UNIVERSITÀ DEGLI STUDI DI ROMA TOR VERGATA
FACOLTÀ DI SCIENZE MM.FF.NN

MASTER DEGREE IN PHYSICS
STRUCTURE OF MATTER

Optimization of γ detection methods for neutron energy analysis on eV neutron spectrometers

---

Candidate:
Dalila ONORATI

Supervisors:
Prof. Roberto Senesi
Prof. Carla Andreani
Dott. Giulia Festa

Academic year 2015-2016

Acknowledgements

Vorrei ringraziare il Prof.Roberto Senesi per avermi dato l'opportunità di svolgere questo lavoro, e per avermi fornito un piano B migliore di ogni altro piano A. Ringrazio anche la Prof. Carla Andreani che rappresenta sempre una guida ed un punto di riferimento. Ad entrambi per avermi permesso di svolgere un'esperienza in un ambiente internazionale come il Rutherford Appleton Laboratory. Ringrazio ovviamente tutti i membri del gruppo di ricerca in particolare la Dott. Giulia Festa.

Ringrazio tutti coloro senza i quali questo percorso non avrebbe avuto lo spesso valore. I miei compagni di studio per avermi spronata, compresa e migliorata. Spingendomi a superare i miei limiti e le mie paure. La mia famiglia, che ha sempre creduto in me e mi ha sostenuta in ogni mia scelta, e sempre lo farà.

Poi ci sei tu, il sapore di ogni cosa che faccio, che mi prendi la mano e mi convinci che insieme siamo tutta la forza che occorre.

Contents

Acknowledgements i

1 Introduction 1

2 Fundamentals of Neutron Physics 3
2.1 Why neutrons? . . . 3
2.2 Neutron Production and Facilities . . . 4
2.2.1 Neutron source . . . 4
2.3 ISIS facility - Rutherford-Appleton Laboratory . . . 6
The Linac . . . 6
2.3.1 The Synchrotron . . . 6
2.3.2 Target Station 1 . . . 7
2.3.3 Target Station 2 . . . 9

3 Neutron interaction with matter: Radiative neutron capture 10
3.1 Radiative neutron capture . . . 11
3.1.1 Nuclear Energy Levels . . . 12
3.2 Radiative-Capture Cross Section . . . 14

4 eV neutron spectrometers at ISIS 17
4.1 Introduction . . . 17
4.2 VESUVIO . . . 17
4.2.1 VESUVIO in the Resonance Detector configuration . . . 20
4.2.2 Foil cycling technique - FCT . . . 22
4.2.3 INES . . . 24
4.3 Calibration of VESUVIO spectrometer . . . 25
4.3.1 L_0 calibration . . . 25
4.3.2 L_1 calibration . . . 26
4.3.3 θ calibration . . . 27
4.3.4 ZrH_2 calibration sample . . . 27

5 Neutron Techniques 29
5.1 Introduction . . . 29
5.2 Prompt Gamma Activation Analysis . . . 29
5.3 Neutron Resonance Capture Analysis . . . 32
5.4 Interaction of Gamma radiation with Matter . . . 33
5.4.1 Photoelectric absorption . . . 34
5.4.2 Compton scattering . . . 34
Pair production . . . 35

6 Characterization of γ-ray background at spallation neutron source beamlines 36
6.1 Introduction . . . 36
6.2 Characterization of the γ background at IMAT beamlines . . . 37
6.3 IMAT data analysis . . . 38
6.3.1 Beam-off and Beam-on background . . . 38
6.3.2 Deactivation of the elements inside IMAT . . . 42

6.4 Background VESUVIO 43
6.5 Result and discussion 43

7 T-PGAA on INES beamline **45**
7.1 Experimental set-up 45
7.1.1 Internal Conversion 49
7.2 Biparametric acquisition 51
7.2.1 ^{10}B peak analysis 54
7.3 Result and Discussion 55
7.4 Experiment ongoing carried out on May 15th - May 20th 2017 61

8 Conclusion and Future perspectives **64**

A Main ROOT algotithm **66**
A.1 Variable definition 66
A.2 Main ROOT algorithm 66
A.3 PGAA and NRCA 68
A.4 Energy vs ToF map 69
A.5 Projection and analysis 71

Chapter 1

Introduction

Neutron scattering techniques are attracting an increasing interest from scientists in various research fields, ranging from physics and chemistry to biology. This mostly relies upon the unique properties of the neutron: being a neutral particle, it interacts weakly with materials and thus it is capable of probing bulky samples. Neutron scattering techniques are able to provide information on structure and dynamics of condensed matter. 'Where atoms are' and 'how atoms move'. The success of these neutron scattering applications is stimulated by the development of higher performance instrumentation. Radiative capture based neutron detectors utilize the emission of prompt gamma ray after neutron absorption in the sample and the detection of those gammas by a photon counter. Several years of extensive development have made eV neutron spectrometers operating in the so-called *Resonance Detector Spectrometer* (RDS) configuration outperform their conventional counterparts. Gamma emission from resonant neutron capture is the mechanism used to select neutron energy, fixing this at the resonance value, and neutron counting, by registering the prompt-γ emission from analyser foil, using the time of flight technique (TOF). VESUVIO indirect-geometry spectrometer, a flagship instrument at ISIS serving a continuous user programme for eV inelastic neutron spectroscopy measurements, is operating in the RDS configuration since 2007 when ^{6}Li-doped neutron detectors at forward scattering angles were replaced by YAP - yttrium aluminium perovskite γ-ray detectors. On VESUVIO, gold foils with a resonance energy of 4.9 eV are used as energy selectors. As a matter of fact, the neutron detection techniques are a key issue to be addressed for the improvement of instrument capabilities. These YAP provide a much superior resolution and general performance, but suffer from a sample-environment dependent γ background. Clearly most of the γ-ray background is removed using the foil cycling technique (FCT). An additional foil, between the sample and detector can be cycled in and out of the flight path of the neutrons, the final signal is obtained by subtracting the signal recorded in the 'foil in' position from the signal recorded in the 'foil out' position. The γ-ray signal from the foil sits on a large background that is one of the limiting factors affecting the data quality and instrument sensitivity on VESUVIO. The background also come if the sample is contaminated with impurities that have resonance peaks in the TOF region of interest.

Briefly the tasks I have carried out in this thesis work are:

1. Calibration of VESUVIO spectrometer and analysis of spurious γ contributions in Deep Inelastic Neutron Scattering (DINS) experiment at eV energies

2. Analysis of the ToF vs Photon energy spectrum of the gold emission in resonance capture conditions

3. Participation and initial data analysis on a DINS experiment with optimised γ thresholds based on the result of ToF - Photon energy spectra analysis made at point 2

As an example of the background subtraction offered by FCT are recorded with a ZrH_2 calibration sample during my first experience on VESUVIO. I took part in the instrument calibration experiment where I could identify that the additional peaks are caused by hafnium contaminations in the ZrH_2 sample. For that reason FCT was introduced. The focus of this work is the analysis of γ spectrum emitted by gold analyser foil used by VESUVIO that are

the heart and the peculiarity of the machine. It will be shown how to achieve an optimized S/B in the RDS configurations, highlighting that possibility to introduced a energy selection windows in the gamma ray cascade spectrum from the resonance analyser is a key parameter for this application. Actually YAP scintillators are set-up to operate with a low level discrimination (LLD) threshold at 600 keV. This optimization has been made to use uranium as an analyzer foil instead of gold. This work reports the data analysis based on measurements made by the group in biparametric configuration, neutron Time of Flight (ToF) versus Photon energy map, acquired with an HPGe detector. A specific task of this thesis was to optimise the implementation, within ROOT environment, of routines used in a previous group work. I will expose the results obtained to understand how these can develop experimental techniques on VESUVIO and if an increase of S/B ratio would allow to improve the quality of the DINS -Deep Inelastic Neutron Scattering - data. Also if this this improvement can be achieved choosing another gamma energy range. I participated in the validation experiment of the hypothesis made in this thesis work. DINS run on a polyethylene reference sample was acquired , by comparing the signal without changing the YAP threshold with that obtained by modifying the threshold. In the final chapter I will show a hint of the results that are still being processed.

Finally I presented the result of this work in a seminar hold on May 17-2017 at the Rutherford Appleton Laboratory during the Molecular Spectroscopy Group Meeting.

Chapter 2

Fundamentals of Neutron Physics

2.1 Why neutrons?

A neutron is an electrically neutral subatomic particle whose physical properties listed in table 1.1. The weak decay of a free neutron is $n \rightarrow p + e + \bar{\nu_e}$ where p is the proton, e the electron and $\bar{\nu_e}$ the anti-neutrino, with a lifetime of about 15 minutes (881.5 ± 1.5) s. Such lifetime is long enough to enable the use of a neutrons beam as a probe for materials investigation.

PHYSICAL QUANTITY	VALUE
Mass	$1.675 \cdot 10^{27}$ kg or 1.0087 u
Charge	0
Spin	1/2
Magnetic Moment	$-1.913\,\mu_n$

TABLE 2.1: Neutron physical quantities ($\mu_n = 5.051 \cdot 10^{27} JT^{-1}$)

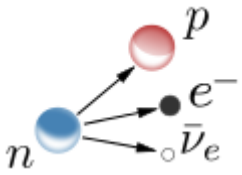

FIGURE 2.1: β decay of a free neutron. An electron and antineutrino are created in this process

Why does one use neutrons for the study of matter and not other particles which would be much easier to handle and much cheaper too ? There are three good reasons.

1. We need a radiation which interacts weakly with matter, so that we are able to treat the scattering in Born-approximation or in other words : we want to see the creation of one excitation and no multiple scattering.

2. The energy E_0, and momentum k of the desired radiation should be of the order of the energies and momenta of the excitations to be studied . In other words : the wavelength λ, should be comparable to the atomic distance, the energy E_0 should be comparable to excitation energies in the system under study.

3. For the study of magnetic properties we need spins. When a neutron is scattered by a nucleus with non-zero spin, the strength of the interaction depends on the relative orientation of neutron and nuclear spins. This makes the neutron a unique probe of nuclear spin correlation and ordering at low temperatures.

All these demands are rather well fulfilled by neutrons. Looking for alternatives there are charged particles like protons or electrons . Because of the strong Coulomb-interaction both cannot penetrate deeply into a target. One only sees surface effects. There are photons : they fulfill request (1) . X-rays have the proper wavelength in the order of 1 Å. They are therefore widely used for structure analysis but they do not see magnetic structures. For inelastic processes, however, their energy of about 10 keV is by far too high to see energy transfers of a few meV. On the other side lasers provide an extremely good energy resolution, but their wavelength allows only tu study excitations at very small K (Brillouin Raman-scattering).

According to their kinetic energies, neutrons can be classified in the following groups. Slow neutrons are produced by collisions in a moderating material containing light atoms like H_2O or D_2O. Depending on the temperature of the moderator, **thermal** and **cold** neutrons are usually distinguished from each other. Their energies are smaller than about 100 meV. Neutrons having energies of about 0.1 eV -1 eV are called **epithermal**. The energies of resonance and intermediate energy neutrons lie in the range of $1eV-1keV$, and $1keV-1MeV$, respectively. **Fast neutron** energies are generally regarded as higher than 1 MeV.

	Energy (meV)	**Temperature (K)**	λ Å
Cold	0.1-10	1-200	30-3
Thermal	10-100	120-1000	3-1
Hot	100-500	1000-6000	1-0.4
Epithermal	>500	>6000	> 0.4

TABLE 2.2: Classification of neutron energy - approximate values of range of energy, corresponding temperature and wavelength.

2.2 Neutron Production and Facilities

From its discovery, in 1932 by Chadwick, neutrons start to be **[1]** applied in many fields thanks to their peculiarities. The growing interest from scientists from all over the world, pushed the scientific community to invest in neutron facilities construction in which neutrons could be produced by different processes and used with different purposes. A PGAA instrument consists of a source of neutrons, a collimating beam tube to shape and direct a beam of neutrons onto a sample, a shutter to turn the beam on and off, a target assembly to position the sample reproducibly in the neutron beam, a gamma-ray detector, a beam stop to absorb the neutrons that are not absorbed by the sample, and shielding to protect the detector and personnel from neutron and gamma radiation. Each of these components will be considered in turn because each of them takes part in the composition of our spectra.

2.2.1 Neutron source

Several kinds of sources of neutrons are available for PGAA, each with a characteristic energy spectrum and generated through different processes:

- Photo-production
- Nuclear Fission in reactor neutron sources
- Spallation in Pulsed Spallation neutron sources

In photo-production, neutrons are produced when the energy of an incident photon is higher than the threshold energy of the (γ, n) reaction. This threshold depends on the atomic number of the target, ranging from 7-8 MeV for high Z materials (W, Pb, Fe) to 16-18 MeV for low Z elements (C,O). The photo-neutron energy spectrum is characterized by an evaporation peak in the low energy range and a relatively weak (10% of the integrated intensity) direct-reaction component in the several-MeV energy range with a resultant mean energy of (700 KeV - 1 MeV). Above the threshold energy, the cross section for production of neutrons grows with the photon energy E_γ, reaches a maximum and then decreases. The shape of this peak is characteristic of the reactions of resonance, and is called *giant dipole resonance*(GDR). The giant resonance is attributed to the acquisition of a moment of induced electric dipole. This dipole is generated by photoabsorption of γ which induces a shift relative of protons and neutrons in the nucleus confined itself. For heavy nuclei resonance giant predominantly it decays with

Element	Z	E_t (MeV)
C	6	18.6
N	7	10.6
O	8	15.6
Fe	26	11.2
Cu	29	10.6
Zn	30	11.1
W	74	7.3
Au	79	8.1
Pb	82	7.4
U	92	6.1

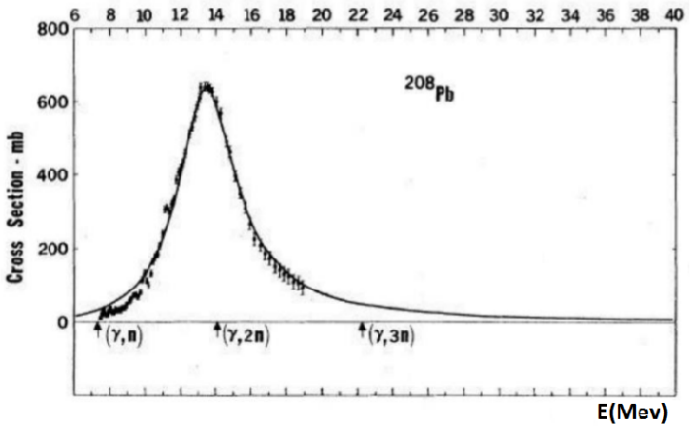

FIGURE 2.2: (a)Threshold energy for some elements
(b) Lead giant resonance

a neutron emission; for higher energies of the incident photons is the reaction can also $(\gamma, 2n)$. The reaction (γ, p) is instead strongly suppressed due to the high value of Colombian barrier, which exceeds the threshold energy of the giant resonance of heavy nuclei.

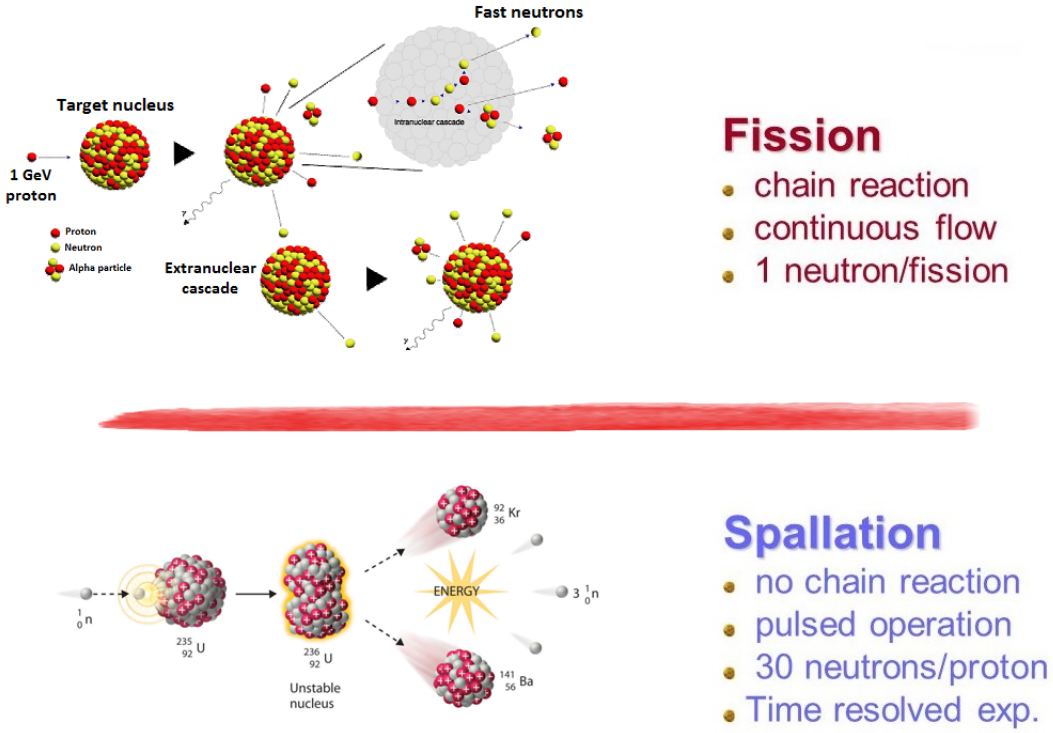

FIGURE 2.3: Fission process of Uranium and Spallation process

In the case of nuclear fission neutrons are produced in the core of reactors employing ^{235}U on the basis of the nuclear fission chain reaction. When a neutron is absorbed by a nucleus of a fissile isotope, e.g.^{235}U, the nucleus is split into two parts by a nuclear reaction, liberating two or three free neutrons. One of these neutrons is required to maintain the chain reaction and, thus, trigger the release of the next generation of neutrons. In a research reactor, as many neutrons as possible should be available for the experiments. Careful design of the reactor core and sophisticated neutron optical devices are needed to maximize the flux of neutrons at the sample positions of the specific experiments. This requires a very high power density in

the reactor core and, therefore, special design features such as a compact core and reflectors to reduce neutron loss from the core. Examples of reactor-based neutron facilities are the NIST reactor in Gaithersburg, MD, and the HFIR reactor in Oak Ridge, TN, in the USA, the research reactor at Chalk River, Canada, the largest research reactor in the world at the Institute Laue-Langevin (ILL) in Grenoble, France, the JRR-3M reactor at the Japan Atomic Energy Agency (JAEA), Tokai, Japan, the FRM-2 reactor in Munich, Germany, and the ANSTO reactor in Lucas Heights, Australia. Reactor safety considerations limit the power and, therefore, the flux possible with research reactors.

For increased neutron flux, accelerator-based spallation neutron sources are the latest neutron sources built in the USA (SNS) and Japan (J-PARC) or planned in Europe (ESS). The Los Alamos Neutron Science Center at Los Alamos National Laboratory, USA, or the **ISIS facility at the Rutherford-Appleton Laboratory** in Didcot, England, are other examples of this type of neutron facility.

All the measurements that are going to be presented in this thesis have been carried out at the ISIS facility which exploits the spallation process for neutron's production.

2.3 ISIS facility - Rutherford-Appleton Laboratory

Proton acceleration at ISIS begins with the ion source, which produces H^- ions. The ion source is fed with hydrogen gas together with hot caesium vapour. A discharge plasma is formed, and positively charged ions from the plasma are attracted towards the cathode surfaces. The deposition of caesium reduces the work function of the cathode, making it a more efficient donor of electrons to the positively charged hydrogen ions, thus enhancing H^- ion production. The H^- ions are extracted from the ion source in 200 μs long pulses to form a beam which is then passed through a 90° magnet to remove any electrons.

The H^- ions acquire an energy of 35 keV across a DC acceleration gap, are focused and monitored in the Low Energy Beam Transport and then passed into the Radio Frequency Quadrupole (RFQ) accelerator. RFQs use intense radio frequency electric fields to focus, bunch and accelerate particles, and are particularly well suited for use with low velocity ions. Inside the RFQ, four specially shaped electrodes produce an alternating gradient quadrupole electric field for focusing and acceleration. Discrete bunches of H^- ions 4.94 ns apart are passed into the linear accelerator (linac).

The Linac

The linac consists of four accelerating tanks in which high intensity radio-frequency (RF) fields accelerate the beam to 70 MeV. Each linac tank has an outer steel wall, which forms a vacuum vessel, and an inner copper liner to make the interior a low loss electromagnetic resonator. RF power at 202.5 MHz is fed to the tank through a coaxial line from a high-power amplifier. The H^- beam enters the tank and travels along the axis where it sees a series of drift tubes. The bunches of ions keep in step with the alternating RF electric field, crossing the gaps between the drift tubes when the field is in the correct direction for acceleration, but being shielded inside the drift tubes when the field is in the wrong direction. The linac provides 200 μs long, 22 mA H^- pulses which are transported to the synchrotron. Final acceleration of the beam occurs in the synchrotron.

2.3.1 The Synchrotron

Ten dipole bending magnets are used to keep the beam travelling around on a circular orbit of radius 26 m, while quadrupole magnets keep the beam tightly focused. On entry the H^- beam is stripped of its electrons by a 0.3 μm thick aluminium oxide stripping foil. The resulting protons are accumulated in the synchrotron over approximately 130 revolutions. The

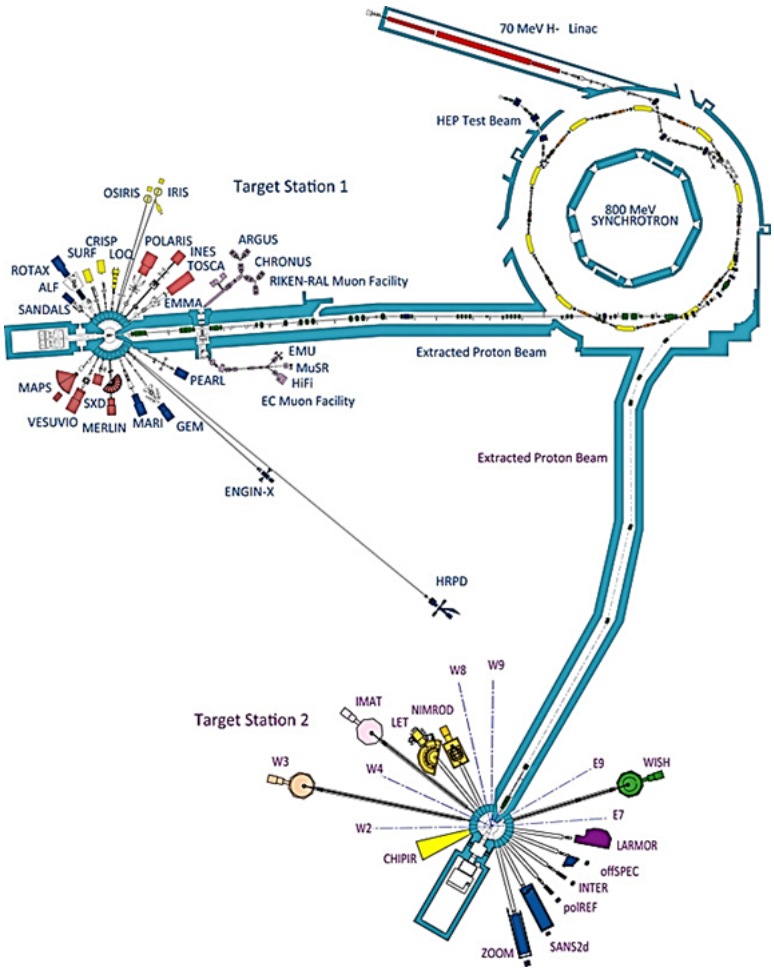

FIGURE 2.4: ISIS is a high power accelerator that fires high energy protons into two targets to release neutrons for experiments. Photo from http://www.isis.stfc.ac.uk.

advantage of this charge exchange injection scheme is that a larger number of protons can be accumulated in the synchrotron than would otherwise be possible.

Once injection is complete the RF system traps the beam into two bunches and accelerates them to 800 MeV. There are six double-gap, ferrite-tuned RF cavities which provide a peak accelerating voltage of 140 kV per beam revolution. The accelerating field and RF frequency are synchronised with the changing magnetic field in the dipoles to maintain a constant proton beam orbit. The beam makes about 10,000 orbits of the synchrotron as it is accelerated, before being kicked in a single revolution into the extracted proton beam line (EPB), delivering $4\mu C$ of protons in two 100 ns long pulses to the neutron and muon targets. The entire acceleration process is repeated 50 times per second, so a mean current of 200 μA is delivered to the targets.

2.3.2 Target Station 1

There are 18 beam channels, 9 on each side of the target, which feed the neutron scattering instruments. Neutrons are produced when the 160 kW proton beam from the accelerator hits a metal target. The target is made from a series of thick tungsten plates, (clad with tantalum to prevent corrosion) housed in a pressure vessel. Water cooling channels remove around 90 kW of heat generated in the target.

Four moderators are used to slow down fast neutrons escaping from the target to the lower speeds required for neutron scattering experiments. Two use water at room temperature, one uses liquid methane at 100 K and the fourth consists of liquid hydrogen at 20 K. The different temperatures result in different energy neutron beams. The moderators are small, about 0.5 l,

and are surrounded by a water-cooled beryllium reflector which scatters neutrons back into the moderators and doubles the useful flux of neutrons.

The only practical way to slow the fast neutrons is by repeated scattering from atoms of a moderating material until the mean energy of the neutrons is comparable to the mean thermal energy of the moderator. The most efficient energy transfer per collision occurs when the scattering atom has a mass equal to that of the neutron: a hydrogen atom. Thermal neutrons are emitted at the moderator surface with an energy spectrum determined by the moderator temperature. The spectra of moderated neutrons which eventually emerge into an experimental hall from a spallation source or a reactor are quite different. In fact the spallation beam has a greater percentage of high-energy neutrons compared to the reactor one. There is another substantial difference: the neutron beam in a reactor is continuous while neutrons from a spallation source arrive in pulses.

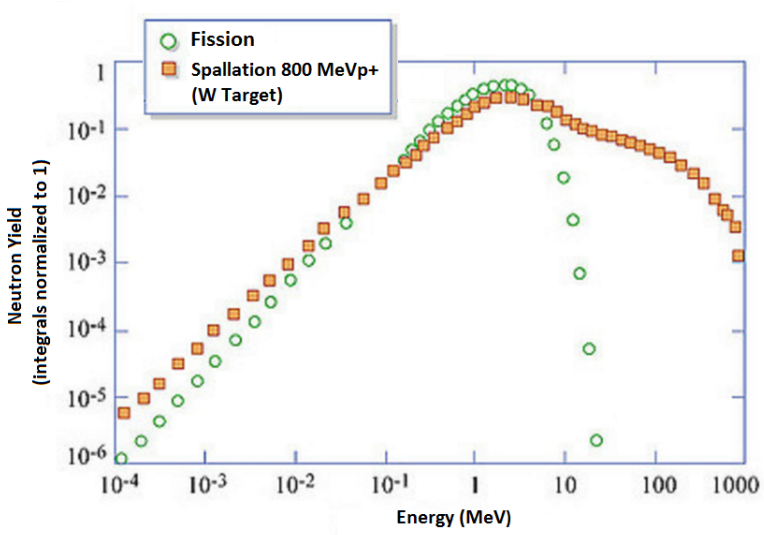

FIGURE 2.5: Neutron yield as function of energy from fission and spallation neutron sources

In the following figure we compare the energy range from fission and spallation neutron production: we can notice that the fission spectrum has a cut off at the energy of the epithermal and fast neutrons ($\approx 20MeV$). In our measurements we take advantage of the dual thermal-epithermal component of the neutron spectrum at ISIS Spallation Neutron Source. Below some technical information about this neutron facility:

NAME	VALUE
ISIS Proton Synchrotron Energy	800 MeV
ISIS Pulsed frequency	50 Hz
ISIS average proton current on the target	175 μA
Neutron yield	30 n/p
ISIS neutron production	$4 \cdot 10^{16}$ n/s

TABLE 2.3: Parametersof ISIS Spallation Neutron Source, Chilton (Oxford), UK.

2.3.3 Target Station 2

The ISIS Second Target Station is a low-power, low-repetition-rate neutron source optimised to maximise the production of long wavelength neutrons. It is required to produce neutrons of two pulse shape varieties.

The first, a wide pulse shape with full width at half-maximum height (FWHM) no bigger than 300 μs and a modest tail, is generated by a coupled moderator; whilst the second is a simple pulse shape de-coupled moderator, with little or no tail, and a width comparable to those of the existing ISIS methane and hydrogen moderators (30–50 μs).

Chapter 3

Neutron interaction with matter: Radiative neutron capture

In this chapter we want to discuss the main properties of neutron-matter interaction in order to deeply understand the implication of the techniques that have been used and explained in this thesis.

Neutrons are neutral particles, therefore they travel in straight lines, deviating from their path only when they actually collide with a nucleus to be scattered into a new direction or absorbed. Neither the electrons surrounding (atomic electron cloud) a nucleus nor the electric field caused by a positively charged nucleus affect a neutron's flight. In short, neutrons collide with nuclei, not with atoms.

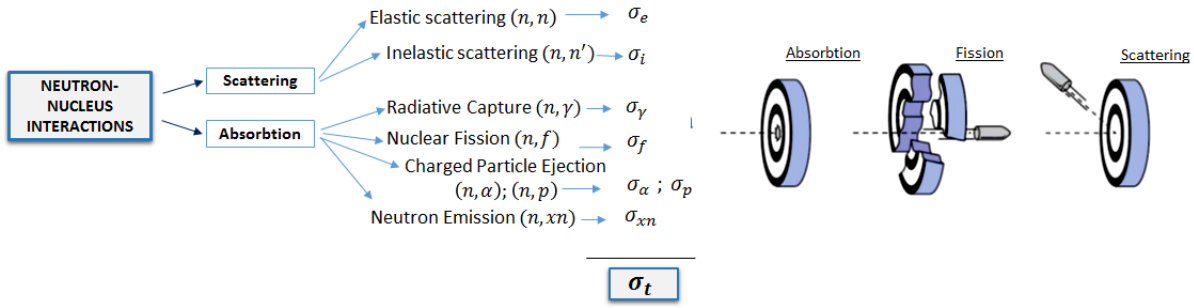

FIGURE 3.1: Schematic resume of interaction between neutron and nucleus

In ease of elastic scattering the incoming neutron interacts with the nucleus. It does not excite the nucleus, but the neutron changes its outgoing direction, and also loses some kinetic energy because of the energy transfer to the recoil of the scattering nucleus. This energy loss is the main mechanism in neutron thermalization. At low energies, when the neutron wavelength is approaching the distance between the atoms, the wave effects become important. In crystalline materials appears the so-called Bragg scattering of neutrons, similar to the X-ray Bragg scattering. It can be used for producing a mono-energetic neutron beam.

The inelastic scattering of neutrons can happen only when the neutron energy is above the energy of the first excited state of the scattering nucleus, i.e. it is a threshold reaction. This type of re action can be used for monitoring fast neutron beams.

Energetic fast neutrons may produce other particle emission in materials. These include $(n, p\gamma), (n, Xn\gamma)$, where X = 1, 2, ... or $(n, a\gamma)$ reactions which are mostly threshold or endothermic reactions. In other words, they can happen only above a given energy, characteristic of the target material. These reactions can also be used to study the energy distribution of the incoming neutron flux, similar to the inelastic neutron scattering reactions.

The absorption reactions the neutron is completely absorbed and compound nucleus is formed. The most important absorption reactions are divided by the exit channel into two following reactions:

- *Radiative Capture.* The reactions result in the loss of a neutron coupled with the production of one or more gamma rays

- *Neutron-induced Fission Reaction.* During the irradiation of fissile nuclides a large number of radioactive fission products are formed with extremely different half-lives, and which emit prompt and delayed gamma radiation

The extent to which neutrons interact with nuclei is described in terms of quantities known as cross-sections. Cross-sections are used to express the probability of particular interaction between an incident neutron and a target nucleus. It must be noted this likelihood do not depend on real target dimensions. In conjunction with the neutron flux, it enables the calculation of the reaction rate.The standard unit for measuring the microscopic cross-section σ is the barn, where 1 barn = $10^{-28}m^2$, which has the dimensions of area (analogy with target size), which is equal to $10^{-28}cm^2$. Total cross-section is defined as the sum of the scattering and absorption cross section :

$$\sigma_t = \sigma_S + \sigma_A = \sigma_e + \sigma_i + \sigma_\gamma + \sigma_\alpha .... \tag{3.1}$$

he microscopic cross sections are tabulated as a function of energy and are compiled in data bases such JANIS (Java-based nuclear information software) provided by NEA-Nuclear Energy Agency.

3.1 Radiative neutron capture

The most important process for this thesis as we will see in next chapters is the radiative capture process, let's analyze it in more detail.

Wherever a nucleus absorbs a neutron, a compound nucleus is formed whose excitation energy equals the binding energy plus the kinetic energy of the neutron. When irradiating with slow neutrons (i.e. when the kinetic energy is in the meV range), the capture state has a well-defined energy value, which practically equals the neutron binding energy. The decay of the compound nucleus takes place typically in $10^{-9} - 10^{-12}s$, the nucleus reaches its ground state by emitting gamma rays in a cascade, according to the reaction:

$$Z^A + n \rightarrow \left(Z^{A+1}\right)^* \rightarrow Z^{A+1} + \gamma + Q \tag{3.2}$$

Since the rest mass of a gamma ray is zero, the Q value is given by

$$Q(n,\gamma) = 931\frac{MeV}{amu}\left[M(Z^A) + m_n - M(Z^{A+1})\right] \tag{3.3}$$

which is seen to be just the energy necessary to separate the neutron from the nuclide Z^{A+1}.

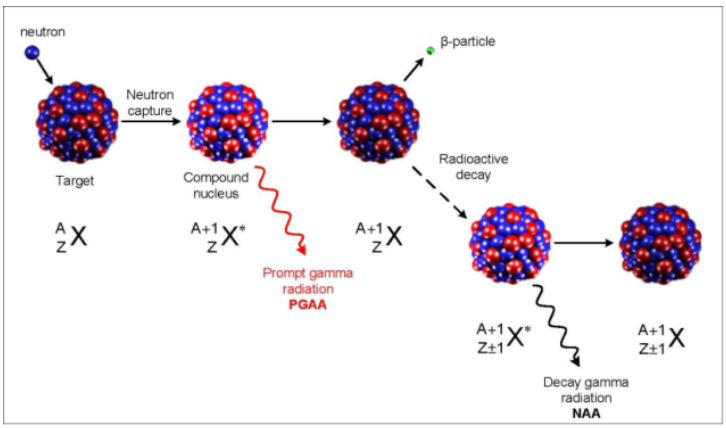

FIGURE 3.2: Schematic representation of Neutron capture with emission of prompt gamma-rays and delayed gamma radiation produced if the formed nuclide is not stable.

Gamma rays are called **prompt**, if their decay times following the capture, are much shorter than the resolving time of the detection system,which typically is in the range of $10ns$ to $10\mu s$. Prompt gamma radiation is characteristic, i.e. the energy values of the gamma rays identify the nuclide, and their intensities are proportional to the number of the atoms. Most nuclides emit several hundreds of different energy prompt gamma rays. Only the lightest ones have simple prompt gamma spectra, since the number of energy levels below the capture state is small. If the ground state of the daughter nucleus is stable, the process ends here. When the ground state reached after the de-excitation is not stable, radioactive decay radiation (typically β-decays and electron capture followed by gamma rays) with a given half-life will also be emitted. The detection of the **delayed gamma** radiation produced in this way is the basis of the *traditional neutron activation analysis* (NAA), but several nuclides can be analyzed in PGAA using their decay radiation too.

3.1.1 Nuclear Energy Levels

The formulation of the general theory describing nuclear interaction depends very strongly on the resonance in the measured cross section. In light nuclei (A < 25) we find resonances in the meV region. In medium weight nuclei $(25 \leq A \leq 70)$ the resonances can be found in the keV region, in heavy nuclei (A > 70) the resonances begin in the eV region. The existence of neutron resonance can be explained by considering the virtual energy levels of the compound nucleus. The energy eigenvalues of a neutron in a potential determined by A other nucleons are the neutron energy levels in the nucleus with A+1 nucleons. The situation is depicted schematically in Fig.**??**, which shows the the neutron energy levels in the nucleus Z^{A+1}.

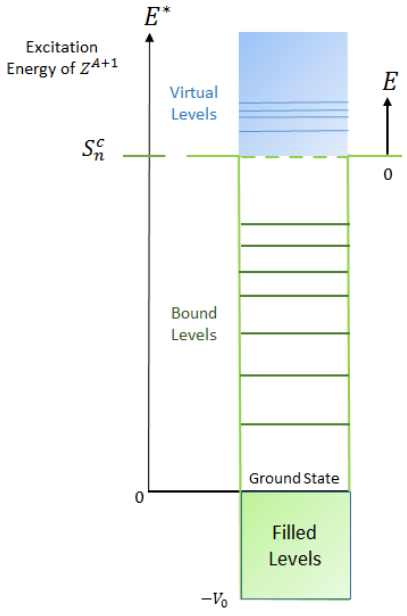

FIGURE 3.3: Highly schematic representation of Neutron energy levels in the nucleus Z^{A+1}, showing the filled, bound and virtual levels and the two energy scales E^* and E.

Two distinct energy scales are employed:

- The excitation energy E^* of the nucleus Z^{A+1} has its origin at the ground state of the compound nucleus
- The neutron's kinetic energy E has its origins at an excitation energy equal to the separation energy S_n^c of a neutron from the compound nucleus

Energy levels below $E^* = S_n^c$ are discrete. Above S_n^c the energy eigenvalues are continuous; however there are some of these energies an which the wave function inside the nucleus

is much larger than at nearby energies. These *virtual levels* are indicated by lines superimposed on the background continuum. The levels that can be excited by a neutron incident on a target nucleus, Z^A, are those who lies above the separation energy S_n^c. A virtual level at excitation energy $E^* = S_n^c + E$ will manifest itself in a resonance at neutron energy E. So we can say that resonances provide us with direct information only about the levels in the compound nucleus that we S_n^c above the separation energy. All the levels of a nucleus, with the possible exception of the ground state,have finite width because they have a finite probability of decay. The ground state has no width if the nucleus Z^{A+1} is stable against radioactive decay; if the nucleus is unstable, the ground state has also a finite width. As we will see better in next chapter for the PGAA, all the excited states, bound and virtual, may decay by γ emission. In addition for virtual states it may be possible to decay by proton or alpha emission or in some few heavy nuclei by fission.

The *decay probability* is the quantity associated with each of the excited states per unit time. They are represented by $\Lambda_\gamma(E^*)$, $\Lambda_\alpha(E^*)$ etc. The reciprocal of the decay probability $\tau_i = 1/\Lambda_i$ is called *mean life* of the state with respect to decay by mode i. Usually each decay probabilities is expressed in energy units, multiplying it by $\hbar$ to get:

$$\Gamma_i = \hbar\Lambda_i = \frac{\hbar}{\tau_i} \tag{3.4}$$

The quantity Λ_i is the *partial width* of the level toward decay by mode i. Let's note the correspondence between this equation written in form $\Gamma_i\tau_i = \hbar$ and Heisenberg uncertainty relationship for energy and time, $\Delta_E\Delta_t \simeq \hbar$. Because the state has a finite lifetime, the uncertainty in its time of decay is not infinite, and, therefore, the uncertainty in its energy must be finite. Since a particular level may be able to decay by several modes, the total decay probability of an energy level is the sum of its partial decay probabilities:

$$\Lambda = \sum_i \Lambda_i \quad or \quad \Gamma = \sum_i \Gamma_i \tag{3.5}$$

For bound states the *total width* Γ is the sum of Γ_γ plus, possibly, Γ_p,Γ_α etc. For virtual levels Γ is the sum $\Gamma_n + \Gamma_\gamma$ plus, possibly, Γ_p,Γ_α etc. The mean life of a level is given by $\hbar/\Gamma$ or, numerically, by

$$\tau(sec) = \frac{6.6 \cdot 10^{-16}}{\Gamma(eV)} \tag{3.6}$$

We can see that a level with a mean life of $10^{-16}s$ will have a width of the order of eV. The width of an energy level is a quantum mechanical concept that follows directly from the uncertainty relationship between energy and time. It is easy to show how the wave function describing a state may be modified to include the probability of decay of that state. Consider a situation in which a large number, N_0, of nuclei are created at time $t = 0$ in identical excited states with excitation energy E^*. At any subsequent time t, the number,$N(t)$, remaining in the excited state will be given by the exponential decay law:

$$N(t) = N_0 e^{-\Lambda t} \tag{3.7}$$

where Λ is the total decay probability per unit time. The quantum mechanical statement of the exponential decay law is

$$|\Psi|^2 = |\Psi_0|^2 e^{-\Lambda t} \tag{3.8}$$

The stationary wave Ψ_0 has the form

$$\Psi_0(\mathbf{r}, t) = \psi_0(\mathbf{r}) e^{-iE^*t/\hbar} \tag{3.9}$$

and,therefore, Ψ has the form

$$\Psi(\mathbf{r},t) = \psi_0(\mathbf{r})e^{-iE^*t/\hbar}e^{-\Lambda t/2} = \psi_0(\mathbf{r})e^{-i(E^*-i\Gamma/2)t/\hbar} \tag{3.10}$$

after the substitute $\Lambda\hbar = \Gamma$.

Thus we can see that the wave function describing a non stationary state is different from that for a stationary state in that energy E^* is replaced by the complex energy $\left[E^* - \left(i\frac{\Gamma}{2}\right)\right]$. The square of the wave function for an unstable state decays exponentially; therefore, as time goes on, it becomes less and less likely that the nucleus described by this decaying wave function will still be in its initial state.

3.2 Radiative-Capture Cross Section

The capture cross section is highly dependent on the neutron energy we can divide it into three characteristic zones.

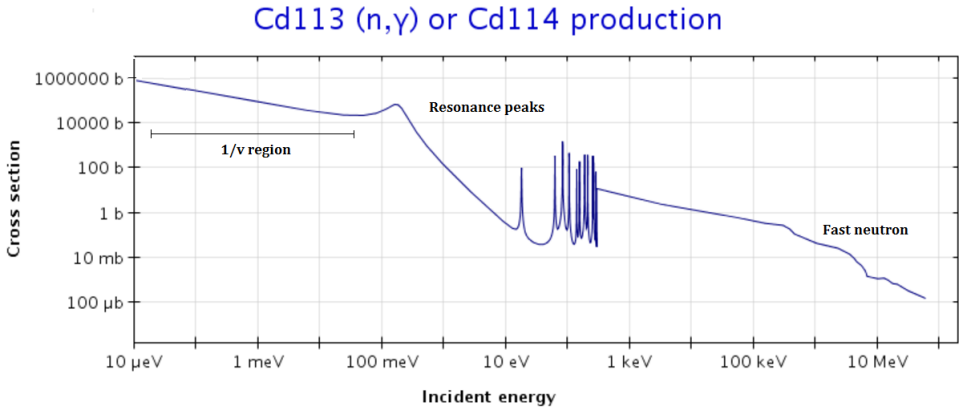

FIGURE 3.4: Capture cross section of ^{113}Cd

- For slow neutrons the most important energy dependence is the so-called **l/v law**, i.e. the cross section is inversely proportional to the velocity of the neutrons. Its validity has been demonstrated down to 10^{-6}eV. It can be seen that in the capture cross-section of ^{113}Cd for example, below 10^{-2}eV the slope of the energy function is $\frac{1}{2}$ in accordance with the $\frac{1}{\sqrt{E}}$ energy dependence. However, there is a strong resonance at 0.18 eV, above which the cross section drops almost six orders of magnitude in a span of 70 eV. (The slope on the high energy side is -3/2. Further resonances appear around 10^2eV. This $1/v$ behavior obtains because the energy levels in the compound nucleus near the neutron separation energy S_n^c are widely separated compared with the widths Γ_γ of the levels. By "widely separated" we mean $D >> \Gamma_\gamma$, but since Γ_γ is only a fraction of an eV, the average separation D need only be a few eV. This law known as "law of neutron absorption" can be explained on the basis of the assumption that only l=0 neutron contribute to the reaction cross section at low energy. Because neutron-nucleus reaction do in fact occur, it is necessary to add quantum-mechanical formalism, in particular the PWA-partial wave analysis. Therefore the $1/v$ behavior of the (n,γ) cross section can be readily derived as a special case of the Breit-Wigner single-level formula

$$\sigma_\gamma(E) = \pi\lambda^2 g(J)\frac{\Gamma_n(E)\Gamma_\gamma}{2\pi(E-E_0)^2 + (\Gamma/2)^2} \tag{3.11}$$

where g(J) is the statistic spin factor which take into account the multiplicity of the final states due to the angular momentum composition of the incident particle and compound

nucleus. E_0 is the energy in which is located the resonance that is greater than E and Γ, E is the kinetic energy of the neutron in laboratory reference system, the denominator is practically constant. Recalling that the neutron width is given by

$$\Gamma_n(E) = \Gamma_n(E_0)\sqrt{E/E_0} \tag{3.12}$$

we reduce the Breit-Wigner expression to

$$\sigma_\gamma(E) = \frac{\pi\hbar^2}{2mE} g(J) \frac{\sqrt{E}}{E} \frac{\Gamma_n(E_0)\Gamma_\gamma}{E_0^2} \tag{3.13}$$

All terms on the right side of this equation are constant except $\sqrt{E}/E$. Thus, in the absence of nearby resonances, the single-level $l = 0$ Breit-Wigner cross section varies as $1/v$.

- After this region, at the energy of epithermal neutrons, we can find **isolated resonances** (whose total width is smaller than the distance, in energy units, from the closest resonance) and the radiative cross section assume the shape of the typical *Breit-Wigner resonance*. This region of isolated resonances begins in the keV region in medium nuclei, in the MeV region in light nuclei and in the eV region for very heavy nonmagnetic nuclei. The (n, γ) cross section for a single isolated resonance is given by the dispersion formula :

$$\sigma_\gamma(E) = \pi\lambda^2 \frac{2J+1}{4\pi(2I+1)} \frac{\Gamma_n(E)\Gamma_\gamma}{(E-E_0)^2 + (\Gamma/2)^2} \tag{3.14}$$

where I is the spin of the target nucleus, J is the spin of the compound nucleus (if I=0 we can have only J=1/2). The radiative-capture width, Γ_γ, is generally of the order of 0,5 to 0,1 eV in the medium-mass nuclei and smaller for heavy nuclei and is somewhat smaller (0.1 to 0.03) in the heavy nuclei. These widths imply, through the uncertainty principle $\Gamma_\gamma\tau_\gamma \simeq \hbar$ mean radiative lifetimes of the order of 10^{-13} to 10^{-15}. The interesting thing is that these lifetimes are orders of magnitude smaller than those from protons or alpha emissions, this is the reason why the radiative capture is the most common reaction induced by slow neutrons.

- Finally at higher energies ($\simeq$ MeV) the resonances start to overlap and it becomes impossible to distinguish them, the result of this behavior is a decrease of $\sigma_\gamma$to very low values at high energies. If it were possible to experimentally resolve the individual resonances, it would make sense to analyze them using individual Breit-Wigner formulas. So the only thing that can be done to analyze this region is to estimate the average cross section over many resonances. Consider first the area under a single resonance given by:

$$\sigma_i = 2\int_{E_0-\Gamma/2}^{E_0+\Gamma/2} \tag{3.15}$$

we shall assume that $\sigma_\gamma(E)$ is given by the Breit-Wigner formula and that λ,$\Gamma_n(E)$, and Γ are approximately constant over the energy range of the resonance. Thus

$$\sigma_i = \frac{\lambda^2}{2} g(J) \frac{\Gamma_n\Gamma_\gamma}{\Gamma} \tag{3.16}$$

Consider now the effective cross section for a neutron beam with an energy spread ΔE. If D is the mean level spacing, the number of levels in this range of energy is $\Delta E/D$ (this is also the number of resonances). The average capture cross-section, $< \sigma_\gamma >$, then is $\Delta E/D$ times the average of the integrated cross section divided by the energy interval ΔE. Thus

$$< \sigma_\gamma >= \frac{\lambda^2}{2} < \frac{g(J)\Gamma_n\Gamma_\gamma}{\Gamma D} > \tag{3.17}$$

A further simplification is possible based on the observation that in most nuclei in the intermediate-energy region $\Gamma_n \gg \Gamma_\gamma$ and $\Gamma \simeq \Gamma_n$, so

$$< \sigma_\gamma >= \frac{\lambda^2}{2} < \frac{g(J)\Gamma_\gamma}{D} > \tag{3.18}$$

The above expression is the final result. Since Γ_γ and g(J) are roughly independent of energy and the level spacing D decreases only slowly with energy over ranges of the order of 1 MeV or less, the main energy variation of $< \sigma_\gamma >$ is in λ^2, which goes as $1/E$.

Chapter 4

eV neutron spectrometers at ISIS

4.1 Introduction

The advent of pulsed neutron sources has made available relatively large fluxes of neutrons in the epithermal energy range between 500 meV to 100 eV. Such energy range is usually not available in reactor-based neutron sources and even in pulsed facilities most of the beamlines are subdued to neutron moderators made to provide a beam of thermal (about 25 meV) neutrons. Only in recent times the possibilities given by epithermal neutrons have generated increased interest in the scientific community, due to the fact that neutrons in the lower part of the epithermal range provide information about atomic and molecular phenomena with characteristic energies of some eV, previously of difficult access through traditional probes. Consequently, new research paths for the investigation of certain aspects concerning condensed matter were opened, as for instance the short time single particle dynamics in quantum and molecular systems and high-energy excitations in materials.

The aim of this thesis is to optimize gamma detection on eV neutron spectrometers in particular on VESUVIO spectrometer. This has been designed and built by British and Italian scientists, for inelastic neutron scattering at high energy and momentum transfers operational at the ISIS pulsed neutron source. The experimental technique employed is known as *Deep Inelastic Neutron Scattering* (DINS) or Neutron Compton Scattering in analogy with Compton scattering of photons from electrons. It is the only experimental technique presently available which directly allows the study of mean kinetic energies, and of the atomic momentum distribution, n(p) in condensed matter. The nuclear resonance absorption foil is a basic element for eV neutron spectroscopy, in that it selects the final energy of the scattered neutrons. For this reason in the previous chapter we reserved particular attention to the radiative neutron capture process and to its cross-section.

4.2 VESUVIO

As we have already said VESUVIO is an **indirect-geometry spectrometer** and as the majority of spectrometers on a pulsed neutron source, is a Time-of-Flight (ToF) spectrometer where the energy selection of scattered neutrons is performed using nuclear resonances in thin Au foils. Direct geometry instruments, where the incident neutron energy is selected by mechanical choppers and/or crystal monochromators, are intrinsically limited, in both energy $(\hbar\omega)$ and wavevector (q) transfer, to the maximum incident neutron energy effectively selected. In both cases this quantity has an upper limit at about 1–2 eV for neutron scattering purposes. Inverse geometry spectrometers can reach unlimited $(\hbar\omega)$ and (q). Indeed the higher the selected final neutron energy the larger the values of energy and wavevector transfers achieved in scattering measurements. The only way to select neutron energies above 1 eV on the latter type of instruments is to use nuclear resonances which one hand allow energy selection up to several tens of eV, on the other pose technological problems related to the neutron counting method(**[9]**). At present, the VESUVIO spectrometer like in Fig.4.1 is equipped with (a) a ^{6}Li

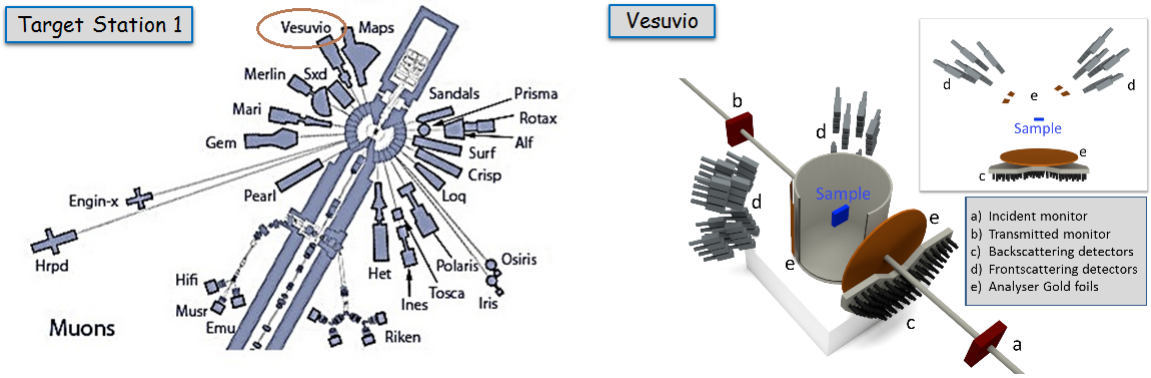

FIGURE 4.1: (a)Position of beamline VESUVIO on TS1 (b) Schematic diagram of the VESUVIO spectrometer

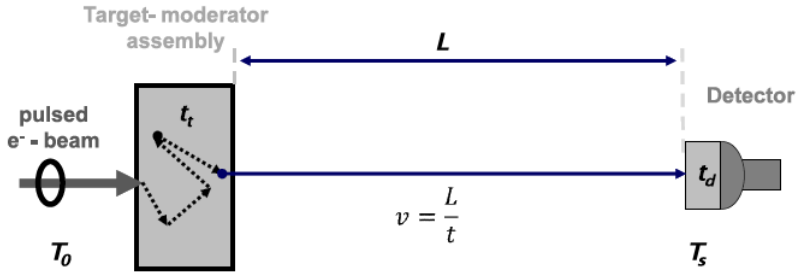

FIGURE 4.2: Schematic representation of the Time of Flight technique in case of a transmission measurement.

doped glass incident beam monitor at 8.57 m from the moderator; (b) a similar monitor for the transmitted beam at 13.45 m from the moderator; (c) a detector bank in backscattering consisting of 132 ^{6}Li doped scintillating-glass detectors of approximate area 20 cm^2 covering the angular region $130° \leq \theta \leq 166°$ at $L_1 \simeq 0.70m$ from the sample position; (d) 64 $\gamma-$sensitive YAP (Yttrium-Aluminum-Perovskite) detectors covering the angular range $37° \leq \theta \leq 67°$ at an average distance $L_1 \simeq 0.50m$ from the sample; (e) moving Au foils used for the Foil Cycling and Double Difference techniques as we will discuss later. The sample area is composed of a tank of 0.4 m in diameter and 0.6 m in height and is generally evacuated down to 10^6mbar. The sample is placed at the centre of the tank at $L_0 = 11.00$m from the moderator.

All measurements are performed using the time-of-flight (ToF) technique that allow to reconstruct the entire kinematics of the process following the relation:

$$ToF = \sqrt{\frac{m_n}{2}}\left(\frac{L_0}{\sqrt{E_0}} + \frac{L_1}{\sqrt{E_1}}\right) = \frac{L_0}{v_0} + \frac{L_1}{v_1} \tag{4.1}$$

with m_n the neutron mass, E_0 and E_1 the initial and final energy of the neutron, respectively. The Time of Flight (ToF) is the time a neutron employs to go from the moderator to the detector. In figure we can see a schematic representation of the ToF pattern in which we can notice that the observed time of flight is the sum of three contributions:

$$ToF = t - t_t - t_d \tag{4.2}$$

where t_t is the difference between the time when neutron leaves the target-moderator assembly and its time of creation; t is the time needed by a neutron to travel the distance L once he left the target-moderator assembly with a velocity v; t_d is the difference between the time of detection and the time in which the neutron enters the detection system.

Experimentally a time of flight is derived from the difference between two well defined

time measurements: the stop signal T_s obtained from the detection system and a start signal T_0 given by the accelerator (for pulsed sources such as ISIS neutron source) or chopper (for continuous sources). An important parameter for ToF detection is the *response function*. It

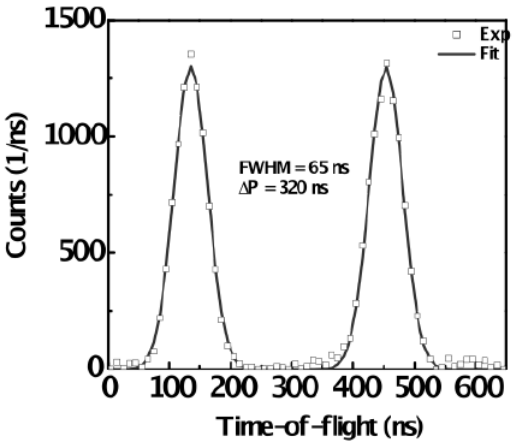

FIGURE 4.3: Contribution of the pulsed proton beam to the response function for TOF measurements at ISIS.

expresses the probability that a neutron with a certain energy E produces a ToF signal, it depends on the distributions of the times and the distance L. We have to pay attention to the contribution due to the difference $(T_s - T_0)$ which is infuenced by the characteristics of the pulsed charged particle beam. At ISIS spallation neutron source this contribution creates a double structure which is given by the sum of two normal distributions separated by 320 ns as we can see in Fig.4.3. The most efficient detectors for TOF measurements are the scintillators due to their high intensities and fast responses.

The count rate at time of flight t in an inverse geometry spectrometer is(**10**):

$$C(t) = 2\left(\frac{2}{m_n}\right)^{1/2} \frac{E_0^{3/2}}{L_0} I(E_0) D(E_1) N \frac{d^2\sigma}{d\Omega dE_1} d\Omega \tag{4.3}$$

where $I(E_0)$ is the intensity of incident neutrons of energy E_0 , $D(E_1)$ is the probability that scattered neutrons of energy E_1 are detected,N is the number of atoms in the beam, $\frac{d^2\sigma}{d\Omega dE_1} d\Omega$ is the average partial differential scattering cross-section of an atom and $d\Omega$ is the solid angle subtended by the detector.

The energy transferred from neutron to sample is:

$$\hbar\omega = E_1 - E_0 \tag{4.4}$$

and the momentum transfer is

$$q = \sqrt{2m}\left(E_0 + E_1 - 2\sqrt{E_0 E_1} cos\theta\right)^{\frac{1}{2}} \tag{4.5}$$

The basic assumption of VESUVIO data analysis is the *Impulse approximation (IA)*. The latter assumes that neutron scattering is incoherent and occurring within time scales much shorter than the typical relaxation times of collective excitations. Under these conditions, the struck particle recoils freely from the collision, with negligible interparticle interactions. The incoherent dynamic structure factor $S(q, \omega)$ is then expressed in terms of the single-particle momentum distribution $n(\vec{p})$ and for a given atom of mass M reduces to a single peak centered at the recoil energy $\hbar\omega_r = \frac{\hbar^2 q^2}{2M}$. The formal statement can be written as:

$$S_{IA}(\mathbf{q},\omega) = \int n(\mathbf{p})\delta\left(\omega - \frac{(\mathbf{p+q})^2}{2M} + \frac{p^2}{2M}\right) d\mathbf{p} \tag{4.6}$$

where $n(\mathbf{p})$ is the atomic momentum distribution for mass M. In this scattering regime the momentum and energy transfer can be considered to be coupled by *y-scaling*; y is the component of atomic momentum p, along the direction of q and M is the mass of the struck atom.

$$y = \mathbf{p}\cdot\hat{q} = \frac{M}{\hbar q}\left(\hbar\omega - \frac{\hbar^2 q^2}{2M}\right) \tag{4.7}$$

where $\hat{q}$ is the unit vector along $\mathbf{q}$.

It is immediately apparent that the IA and the y-scaling centring the contribution from each atomic species at $y = 0$, dependent on the recoil energy for a given mass M.

$$J_M(y,\hat{q}) = \int n(\mathbf{p})\delta(y - \mathbf{p}\cdot\hat{q})d\vec{p} \tag{4.8}$$

$J(y)$ is the so called *neutron Compton profile*, defined as the probability of an atom to have a component of momentum between y and dy. It follows from Eq.4.6 and 4.7 that:

$$S_{IA}(\mathbf{q},\omega) = \frac{M}{\hbar q}J(y) \tag{4.9}$$

A DINS measurement on VESUVIO (for a given detector geometry) thus consists of a set of peaks in ToF, centred at values relating to each atomic species' recoil energy, itself dependent on the atomic mass. In practise a majority of experiments on VESUVIO are on isotropic samples, whereby the $\hat{q}$ dependence of J(y) is lost. The most common model for J(y) is a Gaussian form in y, exact for an isotropic, harmonic potential. In this case the atomic kinetic energy $< E_k >$ relates to the standard deviation of the Gaussian, σ, through

$$J(y) = \frac{1}{\sqrt{2\pi\sigma^2}}e^{-\frac{y^2}{2\sigma^2}} \tag{4.10}$$

$$< E_K >= \frac{3\hbar\sigma^2}{2M} \tag{4.11}$$

This simple expression represents the elegance of DINS. For a given system, each mass is expressed as an individual peak in ToF, the widths of which (in actuality the standard deviation of Gaussian peak in the y-space for each mass) are a direct measurement of their mean kinetic energy and thus confining potential.

4.2.1 VESUVIO in the Resonance Detector configuration

The VESUVIO ^{6}Li-doped neutron detectors at forward scattering angles were replaced in February 2008 by yttrium aluminium perovskite (YAP)-doped γ -ray detectors(**[10]**). Although these do not detect neutrons directly, they are made to function both as neutron detectors and energy selectors by placing a gold foil on the YAP detector surface. YAP is a fast, mechanically and chemically resistant scintillator material, with mechanical properties enabling precise machining to many different shapes. The inorganic scintillator is nonhygroscopic, glasslike, with a high density $(5.55g/cm^3)$ but a low effective atomic number (Z=36). Main characteristics of this scintillation material are a good light yield ($\approx$ 18000 photons/MeV) and a short decay time (τ=27 ns) at a wavelength of maximum emission of 350 nm. The material is relatively stable over a wide temperature range. Its chemical composition is such that no neutron resonances are present in the energy range of interest (1–200 eV).

In the RD technique the detection of scattered neutrons via a photon detector consists of two separate processes:

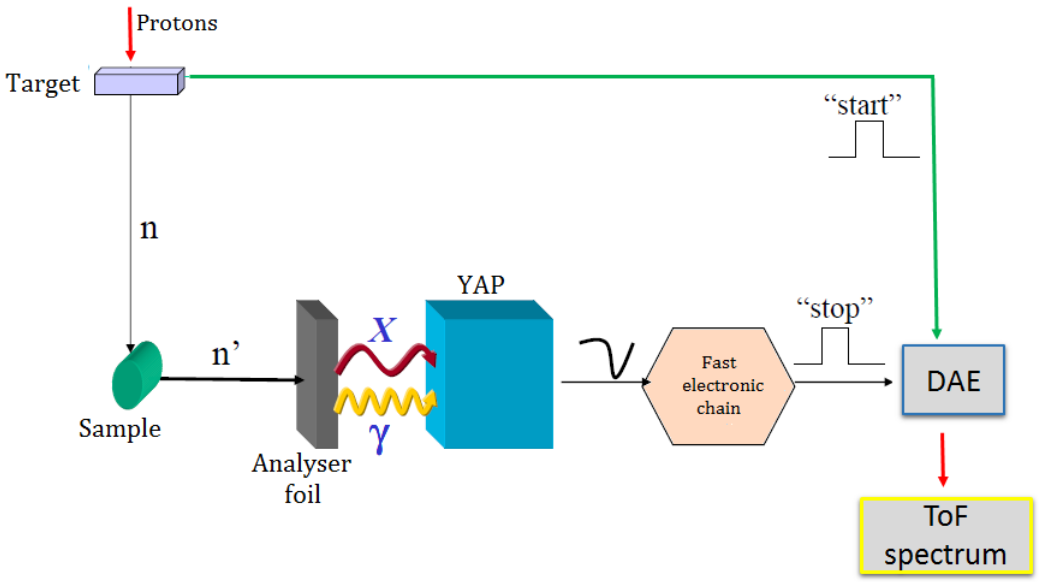

FIGURE 4.4: Chain of Resonance Detector techniques

- resonant neutron capture in the analyzer foil
- detection of the prompt radiative capture γ rays (as well as X-rays) which are emitted following resonant neutron absorption

The intensity of the resonance cross section defines, for a given thickness of the analyzer foil, the neutron absorption efficiency while the resonance width contributes to the overall spectrometer energy resolution (**[5]**). Thus important requirements for the choice of the best analyzer foil are well separated and intense resonance cross sections (σ_R defined as the cross section at the peak) with intrinsic narrow widths [Γ_R, expressed as full width at half maximum (FWHM)].

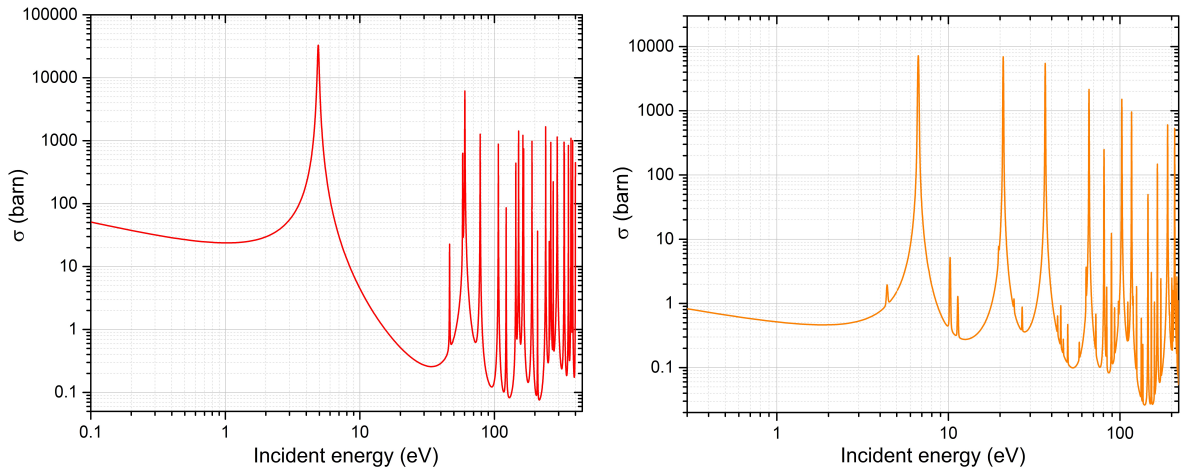

FIGURE 4.5: (a)^{197}Au cross section (b) ^{238}U cross section

VESUVIO spectrometer employs routinely ^{197}Au as analyser foils but previously were used ^{238}U foils. In the case of ^{238}U several high-intensity resonances are available in the energy range 1–200 eV most of which have small values of Γ_R varying within the energy interval 25–50 meV. In the same energy range, on the contrary, ^{197}Au has only two intense and broad resonances (Γ_R >135 meV).

In the case of the ^{238}U analyser foil, the neutron absorption efficiency varies from 10% for the less intense resonance $(E_n = 80.73eV)$, to nearly 100% for the most intense resonance

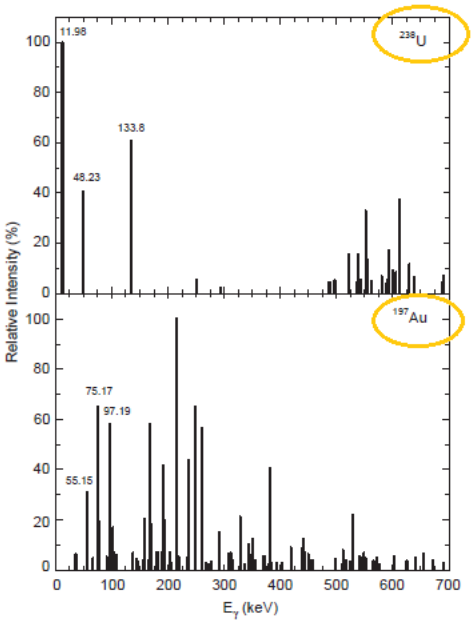

	E_R (eV)	σ_R $(barn)$	Γ_R (meV)	t_{res} (μs)
^{238}U	6.67	23564	24.9	309.5
	20.87	37966	33.7	175.0
	36.68	42228	57.3	132.0
	66.02	20134	48.1	98.37
	80.73	2297	26.9	88.95
	102.5	18989	94.4	78.94
	116.9	11845	47.8	73.92
	189.7	12228	197	58.03
	208.5	8633	72.8	55.22
^{197}Au	4.90	36592	139	360.9
	60.3	10185	176	102.9

FIGURE 4.6: (a)Relative intensities of the radiative capture $\gamma-$rays following thermal neutron capture on ^{238}U (top) and ^{197}Au (bottom). Only the gamma lines with intensity above 2% in the shown energy region are plotted(b)Main parameters of Gold and Uranium resonances.

$(E_n = 36.68eV)$. The ^{197}Au foil provides good neutron absorption efficiency, namely about 91% and 37% for the 4.906 and 60,3 eV resonances, respectively. The predicted γ-ray emission spectra following thermal neutron absorption in the ^{238}U and ^{197}Au isotopes, in the energy region below 700 keV; are shown in Fig.4.6. One can note that the most intense γ line for ^{238}U occurs at a value of $E\gamma$ of about 12 keV and that the whole set of low energy γ lines, i.e. 12, 48 and 134 keV; represent about 50% of the overall γ emission in the energy range of interest. In the case of ^{197}Au several intense lines are present in the region 50–300 keV and the strongest line is centred at 215 keV. Overall this isotope shows a γ emission spectrum distributed over a broader energy range compared to ^{238}U.

4.2.2 Foil cycling technique - FCT

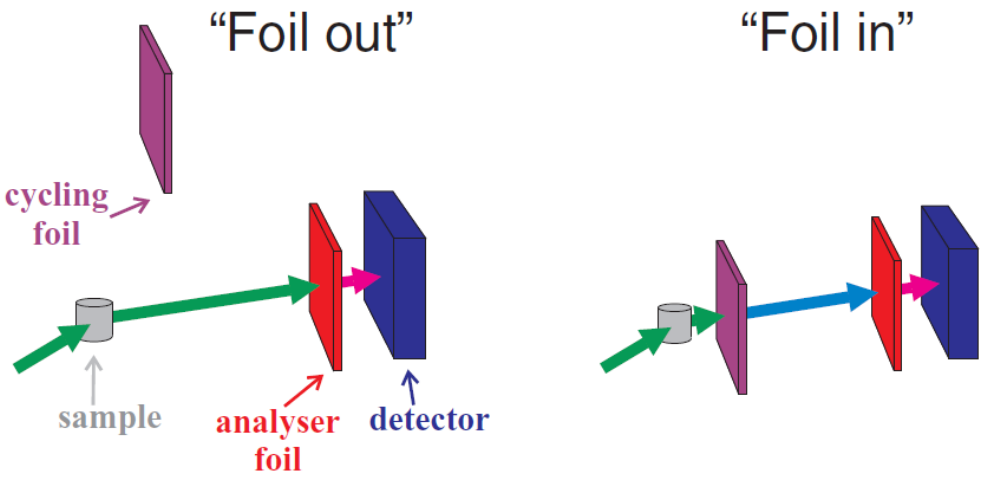

FIGURE 4.7: Schematic representation of the setup used in the foil cycling technique. **[11]**

The ToF spectra recorded by the detectors represent the scattering signal. There are a limitations in the RD approach like: a poor signal-to-background ratio of the measurements and the requirement for heavy shielding around the resonance detectors in order to reduce the γ and neutron background contamination. For these reasons the RD concept was replaced with *Resonance-Filter techniques* used for both forward and backforward detectors .

It envisages the use of two foils of the same material: the first foil (analyzer) is placed in front of the photon detector and behaves as a standard energy analyzer for the RD configuration , while the second foil (cycling foil) is placed between the sample and the analyzer at a given distance from the latter. In the scattering experiment the cycling foil alternates in and out of the scattered neutron beam, leaving the analyzer in front of the photon detector. Subtracting the spectrum acquired with the cycling foil in the foil-in position from the spectrum acquired in the foil-out position produces the final data. The improvement of the resolution function is due to the narrowing of the FWHM of the transfer function using this technique. The FCT may be called a 'redundant resolution' technique, one resolving method (the RD) piled upon another (the FD).

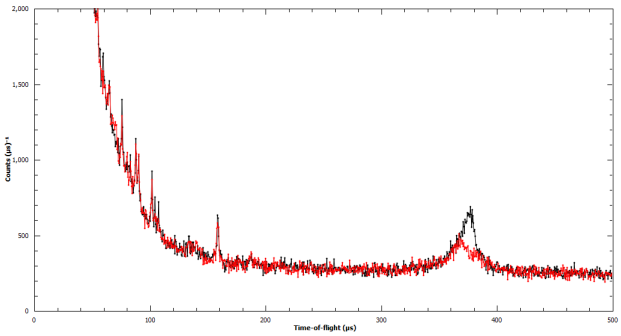

FIGURE 4.8: Data taken from a Pb sample by a single YAP detector at an angle of 52° using Au analyzer foil. The 'foil out' data are in black and the 'foil in' data are in red.

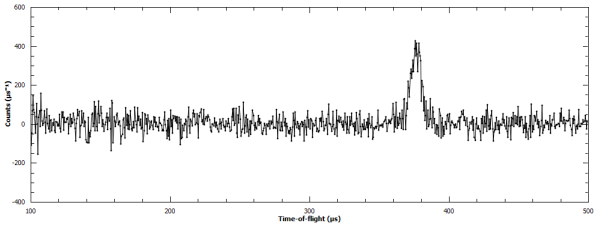

FIGURE 4.9: The black line shown the difference 'foil out-oil in', thus obtained using FCT .The effectiveness of the background subtraction achieved with the FCT in the whole time of flight region can be appreciated.

The cycling foil acts as a filter and removes neutrons from the scattered beam having energies in the range of $\pm\Delta E_r$ near the resonance energy E_r. When the cycling foil is between the sample and the analyzer, the photon detector registers the γ's produced by neutrons that pass the filter and are absorbed by the analyzer. Photons produced by the cycling foil are much less effectively detected due to the smaller solid angle subtended by the detector. The contribution of γ's produced by the cycling foil is further reduced by the subtraction procedure, as the number of γ's from the cycling foil registered by the detector can be made comparable for the foil-in and foil-out positions.

In backscattering this is done by taking measurements with different gold foil thicknesses, the energy resolution of VESUVIO is improved. This *Double Difference* (DD) foil cycling technique achieves a finer experimental resolution than the SDT one, by removing the Lorentzian wings coming from the resonance foils.

It should be noted that running VESUVIO in foil-out mode, i.e. without analyser foils present, allows for the instrument to be utilised as a diffractometer. Foil-cycling the 132

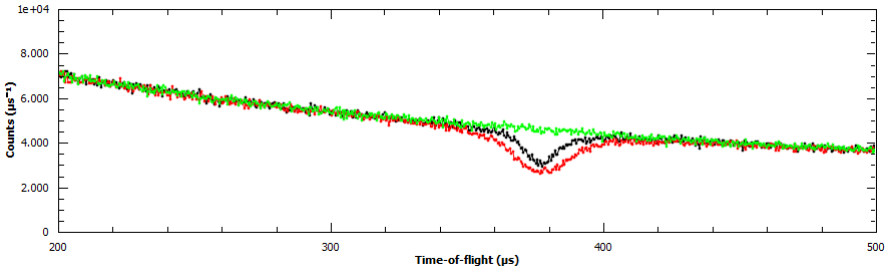

FIGURE 4.10: Illustration of the filter difference method with ^{6}Li-doped neutron detector. Data taken from a Pb sample by a single detector in backscatter. The green line shown 'foil out' data, red line shown 'foil thick' data and black line 'foil thin' data. Each foils configuration is irradiated with $15\mu A/h$

^{6}Li-doped scintillator detectors in backscattering geometry on VESUVIO thus allows for simultaneous diffraction measurements in the thermal neutron region during a standard DINS measurement.

4.2.3 INES

The Italian Neutron Experimental Station INES, located in Target Station 1 at ISIS Spallation Neutron Source, UK, is a neutron powder diffractometer which exploits the neutron beam transmitted by the spectrometer TOSCA. INES has been built with the aim to focus its use in archaeometric measurements, in fact, it is equipped with a large tank in which large sample volume can be accomodated. INES diffractometer is characterized by a primary flight path of $L_1 = 22.804m$ and a sample detector distance of $L_2 = 1.0m$. The neutrons are produced in a white beam, with frequency of 50Hz. The INES beam line is placed on a decoupled-Gd poisoned water moderator at T = 295K that provides a neutron spectrum peaked at E≈30meV and a $E^{-\alpha}$ $(typically 0.9 < \alpha < 1)$ tail in the epithermal-fast neutron region. The time interval allowing for a good quality measurement depends on the nature, thickness and shape of the samples.

The main applications are:

- Crystal and magnetic structure analysis from powder diffraction data
- Non-destructive phase analysis of archaeological objects
- Texture analysis

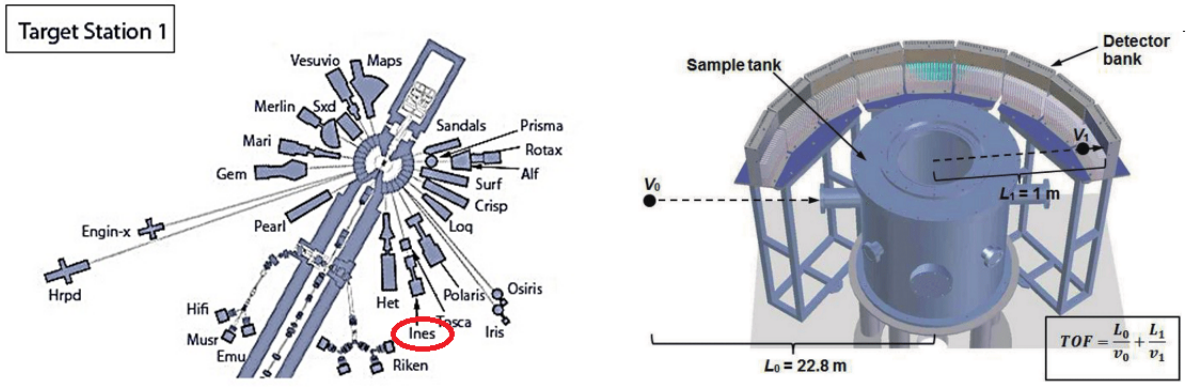

FIGURE 4.11: (a)Position of beamline VESUVIO on TS1 (b) Schematics of INES instrument diffraction configuration and neutron Time of Flight (ToF)

4.3 Calibration of VESUVIO spectrometer

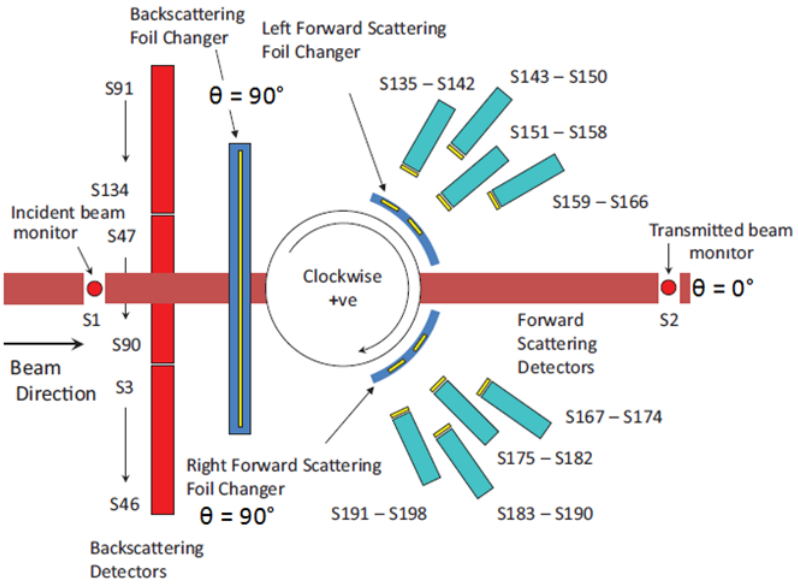

As we said the accurate knowledge of all the relevant numerical parameters as L_0, L_1, E_0, E_1 and θ is necessary for analysis of neutron data at energy transfers in the eV region. The way in which these parameters are determined is the calibration procedure.

During my thesis period I was able to participate in the calibration experiment of VESUVIO with particular attention to gamma-sensitive forward detectors (YAP). For data analysis was used software MANTID. Below are briefly described the methods used.

4.3.1 L_0 calibration

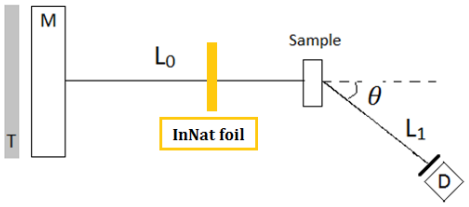

FIGURE 4.12: Representation of the set-up of measurement

L_0 calibration is performed using a Indium sample with a known cross section (n, γ). Indium has a series of sharp neutron resonance absorption peaks and when a neutron is absorbed by one of these resonance, γ-rays are emitted and these are registered by the YAP detectors at forward scattering. L_1 path is covered by photons so $\frac{L_1}{v_1}$ is negligible . Hence the position in time of flight of the gamma ray peaks is determined by

$$TOF = \frac{L_0}{v_0} + t_0 \tag{4.12}$$

independent of detector angle. Once the energy peaks are measured then they are used to calculate the neutron initial velocity ($E_0 = \frac{1}{2}mv_0^2$). By plotting times of flight peaks against $1/v_0$, the initial neutron flight path can be derived from the gradient and t_0 correction from the y-intercept.

$t_{peak} \pm \Delta t_{peak}$ (μs)	$E_r \pm \Delta E_r$ (eV)
405,80 ± 0,02	3,85 ± 0,08
367,70 ± 0.02	4,70 ± 0,07
264,30 ± 0.02	9,07 ± 0,08
229,00 ± 0.02	12,04 ± 0,14
207,45 ± 0.02	14,60 ± 0,07
171,66 ± 0.02	21,55 ± 0,08
166,70 ± 0.02	22,73 ± 0,08
159,80 ± 0.02	24,99 ± 0,09

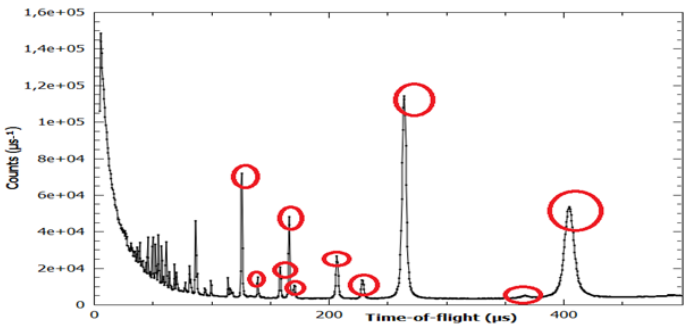

FIGURE 4.13: (a)Parameter defining Indium absorption peak used in the calibration. Energy resonance are provided by JANIS. t_peak is the fitted position in ToF averaged over 64 YAP detector.

4.3.2 L_1 calibration

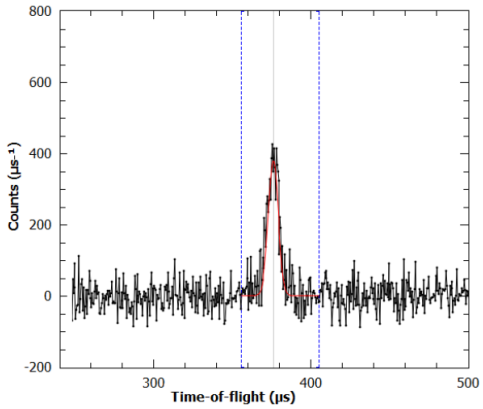

FIGURE 4.14: Pb Compton peak for detector 151

L_1 calibration is performed using a Pb sample (2mm thick and 100cm^2 in area), using the *quasi-elastic approximation*. Imposing $v_1 \sim v_0$, L_1 can be written as:

$$L_1 = -L_0 + v_1(t_{peak} - t_0); \qquad v_1 = 3,06 \cdot 10^{-2} \frac{m}{\mu s} \tag{4.13}$$

where t_{peak} is the value of Pb Compton peak in ToF spectra acquired using the FCT.

Each detector is calibrated independently using this procedure, the derived errors show that the flight paths can be calibrated to an accuracy of a few millimetres. The same procedure can be use for the backscattering detectors. The final flight path from sample to detector can also be determined from the lead calibration using an Uranium foil, in this way we do not need elastic approximation.

Each Compton peak is centred at ToF position corresponding to:

$$\frac{v_1}{v_0} = R(\theta) = \frac{cos\theta + \sqrt{\left(\frac{M}{m}\right)^2 - sin^2\theta}}{\frac{M}{m} + 1} \tag{4.14}$$

this ratio is constant for each detector. In this way we have established a linear equation:

$$t = t_0 + \left(L_0 + \frac{L_1}{R(\theta)}\right)\frac{1}{v_0} \tag{4.15}$$

Graphing the points t vs $1/v_0$ corresponding to each of the ^{238}U resonances, from the angular coefficient m, L_1 can be obtained, in fact $(m - L_0)R(\theta) = L_1$. In this way, with the same procedure we can calibrate L_1 and t_0 simultaneously for each detector. By using lead with respect to uranium, a round down is made.

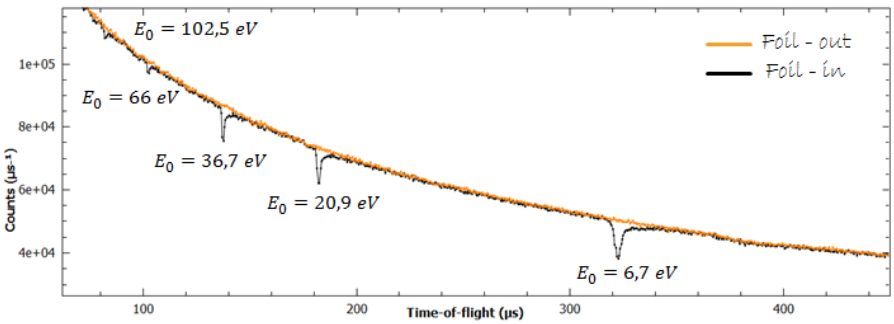

FIGURE 4.15: Resonance holes in the ToF spectrum produced in a single detector with a U foil. The holes in the spectrum provide the neutron flight position with $v_0 = v_{res}$

4.3.3 θ calibration

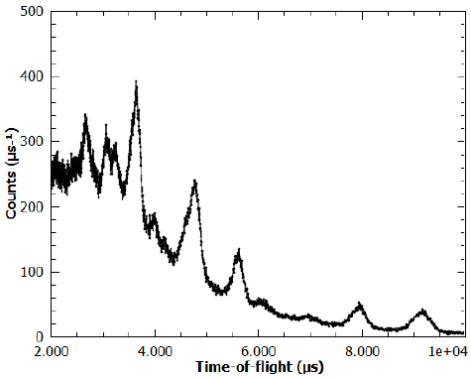

FIGURE 4.16: Diffraction spectra from Pb sample.

θ position calibration of each detector is done using the Bragg peaks of the same Pb sample, in typical TOF range of thermal neutrons $(3000\mu s - 10000\mu s)$. Braggs peaks will be present in a detector spectra at given angle θ, when Bragg's law is satisfied. Thus

$$2dsin\left(\frac{\theta}{2}\right) = n\lambda \tag{4.16}$$

Braggs scattering is elastic, which means $v_0 = v_1 = v$. Using this equations a relation between the measured ToF at which Bragg peaks occour from a Pb calibration sample, with known d-spacing occur, the scattering angle can be obtained (with (n = 1))

$$sin\left(\frac{\theta}{2}\right) = \frac{h(t - t_0)}{2m(L_0 + L_1)d} \tag{4.17}$$

4.3.4 ZrH_2 calibration sample

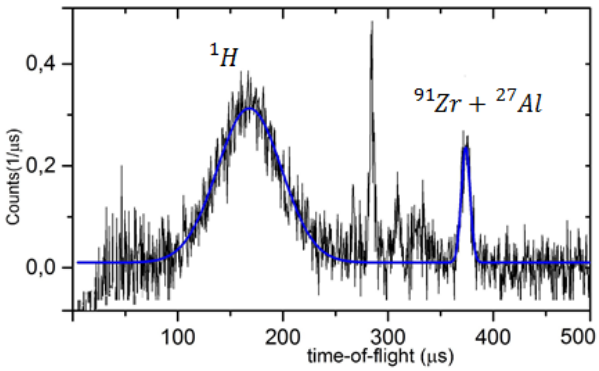

FIGURE 4.17: Experimental ToF spectrum from a ZrH_2 sample. The continuous line is a multipeak fit, Zirconium and Aluminum peaks are overlapping.

During the calibration we used a ZrH_2 reference sample for the identification of mass composition. This sample of thickness of $1mm$ is enclosed in an Aluminium sample container. What we see is the presence of peaks due to impurities present in the sample. They are not recoil peaks but gamma-prompt following the radiative capture process, in fact by changing the detector their position in TOF is not altered, as for the photons ratio L_1/v_1 is negligible. From the position in time of flight of these peaks can be traced back to the energy of the resonance and thus to the responsible element, that is Hafnium , present in zirconium minerals.

The presence of these peaks reveals how my measure is sensitive to gamma-rays, and then to the background, using scintillators detectors. If I could detector neutrons only, I could see

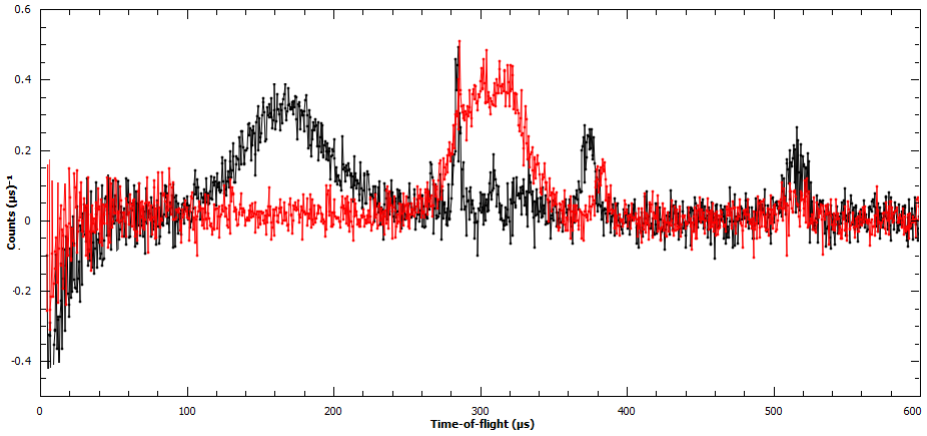

FIGURE 4.18: ToF spectrum from ZrH_2 sample acquired with detector 135 (black line) and detector 160 (red line). The gamma peak remains fixed at 285 μs

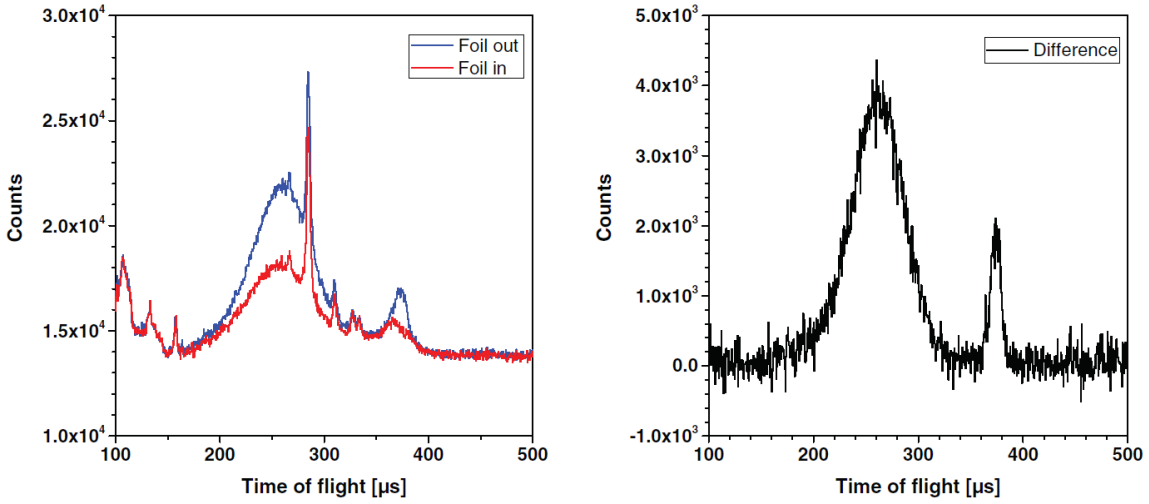

FIGURE 4.19: DINS signals from a ZrH_2 sample with an Au analyser for the 'foil out' and 'foil in' situations are shown on the left. The plot on the right shows the difference signal ('foil out'–'foil in'), illustrating the effective background subtraction obtained with FCT. **[2]**

the sample signal. How can we improve what YAP measures ? This is a first experimental evidence that serves as an inspiration for the purpose of this thesis.

Chapter 5

Neutron Techniques

5.1 Introduction

5.2 Prompt Gamma Activation Analysis

Prompt Gamma Activation Analysis is a neutron technique which consists in the identification of radionuclides present in the chosen sample or in the neutron source environments.The PGAA is a non invasive and non destructive neutron technique based on radiative capture (n, γ) that we have already mentioned previously. Important feature of the method comes from fact that the excitation and the detection take place at the same time, all elements can be analyzed at the same time, and thus a panorama analysis can be performed instantaneously without any prior information on the sample.

PGAA is non-destructive , the irradiation does not change the elemental composition of the sample. The converted nuclei are mostly stable isotopes of the same element, usually, the only problem requiring attention arises when radioactive isotopes are formed. As was mentioned before, every chemical element except ^{4}He can be analyzed using PGAA. However the neutron capture cross sections vary by eight orders of magnitude (from O: 0.00019 barn to Gd: 48800 barn). This fact can be regarded as a disadvantage, because the elements cannot be determined with similar sensitivities.

The energy excitation is the sum of the binding energy and the kinetic energy of the neutron absorbed. The decay time is $\approx 10^{-9} - 10^{-12} s$. We report the schematic representation of the neutron capture which origins the prompt gamma emission:

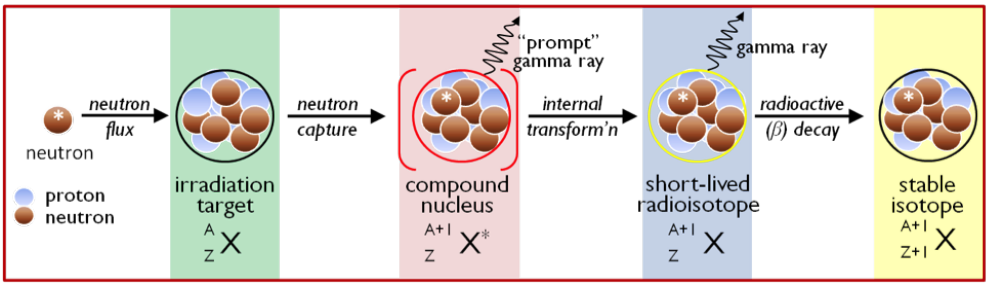

FIGURE 5.1: Schematic representation of neutron capture with emission of gamma-rays

The nuclear energy level structure of the emitter nuclide is the base for the complexity of the prompt gamma spectra. In particular, the number of levels between the capture state and the ground state determine the number and the shape of the PGAA spectra. For the light elements like Li^7, H, we will have only one or few levels below the capture state, in this way, we will have only one or few intense lines in the spectrum corresponding principally to the direct transition and few other levels interactions. As far as the element become heavier, we will have a more complex spectrum. This depend on the number of levels which are involved during the compound nucleus decay. We can distinguish two types of spectrum depending on the atomic number of the element analyzed:

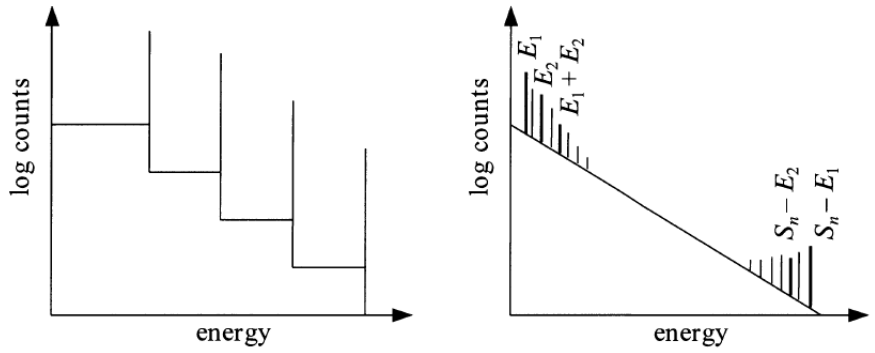

FIGURE 5.2: Typical shapes of prompt gamma spectra for the lightest (type 1) and the heaviest nuclides (type 2).

The spectrum on the left side of the picture is a typical schematic representation of what is called Type1 spectrum for PGAA. It is the spectrum of a light element which is characterized by a low number of very intense peaks spread uniformly in the entire energy range. The intensities of these few peaks are very high because of the high probability they have to be emitted. The spectrum on the right side of the picture has the typical shape of an heavy element prompt gamma spectrum. We can notice that we have only a certain number of peaks situated generally in the first and in the last part of our energy plot. Among those in the low energy range we have secondary crossover gammas $(E_1 + E_2)$ which can be not very well resolved. In the high energy range we can distinguish an ensemble of well resolved peaks among which we have cascade pairs $(S_n - E_1)$. The center zone of our spectrum for heavy elements is usually in lack of peaks. This happens because of the large peak overlap that creates a smooth continuum which increase with the decreasing of the energy. Typically if we could see what happen in this region at a nuclear level, we could have that the disexcitation of a nucleus passes through a lot of branched levels, this causes the creation of tenth of peaks having almost the same energy which overlap and are finally lost in a continuum. Two examples of real spectra for both type 1 (^{5}B) and type 2 (^{7}9Au) categories are reported below.

Semiconductor Detectors

To collect this kind of spectra we used: Semiconductor detectors are used. Semiconductor detectors are based on crystalline semiconductor materials, most notably silicon and germanium. These detectors are also referred to as solid-state detectors they have been developed in the late 1950's. These devices provided the first high resolution detectors for energy measurement and were adopted in nuclear physics research for charged particle detection and gamma spectroscopy. The basic operating principle of semiconductor detectors involve a medium made by solid semiconductor material. The passage of ionizing radiation creates electron-hole pairs which are collected by an electric field. The advantage of the semiconductor is that the average energy required to create an electron hole pair is known, and is independent of the energy of the incident radiation, measuring the number of electron-hole pairs allows the intensity of the incident radiation to be determined. They are compact in size and can have very fast response times. Being crystalline materials, they also have a greater sensitivity to radiation damage which limits their long term use.

In the category of semiconductor detectors the High Purity Germanium Detector is the most used for prompt gamma-ray detection. The Ge crystals of these detectors are produced in different dimensions and shapes, the smaller one are most efficient for γ-rays at low energies and the bigger one are more performant for high energy detection. These detectors have a characteristic high energy resolution due to the low energy requested for Ge (3 eV) to create an electron-hole pair. The acquisition chain of the HpGe is made by the following component:

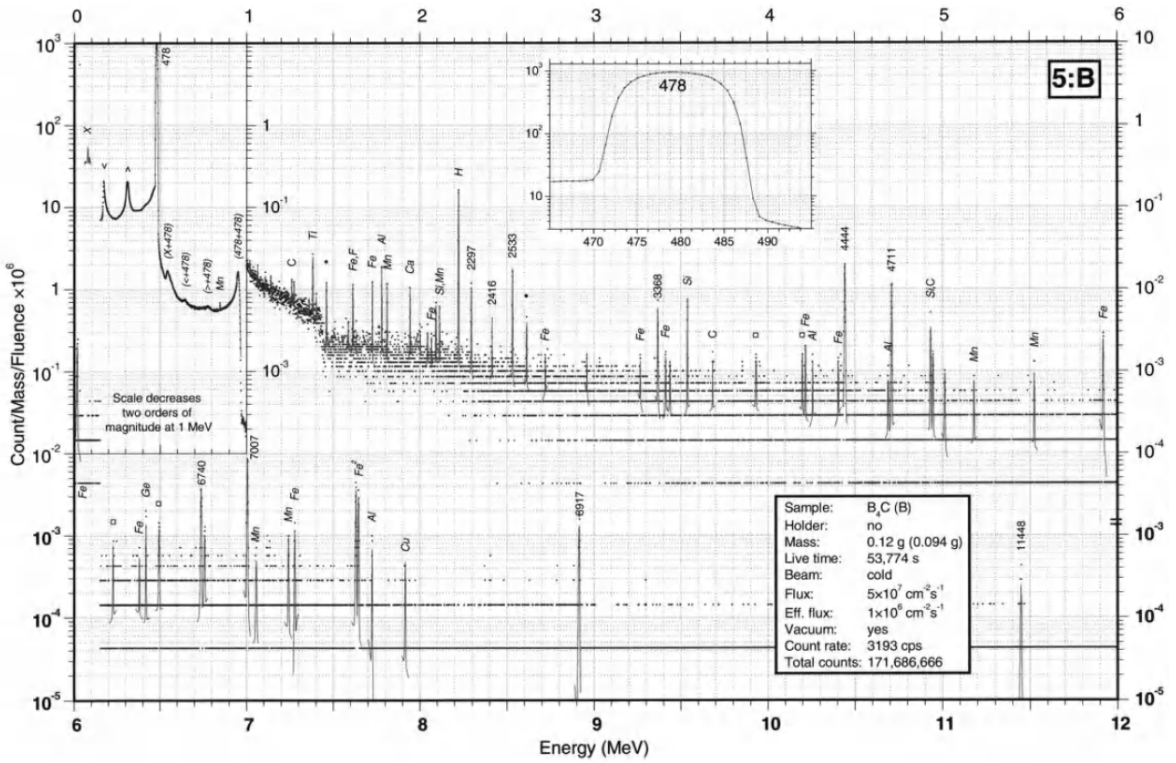

FIGURE 5.3: PGAA spectrum from a light element: ^{5}B

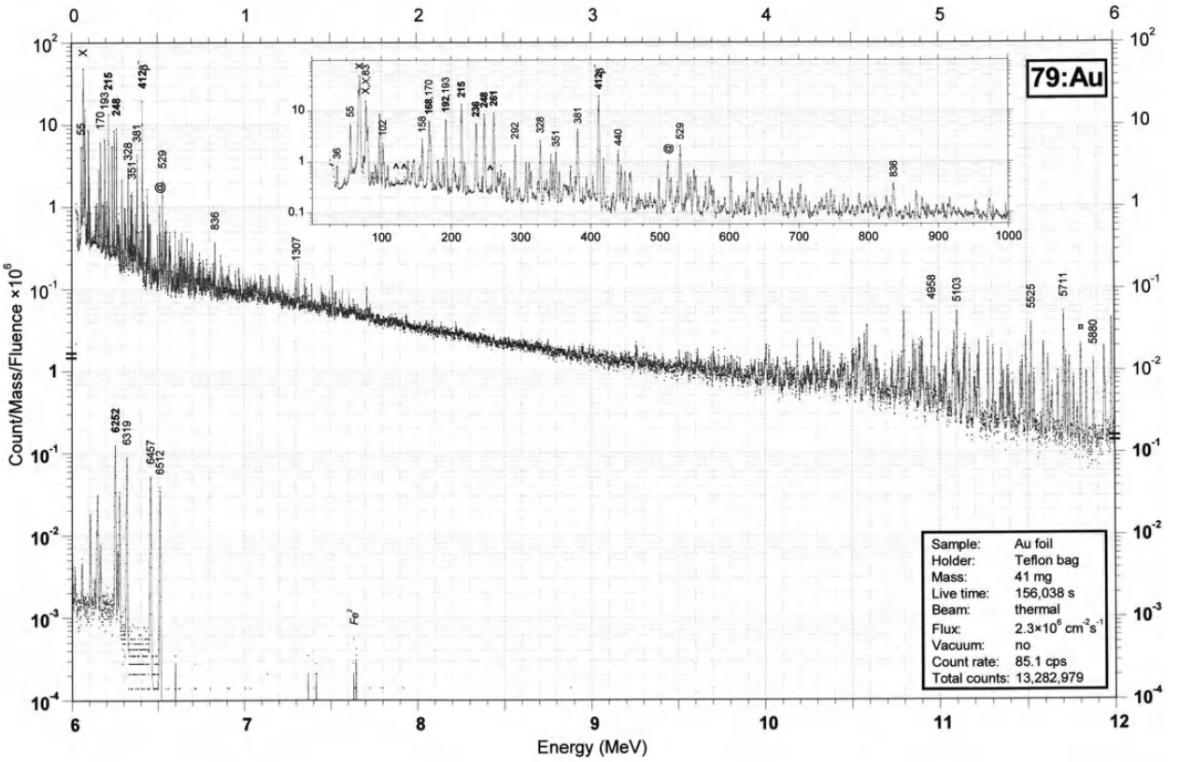

FIGURE 5.4: PGAA spectrum from a light element:^{79}Au

- *Cooling chain:* which is used to get the detector cooled at 77K with the aim to minimize the dispersion current which may destroy the detector and to reduce the thermal noise and ensure a better resolution power. For our experiments we used an Ortec cryo-secure coupled to an X-Cooler.
- *Electronic devices:* used to process the current produced from the incident radiation to

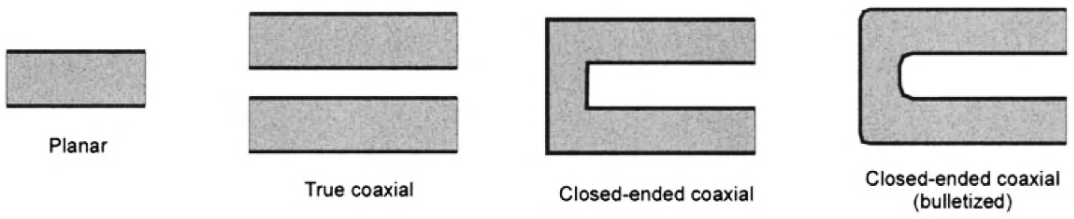

FIGURE 5.5: Classification of the detector geometry for PGAA

the crystal electrical contact from the electron-hole pair which have been created in the depletion zone in the semiconductor.

- *Software:* the electronics output signal is processed by software and produce the spectra that we already discussed. The most used software is MAESTRO it is used to acquire data and even make a preliminary analysis of the peak found.

There exist two kinds of crystal that differ in donor-acceptor concen- tration: the n-type if the donor impurity have the highest concentration, but if the acceptor are predominant the crystal is a p-type. The geometry of the different detectors used for the PGAA can also be classified as follow:

5.3 Neutron Resonance Capture Analysis

The NRCA is a non invasive and non destructive neutron technique based on the analysis of resonances which are essentials for an identification and quantification of elements and isotopes within a sample. This technique exploits the (n;γ) reaction to determine the elemental composition of materials. This technique mostly results in a little radioactivity of the sample analyzed, this is due to the high detection efficiency and the neutron energy spectrum. The energy position of the resonances in the spectrum gives us informations about the specific nuclides so we might say that they can be used to determine the elemental and isotopic composition of materials. NRCA uses a pulsed beam of epithermal neutrons and a time of flight system to recognize resonances of isotopes in a wide energy range. This can be realized at a continuous neutron source involving choppers or at an accelerator-driven neutron source which operates in pulse mode. The use of the choppers put some constraints on the resonances energy range which can be only $\approx 100eV$; to reach higher energies and detect a higher range of elements and isotopes the NRCA experiments have to be carried out to a pulsed neutron source where the neutron beam makes use of a moderator consisting in hydrogen rich material to reach not only high but also a low energy range.

The analysis of the resonances peaks are revealed in a TOF spectrum that is obtained from the detection of γ-ray capture. The parameter of interest for this technique is the time at which the capture event is created, so we need a good time resolution despite neutron sensitivity because we don't care about the neutrons scattered from the sample, but only the time at which the neutron has been captured. The detection system should also be flexible to accommodate large samples with irregular shapes. C_6D_6 and yttrium aluminium perovskite (YAP) scintillators are considered as two of the best detection systems for capture measurements.

One of the advantage of NRCA compared to PGAA is that in a TOF spectrum we can select a TOF region where the contribution due to minor elements is not disturbed by the presence of the main elements. In PGAA experiments the γ-ray spectrum is completely dominated by the response resulting from elements with the largest macroscopic cross section. During the NRCA peak analysis is related to the density of the corresponding nuclide. Following this approach the ratio of masses of the nuclides X and Y, denoted by W_X and W_Y , is derived

from the ration of net areas of resonances μ and λ of nuclide X and Y:

$$\frac{W_X}{W_Y} = K_{\mu,\lambda}\frac{F_\lambda}{F_\mu}\frac{N_\mu}{N_\lambda} \tag{5.1}$$

where N_μ and N_λ are the net peak area of resonances μ and λ. F_λ and F_μ are the corrections for self-shielding due to the neutron beam attenuation in the sample. $K_{1mu,\lambda}$ is the calibration factor. It is determined from calibration samples measurements of known composition using the same experimental set-up and beam conditions.

Scintillators

In general detectors used in this technique are Scintillators. The scintillators are materials that, when hit from nuclear particles or radiation, emit a little ash of light named scintillation. When these scintillations are coupled to a multiplier device, like a photomultiplier, they are converted to electrical pulses which can be electronically counted and analyzed to have information from the incident radiation. The scintillators do not give any information about the energy of the emitted radiation. Generally it consists of a scintillator material (as examples: Li^7 or YAP) optically coupled to a photomultiplier. The radiation passes through the scintillator, excite the ionized atoms and molecules, like Ce^{3+} (which can be found in Li^7 scintillators), causing light emission in visible wavelength ($\approx 400nm$). This light passes through the photomultiplier where it is converted in a weak photoelectron current which is amplified from an electron multiplier system. The current is analyzed from an electronic system. The scintillator give a quick time response compared to others. Which is why they are employed for Time of Flight measurements.

5.4 Interaction of Gamma radiation with Matter

In this section, I will discuss the mechanisms of interaction of gamma radiation with matter. That will lead directly to an interpretation of the features within a gamma spectrum due to interactions within the detector itself and within the detector surroundings. The instrumental detection of any particle or radiation depends upon the production of charged secondary particles which can be collected together to produce an electrical signal. Gamma-ray detection depends upon other types of interaction which transfer the gamma-ray energy to electrons within the detector material. These excited electrons have charge and lose their energy by ionization and excitation of the atoms of the detector, giving rise to many electron–hole pairs. The charged pairs produced by the primary electron are electron–hole pairs. The number produced is proportional to the energy of the electrons produced by the primary interaction. The detector must be constructed of suitable material and in such a way that the electron–hole pairs can be collected and presented as an electrical signal. The main mechanisms of interaction between gamma radiation and detector are :

- **Photoelectric Absorption**
- **Compton Scattering**
- **Pair Production**

Photoelectric interactions are dominant at low energy and pair production at high energy, with Compton scattering being most important in the mid-energy range. It is important to be aware that each of the significant interaction processes results in the transfer of gamma-ray energy to electrons in the absorbing medium, i.e. the gamma-ray detector. In all that follows, therefore, the energy transferred to the electrons represents the energy absorbed by the detector and is, in turn, related to the output from the detector.

5.4.1 Photoelectric absorption

Photoelectric absorption arises by interaction of the gamma-ray photon with one of the bound electrons in an atom. The electron is ejected from its shell with a kinetic energy, E_e, given by: $E_e = E_\gamma - E_b$

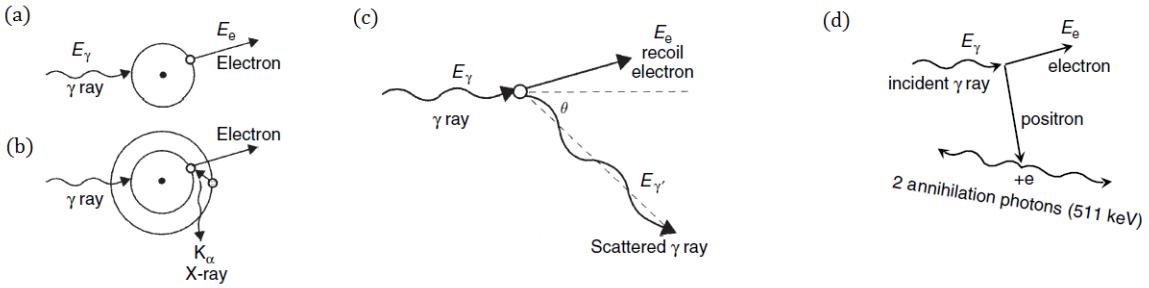

FIGURE 5.6: (a)The mechanism of photoelectric absorption, and (b) the emission of fluorescent X-rays (c) The mechanism of Compton scattering (d) The mechanism of pair production

where E_γ is the gamma-ray energy and E_b is the energy binding the electron in its shell. The atom is left in an excited state with an excess energy of E_b and recovers its equilibrium in one of two ways. The atom may de-excite by redistribution of the excitation energy between the remaining electrons in the atom. This can result in the release of further electrons from the atom (an Auger cascade) which transfers a further fraction of the total gamma-ray energy to the detector**[24]** Alternatively, the vacancy left by the ejection of the photoelectron may be filled by a higher-energy electron falling into it with the emission of a characteristic X-ray which is called X-ray fluorescence (see Figure5.6). This X-ray may then in turn undergo photoelectric absorption, perhaps emitting further X-rays which are absorbed, in turn, until ultimately all of the energy of the gamma-ray is absorbed. (In order to conserve momentum when an electron is ejected, a very small amount of energy must be retained by the recoiling atom. This is very small and can be ignored for all practical purposes.) The energy level from which the electron is ejected depends upon the energy of the gamma-ray. The most likely to be ejected is a K electron. If sufficient energy is not available to eject a K electron, then L or M electrons will be ejected instead. It is normally assumed that photoelectric absorption results in the complete absorption of the gamma-ray.

5.4.2 Compton scattering

Compton scattering (Figure 5.6) is a direct interaction of the gamma-ray with an electron, transferring part of the gamma-ray energy. The energy imparted to the recoil electron is given by the following equation:

$$E_e = E_\gamma - E'_\gamma \quad or \quad E_e = E_\gamma \left(1 - \frac{1}{[1 + E_\gamma(1 - cos\theta)/m_0c^2]}\right) \tag{5.2}$$

Putting different values of θ into this equation shows how the energy absorbed varies with the scattering angle. Thus, with θ= 0, i.e. scattering directly forward from the interaction point, E_e is found to be 0 and no energy is transferred to the detector. At the other extreme when the gamma-ray is backscattered and θ = 180°, the term within brackets in the equation above is still less than 1 and so only a proportion of the gamma-ray energy will be transferred to the recoil electron. At intermediate scattering angles, the amount of energy transferred to the electron must be between those two extremes (Figure 5.7 is a schematic diagram showing this relationship). The inescapable conclusion is that, at all scattering angles, less than 100% of the gamma-ray energy is absorbed within the detector.

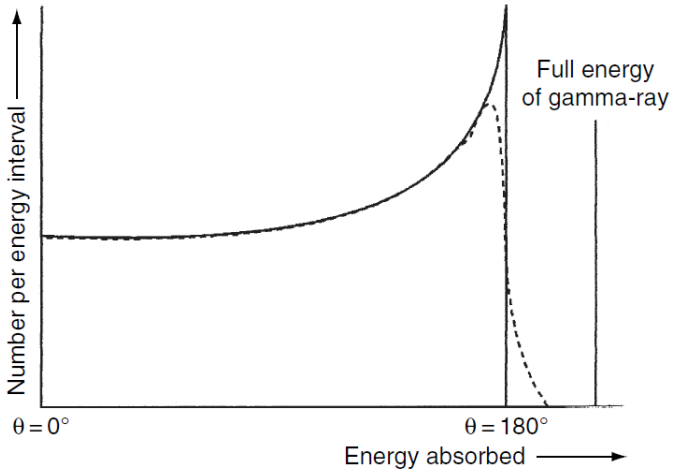

FIGURE 5.7: Energy transferred to absorber by Compton scattering related to scattering angle

Simplistically, we have assumed that the gamma-ray interacts with a free electron. In fact, it is much more likely that the electron will be bound to an atom and the binding energy of the electron ought to be taken into account.

Pair production

Unlike photoelectric absorption and Compton scattering, pair production results from the interaction of the gamma ray with the atom as a whole. The process takes place within the Coulomb field of the nucleus, resulting in the conversion of a gamma-ray into an electron–positron pair. In a puff of quantum mechanical smoke, the gamma-ray disappears and an electron–positron pair appears. For this miracle to take place at all, the gamma-ray must carry an energy at least equivalent to the combined rest mass of the two particles – 511 keV each, making 1022 keV in all. In practice, evidence of pair production is only seen within a gamma-ray spectrum when the energy is rather more than 1022 keV. The electron and positron created share the excess gamma-ray energy (i.e. the energy in excess of the combined electron–positron rest mass) equally, losing it to the detector medium. When the energy of the positron is reduced to near thermal energies, it must inevitably meet an electron and the two will annihilate, releasing two 511 keV annihilation photons. This is likely to happen within 1 ns of creation of the pair and, taking into consideration the fact that the charge collection time of typical detectors is 100 to 700 ns, the annihilation can be regarded as instantaneous with the pair production event. The complete sequence of events is described in Figure 5.6. The net energy absorbed within the detector by the immediate consequences of the pair production event is (with energies expressed in keV):

$$E_e = E_\gamma - 1022 \tag{5.3}$$

To summarize, an ideal 'very large detector' response would contain only *full energy peaks* corresponding to the energies of the gamma-rays emitted by the source. In a 'real' detector, other features appear in the spectrum as a consequence of incomplete absorption of the gamma ray energy. In some circumstances, the loss of precise amounts of energy results in peaks (single and double escape peaks and X-ray escape peaks) or, when random losses occur, in a continuum. The degree of incomplete absorption depends upon the physical size of the detector and the energy of the gamma-ray.

Chapter 6

Characterization of γ-ray background at spallation neutron source beamlines

6.1 Introduction

The VESUVIO ^{6}Li-doped neutron detectors at forward scattering angles were replaced in February 2008 by yttrium aluminium perovskite (YAP)-doped γ -ray detectors.
These YAP provide a much superior resolution and general performance, but suffer from a sample-environment dependent gamma background. Clearly most of the γ-ray background is removed using the foil cycling technique described in the previous chapter but still represent one of the main factors limiting the current VESUVIO capabilities. The gamma background reported in the figure 6.1 limits the signal to background ratio for DINS measurements using YAP scintillators proving that 85% of the signal is due to the gamma background which is useless for the purpose of the experiment . An increase of this ratio would allow to improve the quality of the DINS data with special regards to the modelling of the tail components of the neutron Compton profiles and optimise counting times. YAP scintillators currently in use on the instrument, are set up to operate with a low level discrimination threshold of 600 keV, that is they record photons emitted by the gold analysers with energies above 600 keV. This choice has been done through a study **[5]** based on a figure of merit (F) containing the number of background counts under the recoil peak, the total number of counts and the signal-to-background ratio, using ^{238}U foil as analyzer foil. This shown a significant improvement in S/B has been achieved by using a lower level discrimination (LLD) of the γ energies at about 600 keV. In recent years, it has been chosen to use gold as an analyzer for security and handling issues. It also provides a constant background level due to the analyzer foil radioactivity itself, and the presence of so many close resonances in a beamline with short flight path as VESUVIO leads to the overlapping of the recoil peaks. However energy discrimination of the detected photons is an effective way to reduce the interference of the different background component. Shielding is also another possibility to reduce the background but is not practical due to space limitation.

But understand what these background components are and where they come from is a first important step. This chapter details how this background can be calculated and what are its main components.

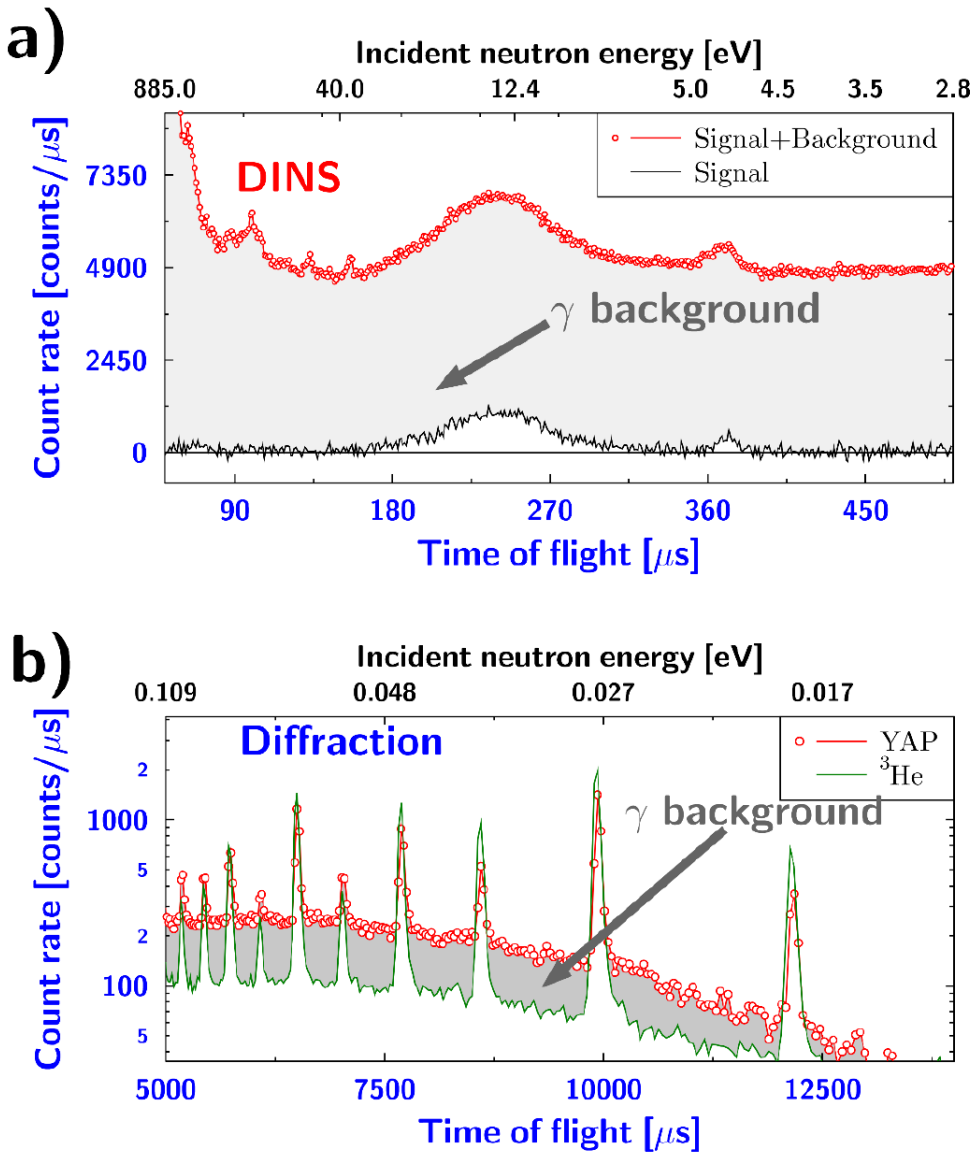

FIGURE 6.1: Foil-in measurement (red circles) and net signal (black line) for a single YAP detector element in a DINS experiment on a water sample on VESUVIO. The grey shaded area is the gamma background. b) Time of flight diffraction data from a copper sample recorded on INES, using a YAP gamma scintillator coupled to a cadmium neutron/gamma converter (red circles), and compared to a measurement on the same sample from a ^{3}He detector placed at the same angular position (green line). The grey shaded area is the gamma background.

6.2 Characterization of the γ background at IMAT beamlines

This study reports the characterisation of the gamma-ray background on IMAT beamline at TS-2 ISIS spallation neutron source. IMAT (Imaging and Materials Science and Engineering) has been designed for a broad range of material science areas where non-destructive and in-situ testing is required. The special features of the instrument will be energy-selective neutron imaging and the combination of neutron imaging and neutron diffraction. An important feature of IMAT will be tomography-driven diffraction. Residual stresses inside engineering-sized samples can be more effectively analysed if the diffraction scans are guided by radiographic data. Diffraction analysis may be indispensable for a quantitative analysis and

physical interpretation of the attenuation features observed in energy-dependent radiography data.There are two imaging cameras available: a gated CCD camera and a time-of-flight capable high-resolution pixel detector. A time-of-flight imaging system taking full advantage of the pulsed source will use a detector based on microchannel plates .Two large pixellated diffraction detectors at 90 degree scattering angles are installed for diffraction analysis.

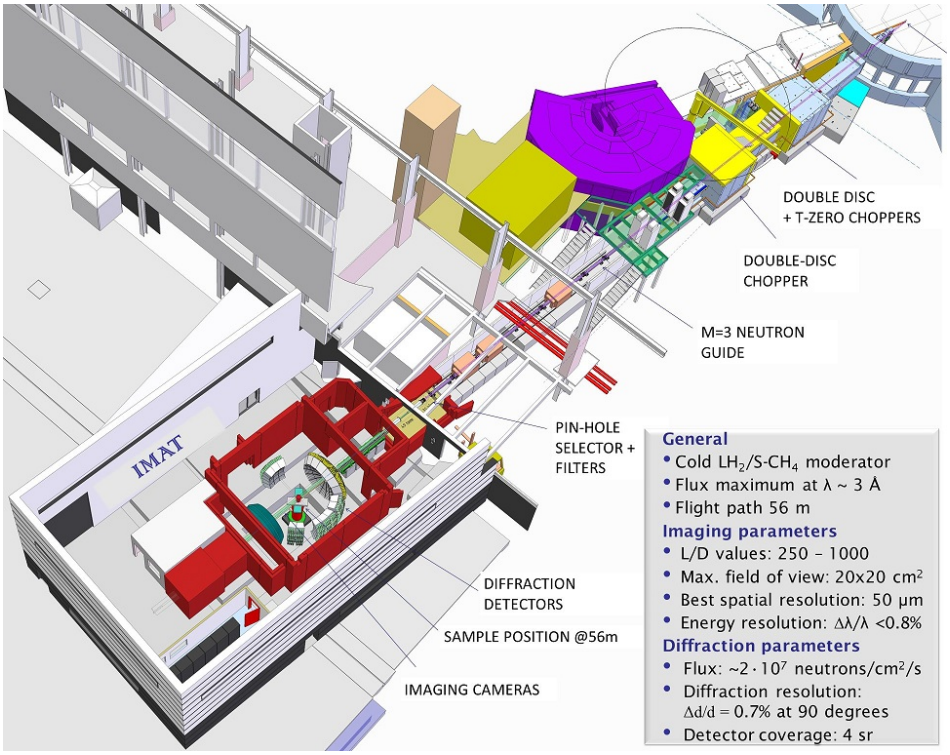

FIGURE 6.2: Panoramic view of IMAT at TS-2.

These measurements of background were made using a HPGe- *High Purity Germanium Detector* and are intended to provide information on the origin of the environmental gammas produces during irradiation with special regards to influence of the background on the measurement of a sample and this is particulary relevant for beamline employing gamma-ray sensitive detectors for example CDD assemblies. It is also important for the choice of the materials for the beamlines construction, for the damaging of the instrumentation installed inside the blockhouse and for users security during experiment. In facilities of this type, where the incident neutron beam at the simple position is mainly moderated, gamma-rays are primarily produced by radiative neutron capture and activation. Furthermore the presence of fast and epithermal neutrons cause γ-ray background and large amounts of shielding and moderating material are required to eliminate undesired neutrons.

6.3 IMAT data analysis

6.3.1 Beam-off and Beam-on background

The aim of the peak detection on the γ spectrum was to identify the chemical elements. The gamma spectrum is a set of counts sorted into channels, which correspond to gamma energy. This histogram must be converted into counts vs. energy so must be done an *energy calibration*. In the simplest linear energy calibration one determines the channel positions of two gamma-ray peaks with accurately known energies. A prompt gamma activation analysis database published by the International Atomic Energy Agency (IAEA) was used to match peaks with chemical elements.

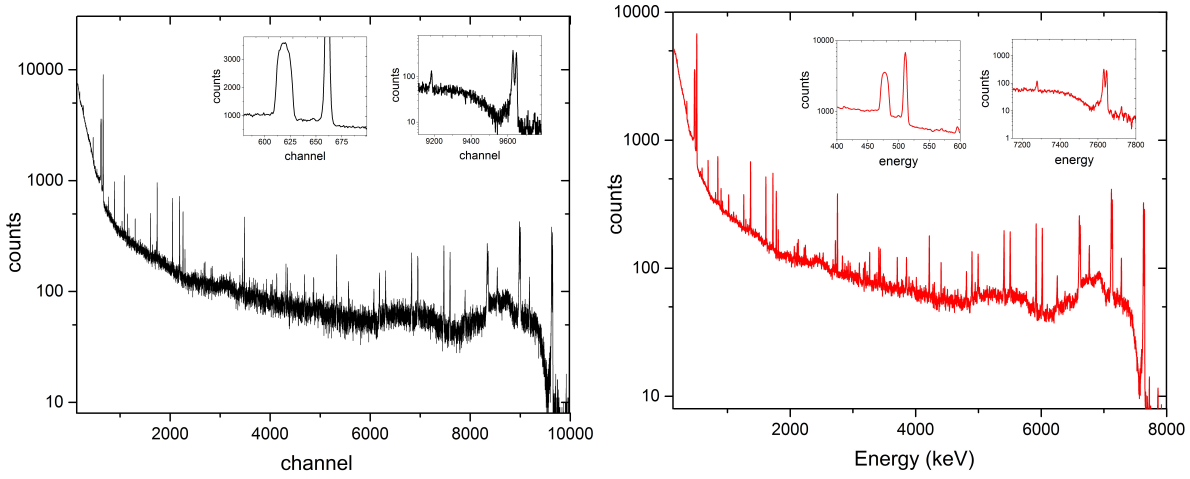

FIGURE 6.3: Pulse height spectrum of a ^{56}Fe radioactive source acquired with the germanium detector (black) and the same spectrum with the insertion of the calibration (red). The included graphs show a zoom of the Boron and Iron peaks region.

Energy calibration of germanium detector has been performed using an Iron sample prompt gamma spectrum (18mm thick). The sample provided three intense γ lines of energies 7279 keV, 7632 keV, 7646 keV. The broad peak around chn.620 can be ascribed to the full energy absorption of γ rays of energy 477.8 keV, which are produced via the reaction $^{10}\mathrm{B}(n,\alpha)^{7}\mathrm{Li}$ and the following decay of ^{7}Li nuclide to the ground state. The nuclide ^{10}B has a high neutron absorption cross-sectionat thermal energies (716 barn) and is used in the beam dump, in the walls of experimental hall and as collimator (B_4C).The peak at 511 KeV is due to the detection of one of the two photons generated in the $e^{+}e^{-}$ annihilation process following pair production.

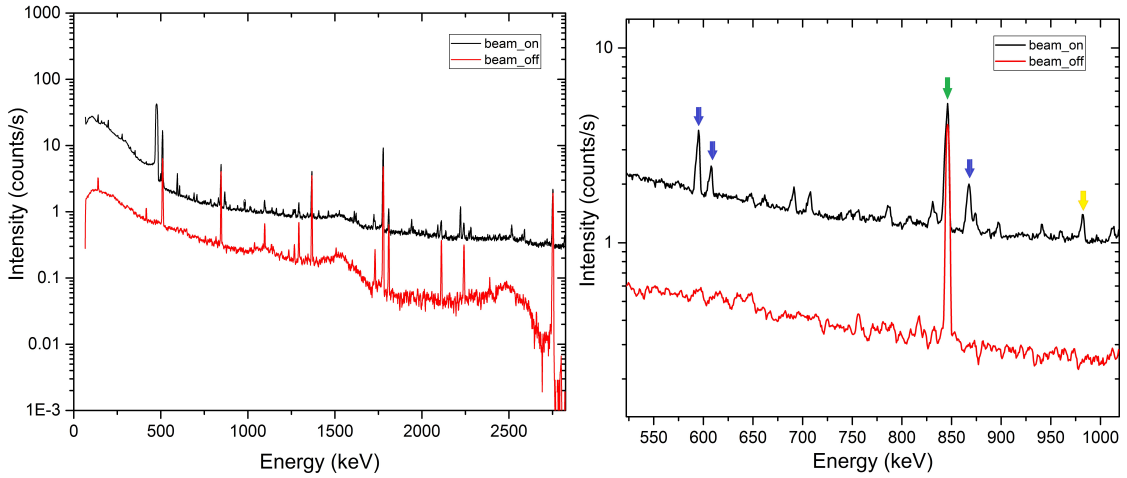

FIGURE 6.4: (a)Comparison of beam-off (red) and beam-on (black) background (b) Blue arrows indicate the peaks associated with the prompt gamma emitted by ^{73}Ge in the process of the neutron absorption. Yellow arrow indicate the prompt peak emitted by ^{27}Al, while the peak of the delayed gamma emitted from the same element is located to the energy of E_{γ}^{d}=1779 keV. Green arrow indicate delayed gamma emitted by ^{55}Mn , in fact present in both spectra.

Using the same conversion between channel-energy, was calibrated the beam-on background (PGAA) then acquired without sample. This was possible because acquisition were made on the same day and using the same condition of gain and dead time of detector. In order to emphasise signatures due specifically to prompt and delayed gamma, is shown the

comparison between beam-on and beam-off background normalized to the time of acquisition. It is clear that in general there is an order of magnitude difference between the baselines of the two spectra, because beam is on and so more events take place when neutrons arrive. There are many more gamma-ray lines in the beam on spectrum than in the beam off, and this is due to the fact that in the beam-on are present both the prompt gamma that the delayed gamma emitted by each element, while the latter are the only component of the beam off spectrum and represent the contribution given by the activation of the elements present inside the beam line. This double check has enabled better labelling of the peaks corresponding to chemical elements.

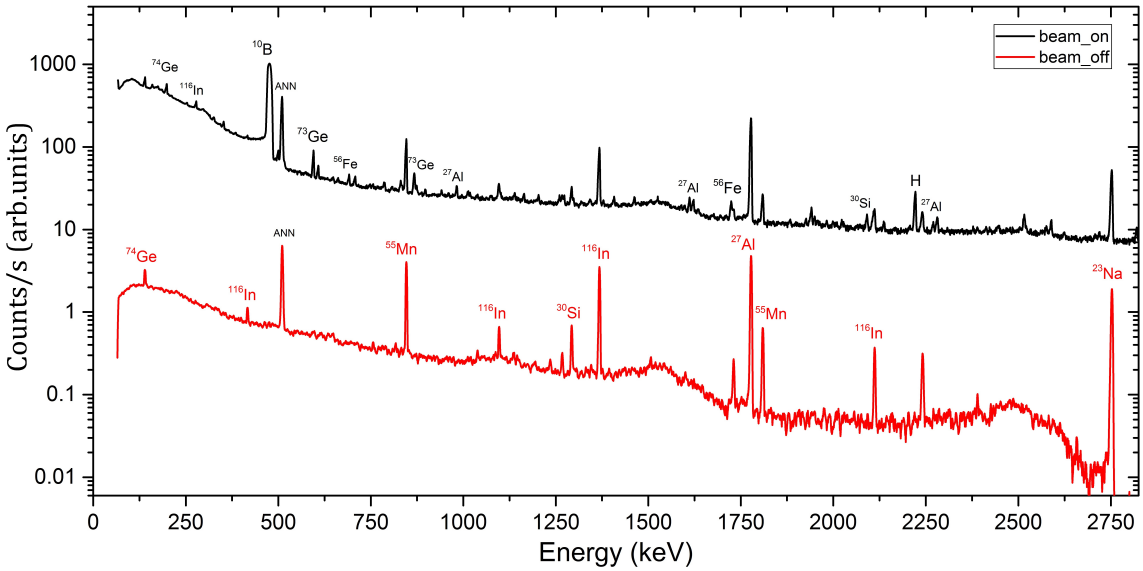

FIGURE 6.5: Element identification to the energies shown in Table 1. The two spectra were shifted along the y-axis for a better comparison. Red and black element identify delayed and prompt gamma respectively. Note that the beam-on background is at least two orders of magnitude higher than the beam off.

For example, the 2223 keV line resulting from the capture of thermal neutrons in hydrogen-containing materials, in particular the blockhouse walls and the beam dump. Neutron-beamline instruments also often contain significant quantities of boron coming from beam dump and pile-hole selector. The germanium peak are from the activation of the HPGe detector. Manganese gamma-ray lines are due to composition of stainless steel grade used in flanges, pipes and collimators. Indium instead commonly is used for metal seals. The gamma-line at 1778 KeV are from the activation of aluminium in the sample tank, flanges and collimator.

Dealing with background radiation normally requires the use of radioisotope-free pure materials with low neutron-capture cross-section and in as small amounts as possible. In order to designing next generation beamlines, special attention was paid to the amount and choice of materials. To substantially reduce the external background radiation incident onto the detectors, one normally needs to attenuate it by placing a passive shielding. An example of shielding material consists of polyethylene and borax mixed with each other. Fast neutrons are moderated in the polyethylene by inelastic scattering on hydrogen atoms while thermal neutrons, captured by boron nuclei, get stopped in the borax, also known as sodium borate, then in containing Na. Gamma peaks due to this element are located at energies 1367 keV and 2754 keV.

TABLE 6.1: Table shows some of the processes involved on IMAT gamma-ray background lines. Database published by Molnar and the International Atomic Energy Agency was used to match peaks with chemical elements. Only gamma-rays with σ_γ above 0.01 barns were considered.

Process	**E_γ^p(keV)**	**E_γ^d (keV)**	**Half life**
$^{74}\mathrm{Ge}(n,\gamma)^{75m}\mathrm{Ge} \xrightarrow{IT} {}^{75}\mathrm{Ge}$	253.2 ± 0.7	140.6 ± 1.4	(47.7 ± 0.5) s
$^{115}\mathrm{In}(n,\gamma)^{116m}\mathrm{In} \xrightarrow{\beta^-} {}^{116}\mathrm{Sn}$	273.3 ± 1.4	417.3 ± 2.0	(54.3 ± 0.2) min
		1097.3 ± 1.1	
		1293.2 ± 1.7	
		2112.6 ± 1.3	
$^{73}\mathrm{Ge}(n,\gamma)^{74}\mathrm{Ge}$ STABLE	596.3 ± 1.4	- - - -	
	867.2 ± 0.4		
$^{27}\mathrm{Al}(n,\gamma)^{28}\mathrm{Al} \xrightarrow{\beta^-} {}^{28}\mathrm{Si}$	983.3 ± 2.1	1778.9 ± 1.8	(2.24 ± 0.05) min
	1623.0 ± 1.3		
	2282.8 ± 1.2		
$^{55}\mathrm{Mn}(n,\gamma)^{56}\mathrm{Mn} \xrightarrow{\beta^-} {}^{56}\mathrm{Fe}$	212.1 ± 1.7	846.9 ± 1.6	(2.57 ± 0.02) h
		1810.7 ± 1.7	
		2112.9 ± 1.8	
$^{23}\mathrm{Na}(n,\gamma)^{24}\mathrm{Na} \xrightarrow{\beta^-} {}^{24}\mathrm{Mg}$	869.2 ± 0.4	1367.4 ± 1.6	(14.97 ± 1.2) h
		2754.4 ± 1.8	

6.3.2 Deactivation of the elements inside IMAT

Another possible analysis which goes beyond the distinguishing the informations from sample to those from background, is figure out the deactivation of these elements within the beamline IMAT. For this purpose, it has been compared the beam off background, which was acquired immediately after closing of the shutter, with two other beam-off measurements performed after 5 and 10 minutes after turning off respectively.

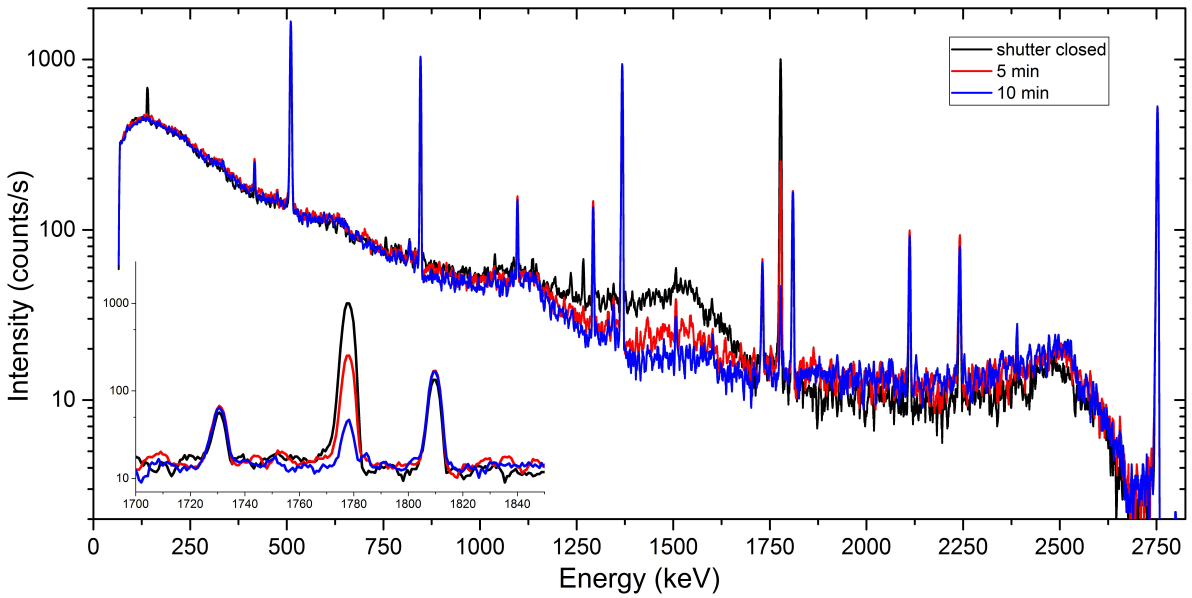

FIGURE 6.6: Gamma-ray background acquired on IMAT a different time. Insert graph shows the decay of Al-peak.

Fig.6.6 shows IMAT background acquired immediately after shutter has been closed and spectra acquired after 5 and 10 minutes. A clear difference is visible in Ge and Al peaks. Germanium peak is absent in 5 min and 10 min spectra because half-life of the state ^{75m}Ge is 47.7s, instead Aluminium half-life is 2.24 min. To confirm this between shutter closed and 5 min acquisition, the peak area was reduced by 25%. So this figure shows how elements around IMAT are being deactivated.

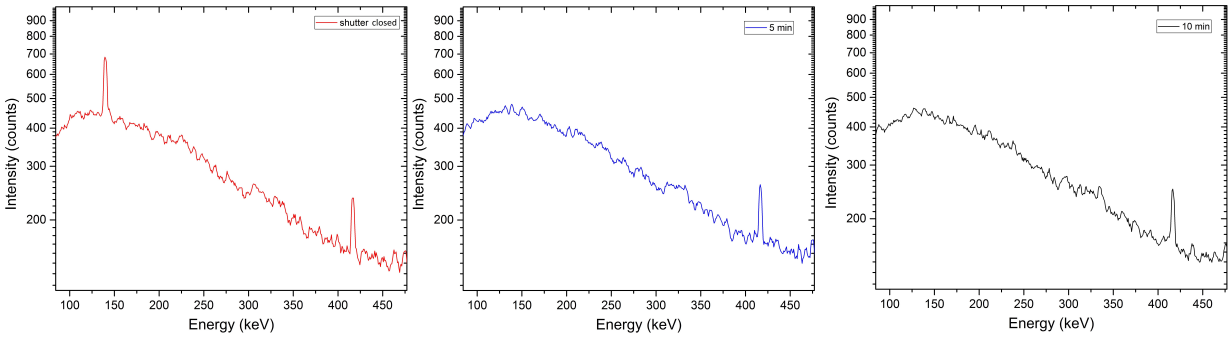

FIGURE 6.7: Variation of the germanium peak. The peak on the right which remains intact even after 15 min is indium-peak which has a decay time of 54.3 minutes.

6.4 Background VESUVIO

The same method for calibration channel-energy has been done on VESUVIO data. The beamline has undergone some changes in recent years that may have altered the chemical composition of the environment surrounding the equipment. These changes certainly influence the measures reflecting on background.

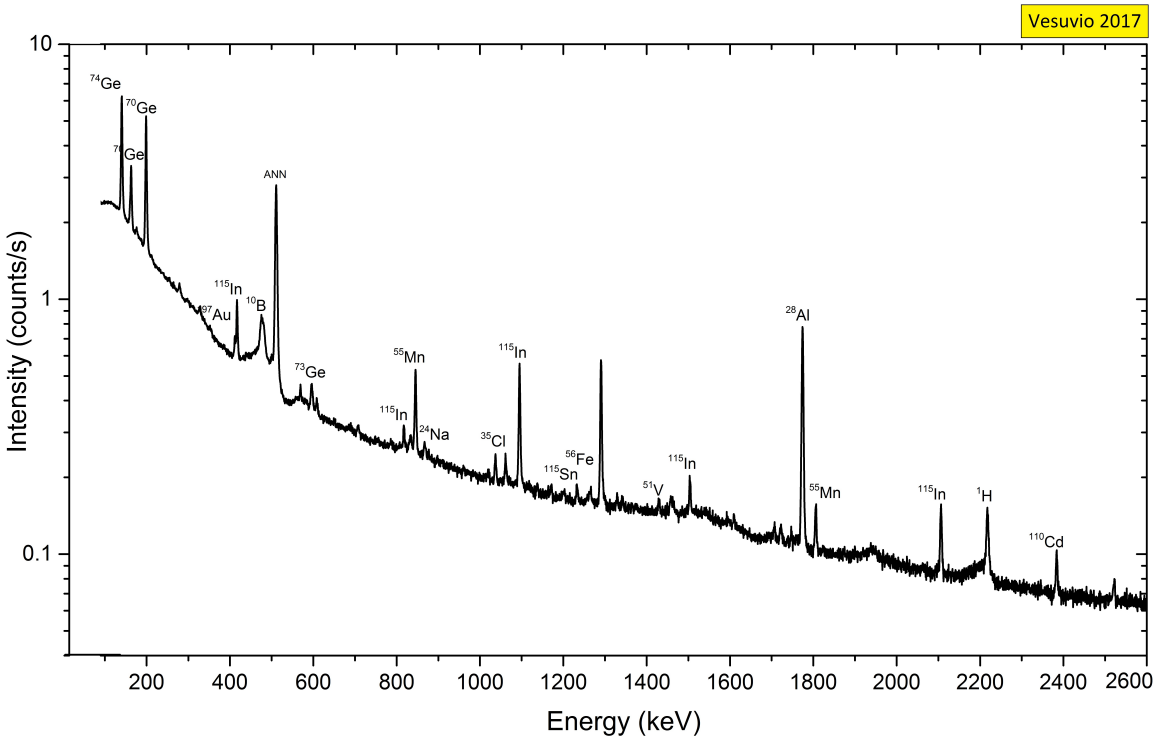

FIGURE 6.8: Measure of 2017 of gamma-ray background on VESUVIO .

6.5 Result and discussion

For the purpose of this thesis, it is particularly important to compare the background on different beamlines. The comparison shows that the gamma background spectrum on VESUVIO increases in the range between 500 keV and 2.5 MeV, as compared to INES and IMAT. In order to characterise and determine the sources causing the increase of background between 600 keV and 2.5 MeV, a measurement of the neutron energy (time of flight) dependence of the gamma background spectrum, would allow to investigate in more details the beamline components which require an optimisation or re-design for background reduction. These measurement are the subject of the forthcoming experiment in May of this year.

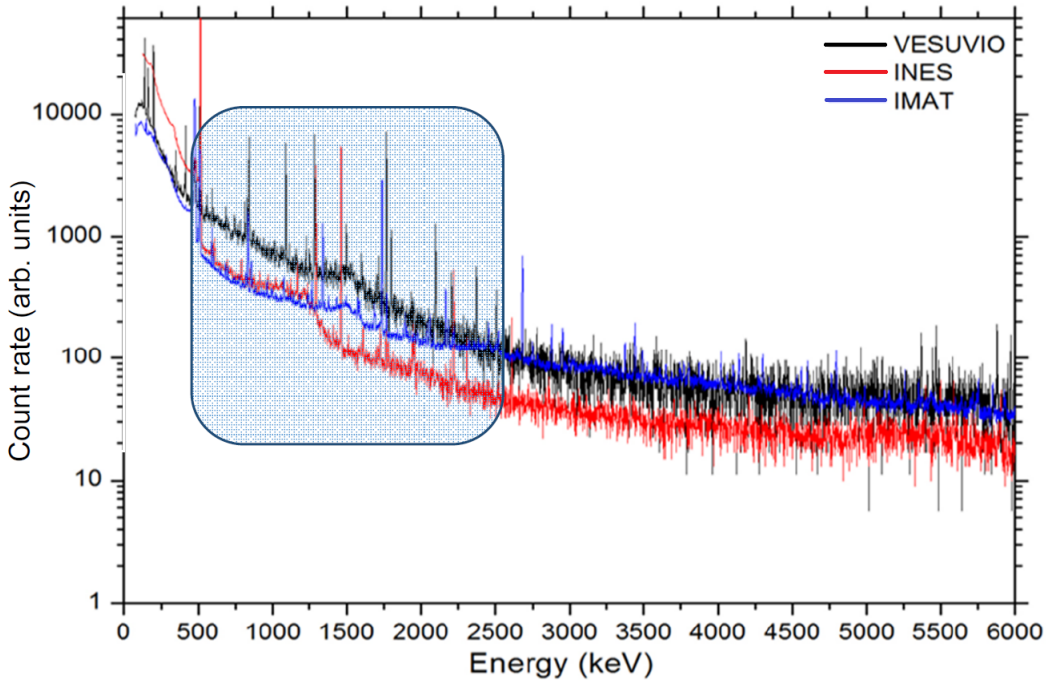

FIGURE 6.9: Gamma background spectra measured on VESUVIO (black line), INES (red line), IMAT (blue line) using a HpGe detector. The shaded box marks the spectral range in which the background on VESUVIO is higher than the INES and IMAT backgrounds.

But why is this important for the purposes of this thesis?

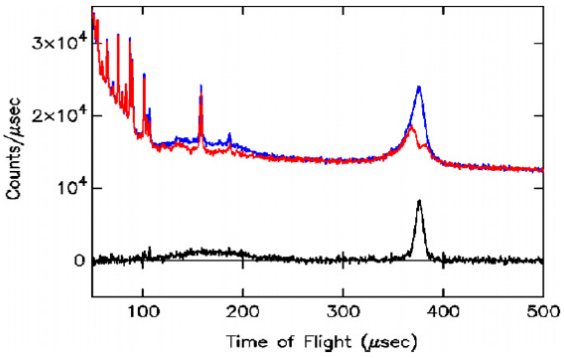

FIGURE 6.10: Data taken from a sample composed of sheets of polythene (CH_2) and lead by a single YAP detector at an angle of 67°. The 'foil out' data are in blue. The 'foil in' data are in red. The difference 'foil out-foil in' is shown as the black line.

Observing Fig.6.10 and therefore the current VESUVIO state of art, the aim of the work is to study gamma emission of the Au analyzer foil, in order to , preserving the counts of the net signal (black line) unchanged, reduce the counts of foil-in and foil-out. This would result in a reduction in the error bars associated with Poisson's counting uncertainty, and then a possible reduction of structured background components (of unexamined and unidentified origin) at low flight times.

Chapter 7

T-PGAA on INES beamline

In this thesis we are going to focus on the analysis of emission due gold analyzer foil when it's in resonance. All measurements were made on INES, as having a primary flight path double compared on VESUVIO provides greater time resolution, and above all this is not surrounded by gold, our main source of investigation.

To characterize our samples we merged two techniques, PGAA and NRCA, giving birth to a third technique called T-PGAA (time resolved PGAA) in which the information of prompt-γ from PGAA and Time of Flight from NRCA are collected simultaneously. Time resolved Prompt Gamma Activation Analysis (T-PGAA) consists in the measurement of gamma energy spectrum induced by the radioactive capture as a function of incident neutron Time Of Flight (TOF), directly related with the incident neutrons energies.

7.1 Experimental set-up

Measurements of the γ-ray spectra on INES were performed using an ORTEC-GMX15 HPGe detector with quoted efficiency varying between 25% at 60 keV and 3.7% at 1332 keV . The detector was placed 1m from the sample position at 90° with respect to the neutron incident beam direction due to sample tank constrains. The HpGe output signal was sent to a channel of a DT5724-4 Channel CAEN digitizer. An attenuator was used to adjust the signal intensity to the input digitizer dynamic range. A copy of the spallation proton pulse signal is available on the INES Data Acquisition Electronics, and was used to synchronize the acquisition with the neutron pulses. This signal, referred to as T_0 from the ISIS source, is a TTL signal that corresponds to the time at which the high energy proton beam hits the target and neutrons are produced for each pulse. The neutron pulses are produced at a fixed frequency of 50 Hz. The T_0 signal was fed to a second channel of the digitizer to obtain the time synchronization.

A recorded event is defined by a signal above a defined threshold. Since the digitizer records a time stamp for each event with 10 ns accuracy, the TOF of each event is computed as the difference of the two time stamps. A trapezoidal filter algorithm is used by the digitizers FPGA to calculate the signal Pulse Height, which is proportional to the energy deposited in the HPGe by the γ-ray. The result of this process is that a bi-parametric acquisition (TOF-photon energy) is possible. In fact, for each signal both the Pulse Height (i.e. the deposited energy) and the neutron TOF are recorded and written to a file.

The data analyzed in this thesis were taken from the group in a previous experiment. I took part to the validation experiment based on the results obtained in this job. Data analysis was carried out through the ROOT software environment, using custom developed macros. The main macros produce a two-dimensional matrix containing counts as function of

- Neutron time of flight that is strictly related to the incident neutron energy
- Deposited γ-ray energy in the HpGe

The gamma energy range obtained from the 2D-Matrix is $10keV \leq E \leq 12MeV$, while the neutron energy range in the 2D-matrix is $0.1eV \leq E_n \leq 68eV$. The data can be represented

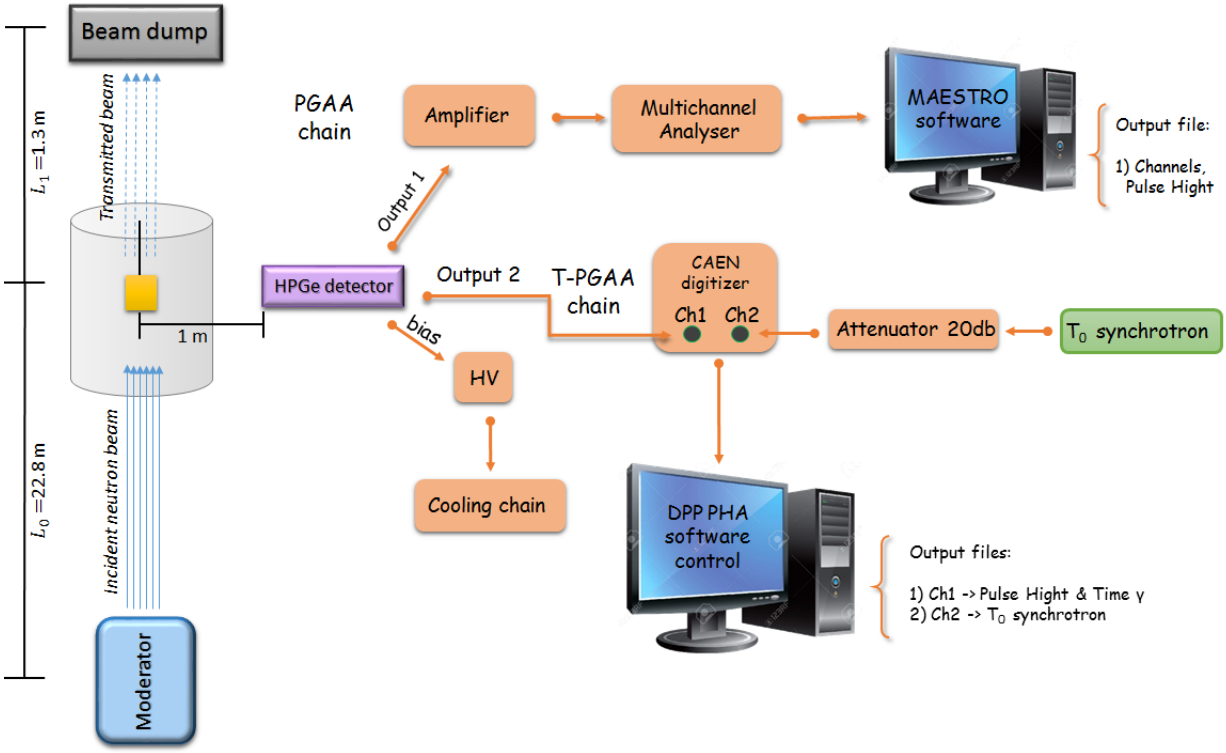

FIGURE 7.1: Chain acquisition for the biparametric data

as a prompt gamma spectrum as a function of the incident neutron energy, the latter defined through the neutron time of flight from the pulsed source to the sample and as an NRCA spectrum as a function of the gamma energy. This 2D matrix have been used in our ROOT macros in a very peculiar way because performing a projection in x or y axis of our spectra we may have both PGAA spectra and NRCA spectra by integrating respectively in TOF or in Energy. Background peaks were labeled and a characterization of gamma background on INES were performed to distinguish it from the samples peaks which have been analyzed in both energy and TOF.

The samples we analyzed in this thesis are:

- a foil sample of ^{197}Au - $2cm \times 2,4cm$ and $10\mu m$ of thickness
- a foil sample of ^{197}Au - $10cm \times 4,5cm$ and $3\mu m$ of thickness

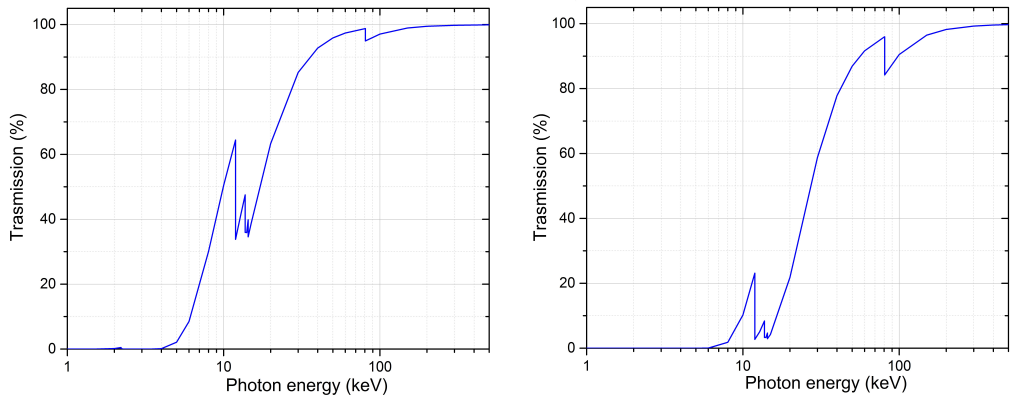

FIGURE 7.2: (a)Photon transmission through a 3μm ^{197}Au foil. (b) Photon transmission through a 10μm ^{197}Au foil.

In order to increase counting statistics and to achieve the best signal to background ratio, the analyser foils were located at the sample position (i.e., in the incident neutron beam), and HpGe detectors was positioned at the closest possible foil-detector distance (1 m) a scattering angle $2\theta \approx 90°$. The foils thickness was chosen in order to ensure both good neutron absorption efficiency and low self-absorption of the emitted photons. The 10μm -^{197}Au foil provides good neutron absorption efficiency, namely about 91% and 37% for the 4.906 and 60.3 eV resonances, respectively; the self-absorption probability of a 100 keV photon emitted from the centre of the foil is only 3%, in the case of 3 μm foil, and 10% in the case of 10μm foil. The energy calibration of the germanium detector was carried out with a gadolinium

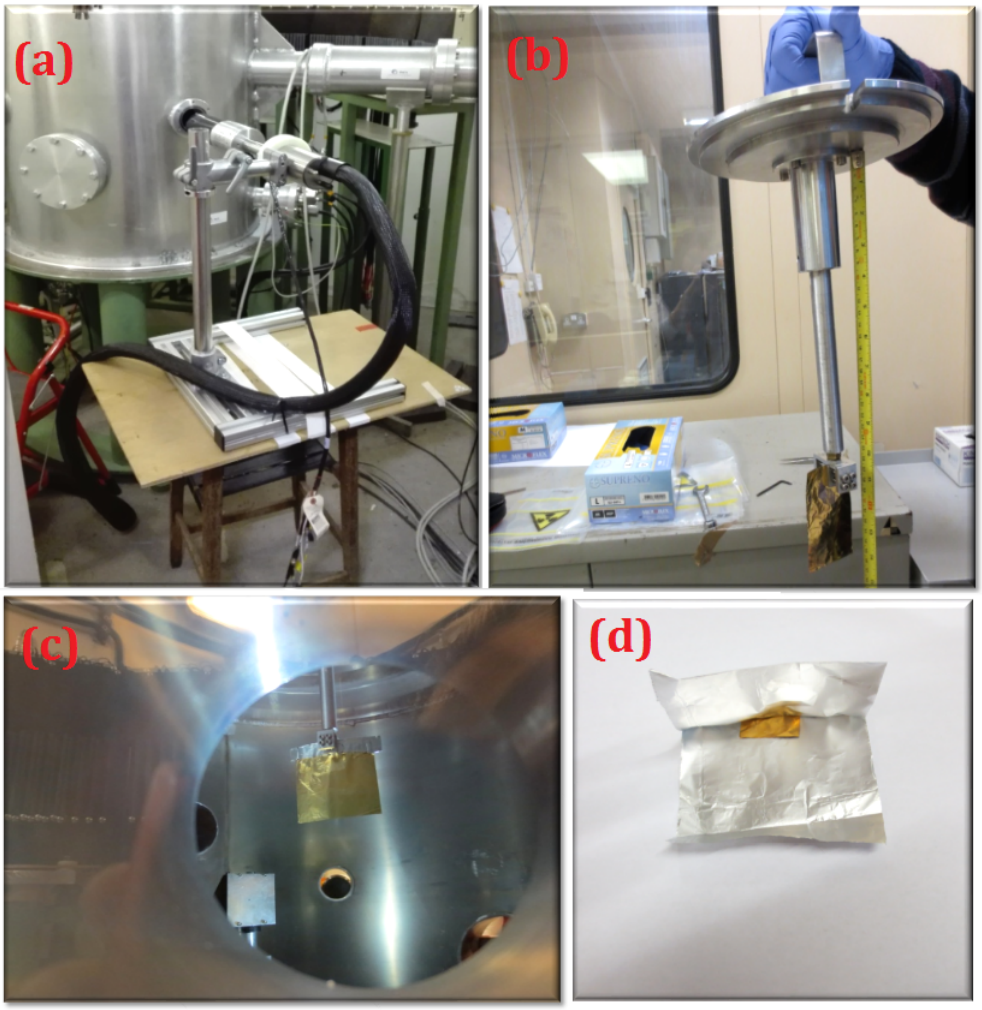

FIGURE 7.3: (a)-(b) HpGe detector and sample positioning (c) ^{197}Au foil - 10 cm$\times$ 4,5 cm and 3 μm of thickness (d) View of the sample ^{197}Au - 2 cm$\times$ 2,4 cm and 10 μm of thickness from the flange opening

sample which present intense peaks spreads all along the energy range. The detector gain was set up to obtain a photon energy window 3.5 keV < E < 497 keV in 16383 channels. This was done intentionally to use the ^{10}B peak at 478 keV as a reference for calibration of detector. Acquisitions in continuous (Ortec) as well as biparametric (Caen) were both carried out.

The second information needed before collecting data from our samples, was a background characterization of the INES beamline in order to distinguish the informations from the sample to those from the background. We see the presence of elements like indium, manganese, iron, germanium (detector activation) and boron which is one of the most important neutron absorber as B_4C.

After the measurement of the background spectrum, the data from the samples mentioned before was collected. Below the figures representing the PGAA calibrated spectra of gold and

Element	Energy (keV)	Channel
^{157}Gd	79.5	2595
	88.9	2900
	181.9	5929
	199.2	6473
^{10}B	477.6	15573

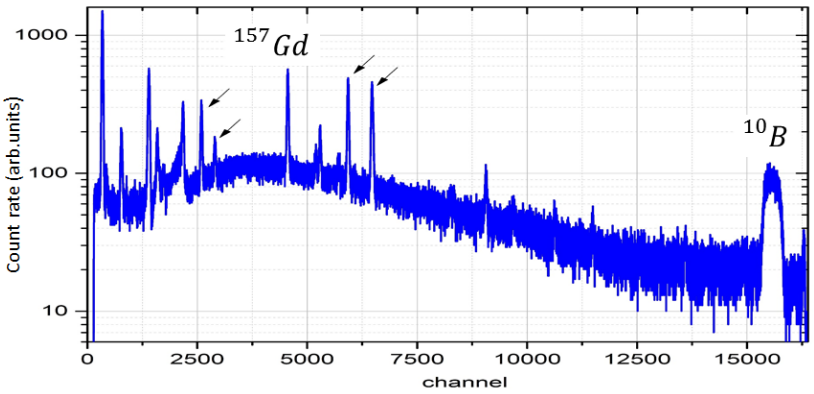

FIGURE 7.4: (a) Channel and energy matching used for calibration (b)γ spectrum acquired with Gd sample in channel units. The arrows indicate the Gadolinium peaks, while the right peak is of the Boron

the signal/background comparison. Both spectra were normalized at acquisition time.

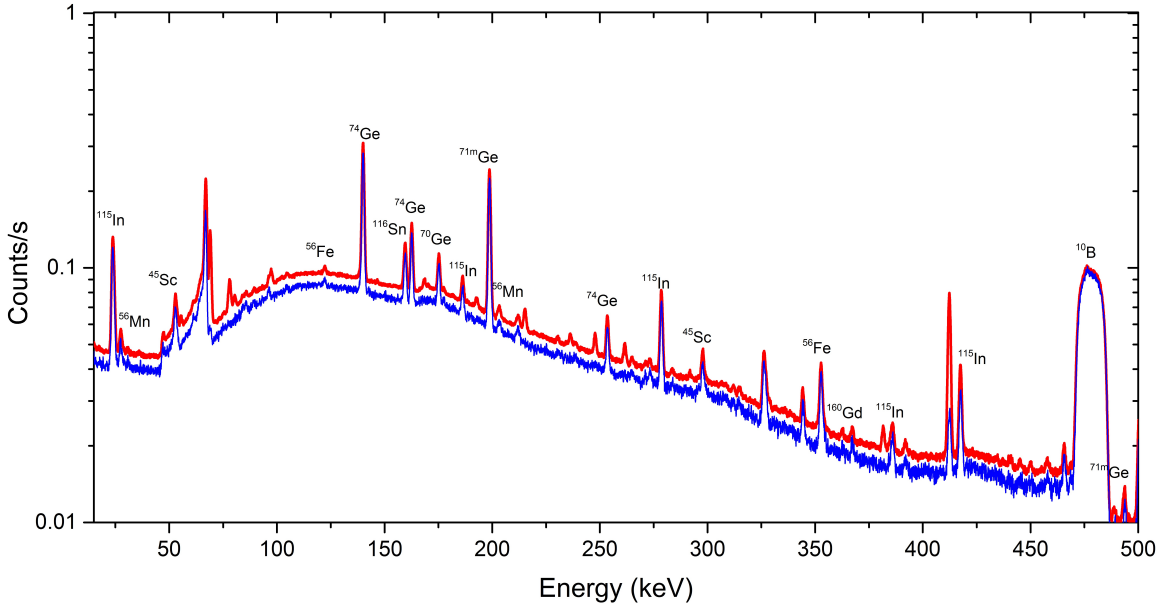

gr

FIGURE 7.5: PGAA labeled spectrum from INES background (blue line) and PGAA spectrum of Gold (red line).

The sample spectrum contains background contribution arising from both prompt and activation spectra which often shows peaks overlapping with the sample γ-ray lines. All the tabulated peaks are present and their intensity is consistent with the expected intensities according to the radiative cross section. The emission of gamma radiation is not the only possible process for de-excitation of a nuclear level and so not all peaks are associated with this process. Our spectra show indication of another process for de-excitation : Internal Conversion (IC). The sample was irradiated for about 15 hours to get good statistics and after this an activation measure was done. The sample was taken out of the tank and placed in front of the germanium. In the resulting spectrum shows in fig.7.7 we notice an intense peak at 411 keV and less intense peak at 66, 68, 77 and 80 keV. The most intense peak is the delayed-γ emitted by ^{198}Au in the β^- decay. The peaks around 70-80 keV are due to the internal conversion process mentioned earlier and will be better explained in the next paragraph.

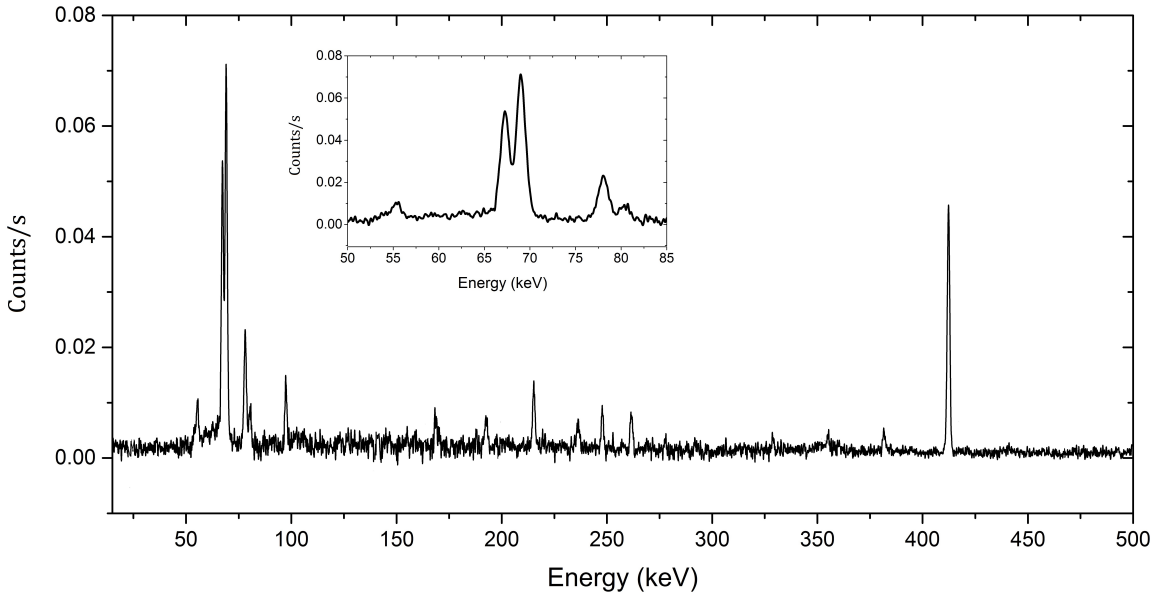

FIGURE 7.6: PGAA spectrum of Gold with background subtraction. The insert graphic is a zoom in the range 50 keV- 85 keV. The different color arrows indicate the different process associated with the production of that peak.

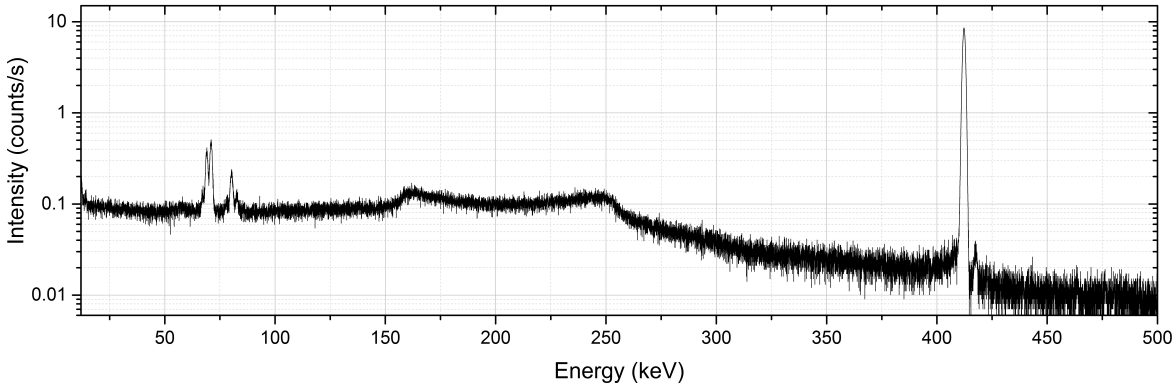

FIGURE 7.7: Gold activation spectrum. The intense peak at 411 keV is the delayed γ emitted by ^{198}Au. The less intense peaks are related to the internal conversion process.

7.1.1 Internal Conversion

In this process, the energy available is transferred to an electron, which is ejected from the atom. This is called an *internal conversion electron*. It is mono-energetic, having an energy equal to the transition energy less the electron binding energy and a small nuclear recoil energy. Measurement of the distribution of electron energy (i.e. an electron spectrum) would reveal peaks corresponding to particular electron shells, such as K, L and M. Loss of an electron from a shell leaves a vacancy and this vacancy will be filled by an electron dropping into it from a higher shell. Thus, as with electron capture, an array of X-rays and Auger electrons will also be emitted. However, note that because IC is a mode of de-excitation and there is no change in Z, N or A, the X-radiation that is produced is characteristic of the parent isomeric state. Both 'parent level' and 'daughter level' are the same element. This is in contrast to electron capture, where the X-rays are characteristic of the daughter. Internal conversion operates in competition with gamma-ray emission, and the ratio of the two is the *internal conversion*

TABLE 7.1: Table shows the processes involved on neutron absorption and the energy of gamma rays emitted. Only γ-rays with σ_γ above 1 barn were considered. **[6]**

Process	E_γ**(keV)**	σ_γ (b)	E_γ**(keV)**	σ_γ (b)
^{197}Au(n,γ)^{198}Au	55.181	2.90	214.971	9.0
	82.356	2.3	236.045	4.1
	97.250	2.1	247.573	5.56
	158.436	1.25	261.404	5.3
	168.334	3.60	291.724	1.05
	170.103	1.66	328.484	1.48
	192.392	3.9	381.199	3.0
$^{198}\text{Au} \rightarrow {}^{198}\text{Hg} + e^- + \bar{\nu_e}$	411.804	95.58	**Half life**	2.695 d

TABLE 7.2: X-ray energies. The intensity were normalized to $I(K_{\alpha 1})$=100. Due to the unmeasurably small energy differences, it is practical to group together K_β transition as: $K_{\beta 1'} \rightarrow K_{\beta 1} + K_{\beta 3} + K_{\beta 5}$ and $K_{\beta 2'} \rightarrow K_{\beta 2} + K_{\beta 4} + ...$

Process	$E - K_{\alpha 1}$ **(keV)**	$E - K_{\alpha 2}$ **(keV)**	$E - K_{\beta 1'}$ **(keV)**	$E - K_{\beta 2'}$ **(keV)**
$^{198}\text{Au}^* \rightarrow {}^{198}\text{Au}^+ + e^-$	68.81(100)	66.99(58.7)	77.86(35.2)	80.16(9.3)

coefficient,α:

$$\alpha = \frac{number\,of\,IC\,electron\,emitted}{number\,of\,gamma-\,rays\,emitted} = \frac{N_e}{N_\gamma} = \frac{(N_e)_K}{N_\gamma} + \frac{(N_e)_L}{N_\gamma} + ... = \alpha_K + \alpha_L + \alpha_M + ... \tag{7.1}$$

This may be subdivided into α_K,α_L, etc., where electrons from the individual K and L shells are considered. Values of α depend on the transition energy and atomic number. In broad terms, α increases as the half-life and Z increase, and as ΔE decreases. Also the characteristic X-ray are labeled as K, L, M or N to denote the shells they originated from. Another designation alpha (α), beta (β) or gamma (γ) is made to mark the X-ray that originated from the transitions of electrons from higher shells. Hence, a K_α x-ray is produced from a transition of an electron from the L to the K shell, and a K_β x-ray is produced from a transition of an electron from the M to a K shell, etc. Since within the shells there are multiple orbits of higher and lower binding energy electrons, a further designation is made as α_1, α_2 or β_1, β_2, etc. to denote transitions of electrons from these orbits into the same lower shell *(Siegbahn notation)*.

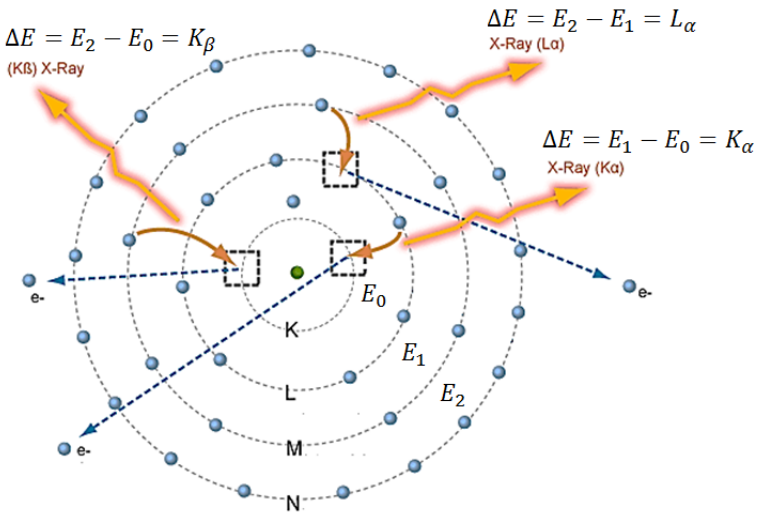

FIGURE 7.8: Schematic representation of Internal conversion with X-rays emission.

7.2 Biparametric acquisition

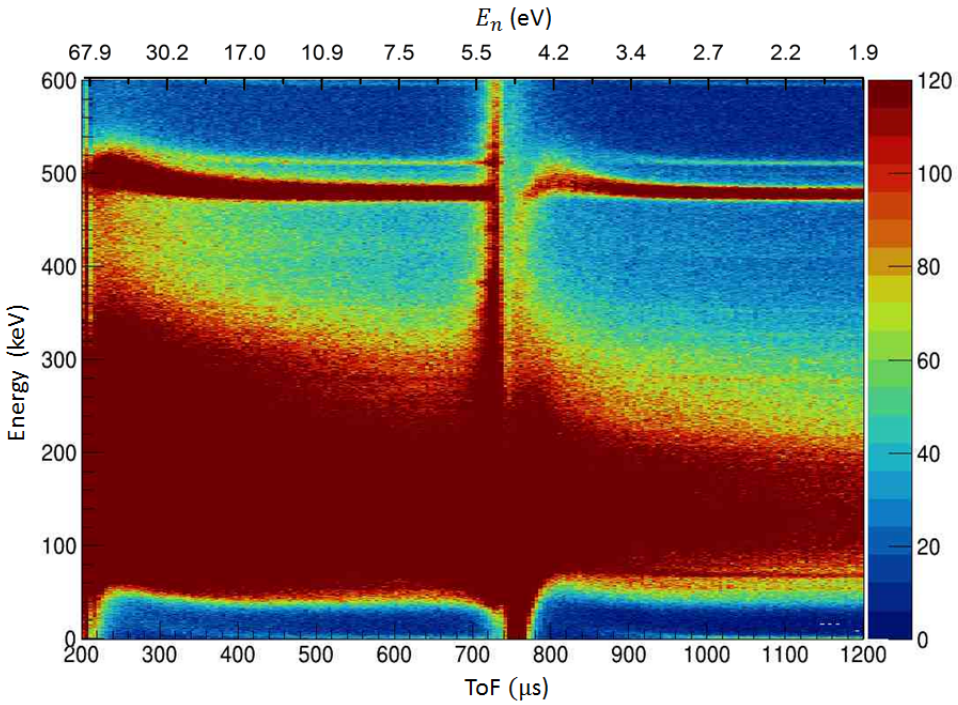

FIGURE 7.9: Intensity map of the bi-parametric (γ-ray energy vs. time-of-flight) spectrum measured with the HPGe detector for Gold foil.

A separate calibration on the biparametric acquisition data was done, because the gain in acquisition channel ORTEC covers a energy range of 10 keV < E_{photon} < 12 MeV, while the CAEN acquisition channel covered 0-500 keV energy range. The biparametric data presented in this thesis refer to two runs acquired with the HpGe detector for 16 h at an average proton beam current of 157 μA. A specific task of thesis was to optimise the implementation, within the ROOT environment, of routines outlines in **[100]** These allowed to elaborate the output

data of the acquisition chain and to build 2D histograms. A typical *biparametric spectrum* relative to the ^{197}Au - 3 μm foil is shown in Fig.7.9. From the inspection of the intensity map it is possible to follow the TOF evolution of the individual γ-ray lines such as for example the 511 keV annihilation and 478 keV boron capture across the resonance and out of resonance region. The correspondence between energy and time of flight is given by:

$$ToF(\mu s) = 72,3 \cdot \frac{L_0(m)}{\sqrt{E_n(eV)}} \tag{7.2}$$

On INES the 4,9 eV resonance is located at 744 μs while the 60,3 eV resonance at 212 μs. We can notice the increase in the count rate in the resonance zones, especially for the lowest neutron energy resonance, since the first resonance (in time of flight) is not perfectly visible. In fact, the detector set-up used has a limitation in the measurable before 180 μs, where it is "drowned" by the rapidly increasing in the count rates. Cuts along the vertical axis provide time of flight-resolved PGAA spectrum ,reported in fig.7.10, while cuts along the horizontal axis provide gamma energy-resolved NRCA spectrum, reported in fig.7.11. For example, it is possible to derive a PGAA from electron Volt neutrons, as compared to a PGAA from thermal neutrons.

So information that can be extracted from the collected biparametric data is dual: by introducing a selection window on the time (γ energy) axis and projecting the data along the other axis one obtains the γ energy (neutron TOF) spectrum corresponding to the selected neutron TOF (γ energy) window. This has been used for data analysis with a two-fold aim. The first aim is to characterise the HpGe pulse-height response to the absorption of resonant and non-resonant neutrons in the analyser foils . The second aim is to show that it is possible to improve the signal to background ratio of the TOF measurement by selecting specific γ energy regions. An example of the potential of the present technique is shown in fig.7.12. For instance, the pair of energy spectra were generated by selecting 30 μs wide time windows centred around t=744 μs, i.e around the resonance, and in the region 900μs-930μs, i.e. an off-resonance interval. What we see is the net increase of the peaks due to gold in-resonance radiative absorption , which are barely visible off-resonance.

Interestingly the boron emission peak a 478 keV, shows a decrease for in-resonance neutrons as compared with off-resonance. Indeed the main mechanism that we believe been at the origin of the boron peak is due to radiative capture from ^{10}B in the beam stop and block house surrounding area like walls and collimator. Off-resonance gold absorbs less neutrons, so the number of transmitted neutrons that hit the surrounding walls is higher. This process is most noticeable for boron, which is the highest cross section element among those contributing to the background.

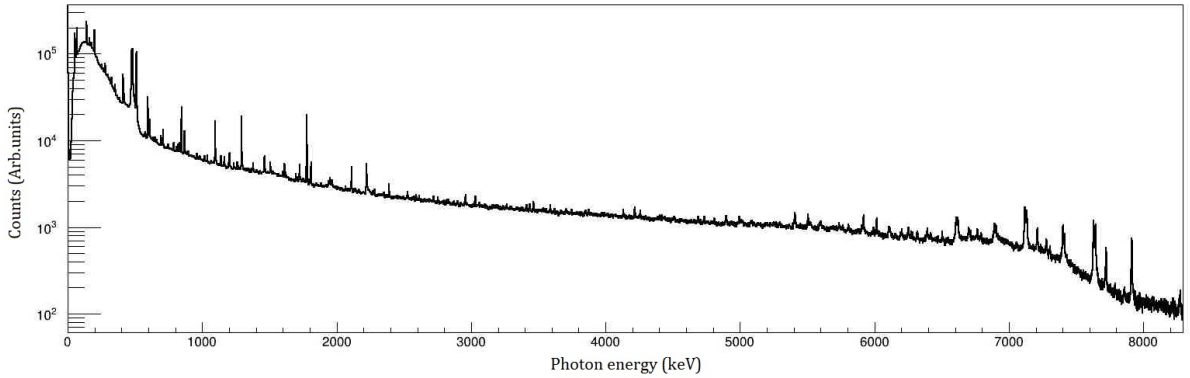

FIGURE 7.10: PGAA spectrum using entire neutron energy range.

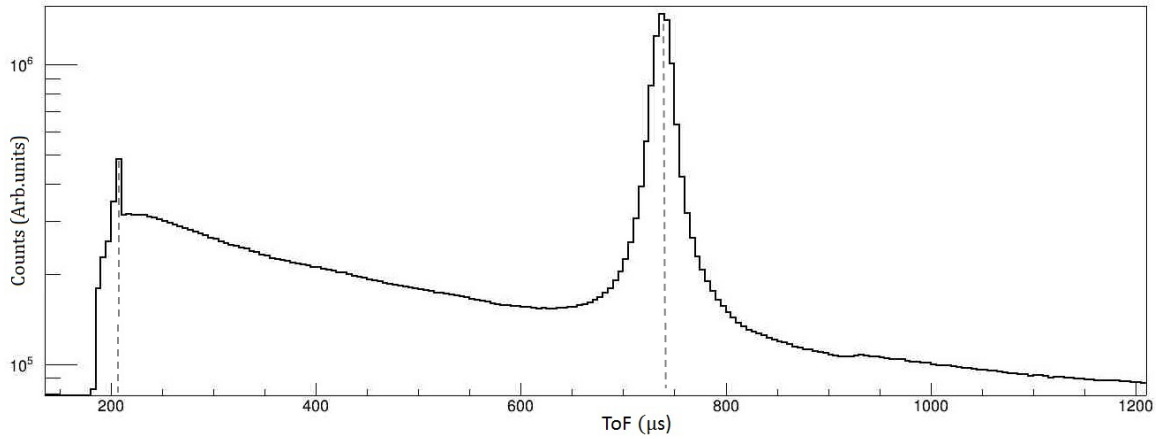

FIGURE 7.11: Projection of ^{197}Au biparametric data on the time axis (NRCA). The result is the neutron time of flight spectrum. The vertical lines indicate the calculated position of the resonances ; The peak around 744μs represent the E_n=4.906 eV neutron resonance. The peak around 212μs represent the E_n=60.3 eV neutron resonance.

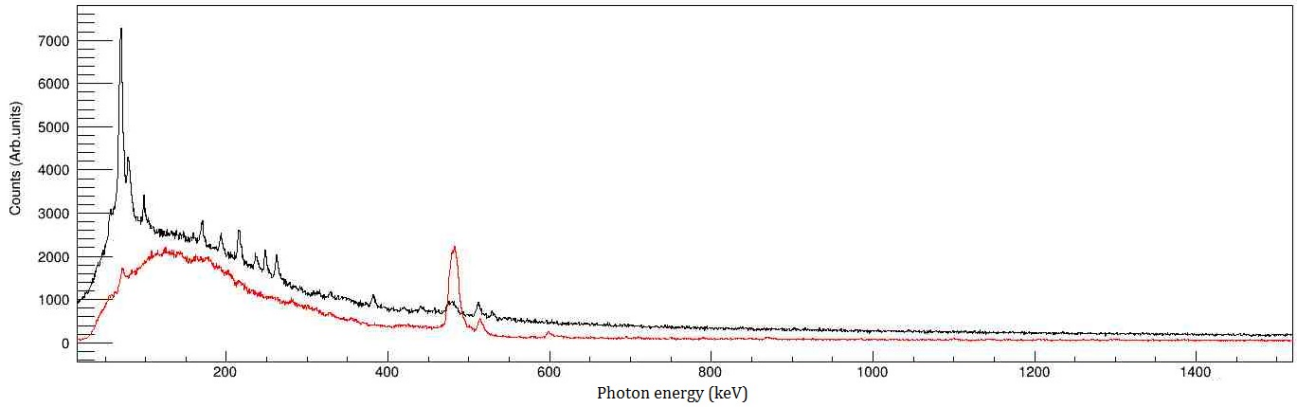

FIGURE 7.12: Projection of gold biparametric data on the energy axis for specified time interval. Black line corresponding to a time windows around the neutron resonance and red line around off-resonance region. The chosen time interval are : 723μs <t< 753μs corresponding to an energy range 4.79 eV < E_n < 5.18 eV (resonance) and 900μs<t<930μs corresponding to an energy range 3.14 eV < E_n < 3.35 eV (off-resonance).

7.2.1 ^{10}B peak analysis

The behavior of the boron peak on and off resonance can be quantified. If σ_t(E) is the total Au cross-section, The decrease on the intensity of a beam that impacts on a thickness dx and hit ndx atoms per unit area will be

$$dI = -I\sigma_t n dx\,; \qquad I = I_0 e^{-\sigma_t n x} \tag{7.3}$$

where

$$n = \rho_{Au}\frac{N_a}{M} \qquad \rho_{Au} = 19.32\frac{g}{cm^3} \qquad M = 196.966\frac{g}{mol} \tag{7.4}$$

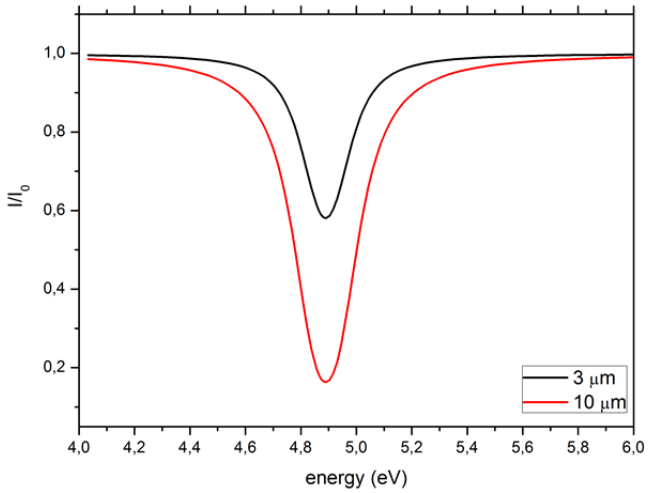

FIGURE 7.13: The figure shows the variation of I/I_0 with the energy of neutron incident for the two different thicknesses of the gold foils.

Gold 3μm

Observing fig.7.13 we notice that for E_n=4.9 eV the ratio I/I_0=0.58 (58% of the beam is transmitted) and for E_n =5 eV the ratio I/I_0=0.81 (81% of the beam is transmitted). Off resonance we have 40% more beam transmission as compared. Then making a very narrow cut (5μs wide) around 738μs (on) and 730μs (off) and performing a gaussian fit (fig.7.14) with subtraction of an exponential background we can calculate the area under the boron peak in both cuts. The ratio derived from the fit-area off-resonance is 35% larger than the fit-area on-resonance , confirming the calculated theoretical value.

Gold 10μm

Observing fig.7.13 we notice that for E_n=4.9 eV the ratio I/I_0=0.15 (15% of the beam is transmitted) and for E_n =5 eV the ratio I/I_0=0.53 (53% of the beam is transmitted). This is consistent, because the larger the thickness the larger is the absorption, at the same energy value. So on resonance the beam is attenuated 3 times more than off resonance. The areas under the fit confirm this value as seen in the figure7.15.

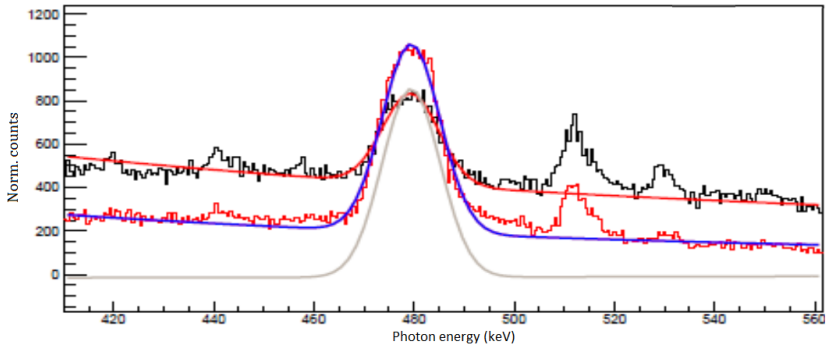

FIGURE 7.14: Zoom in the energy range around 478 keV for 3μm gold foil. Blu line is the fitted peak for off-resonance cut. Red line (continuous) is the fitted peak for on-resonance cut. Grey line in the fitted peak (off) with background subtraction.

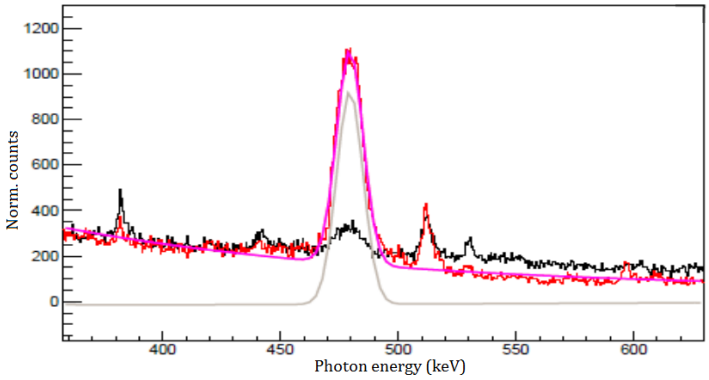

FIGURE 7.15: Zoom in the energy range around 478 keV for 10μm gold foil. Pink line is the fitted peak on-resonance and grey line is the same with exponential background subtraction.

7.3 Result and Discussion

Returning to Figure7.12, which has a central role in this work, we see how the two spectra essentially have the same overall features. Exceptions are the peaks that follow neutron-capture when gold is on-resonance. Thinking of the purpose of this thesis is important to understand whether this contribution is dominant so that it can provide information on the optimal operating point of the YAP detectors on VESUVIO.

The biparametric maps reported in fig.7.17 are constructed so that 1 bin corresponds to 1 μs, this make the data less manageable, but allows better resolution in ToF. The acquisition with the HpGe detector covers an energy range of 10 keV -12 Mev, for our purposes it is useful to look only at 10 keV - 1500 keV energy range since over 1500 kev the efficiency of YAP detectors decrease below 10%. Above the 511 keV which corresponds to the peak of annihilation, there are no significant contributions to the biparametric map which is flat in counts rate in this range. In the 0-600 keV energy range there are the greater contributions. This energy range is discarded by VESUVIO's YAP detectors. The fig.7.18 can provide information on the optimal operating point of the YAP detectors on VESUVIO. When we approach to incident energy of 4.9 eV, we note intense spots corresponding to the energies of photons emitted by gold and correspond to those listed in the previous page.

The most intense spot is situated in the 60 keV -80 keV energy range as shown in fig.7.19. This peaks, located at 68.81 keV, and is neighbouring peak at 66.99 keV can be identified as K-shell X-ray lines from Au foils emitted after interval conversion process. The same is for the peaks at 77.86 keV and 80.16 keV. These peaks could be too sharp, and do not contribute to an actual signal increase measured by the YAP. To test it, we must consider the area under

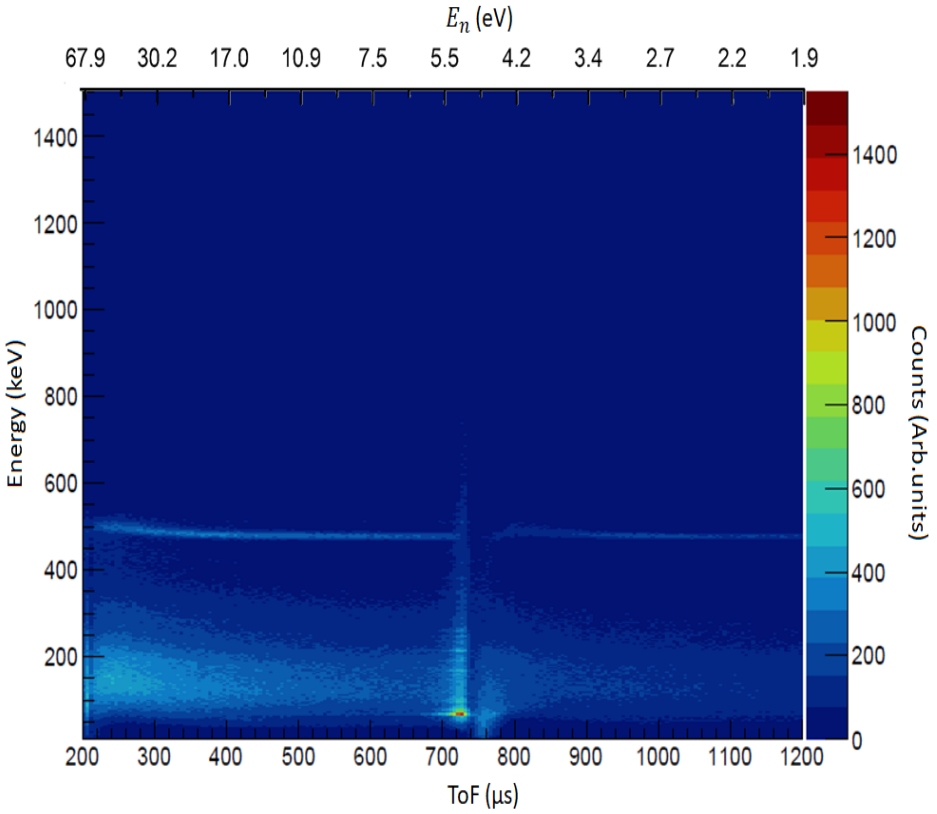

FIGURE 7.16: Count intensity map of the bi-parametric spectrum in the range 200 μs<ToF<1200 μs and in photon energy 10 keV<E<1500 keV.

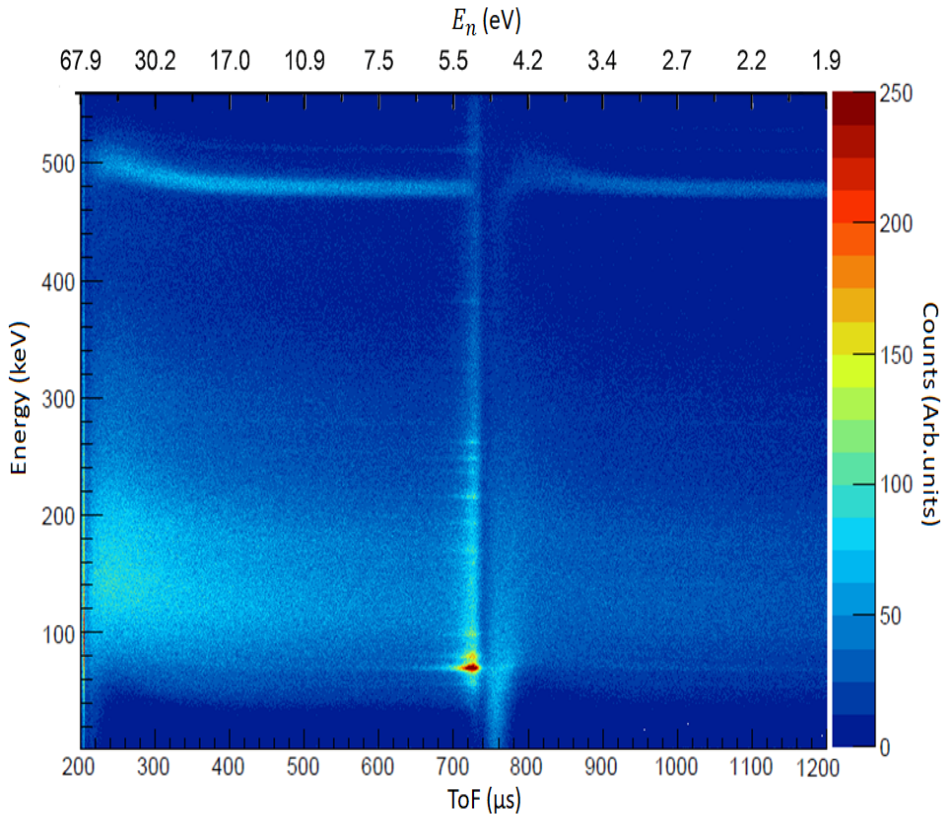

FIGURE 7.17: Zoom on the bi-parametric spectrum in photon energy range 10 keV<E<550 keV.

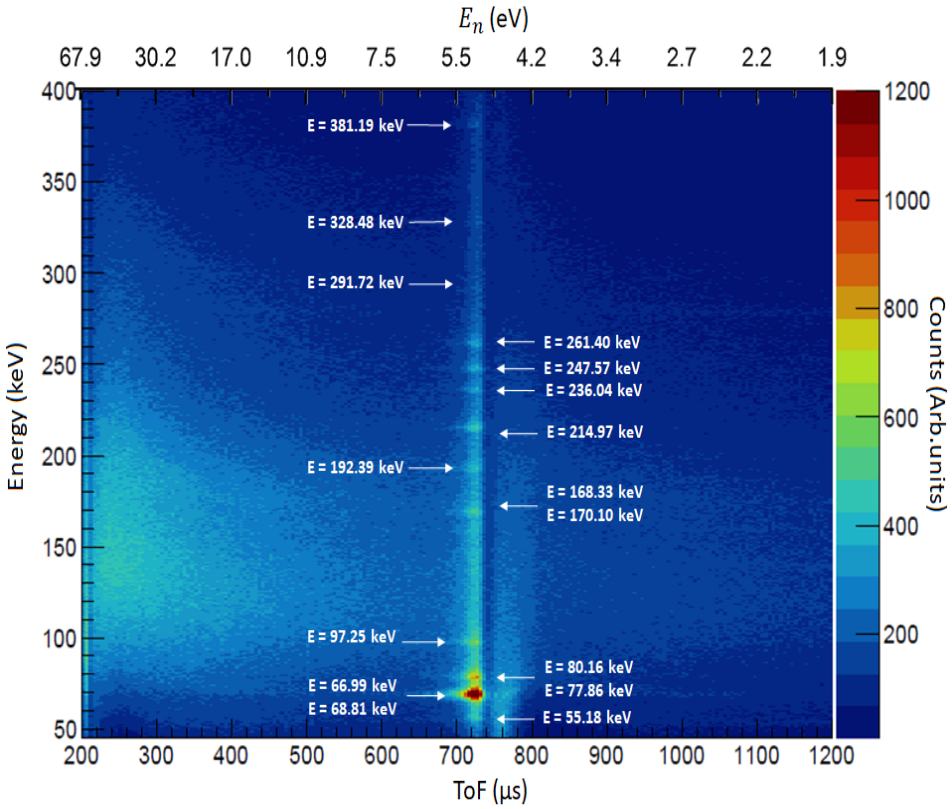

FIGURE 7.18: The most intense zones positioned exactly on the resonance line identify the peaks due to gold. Are found at the same energies as shown in table 7.1 and 7.2. Some peaks are overlapping.

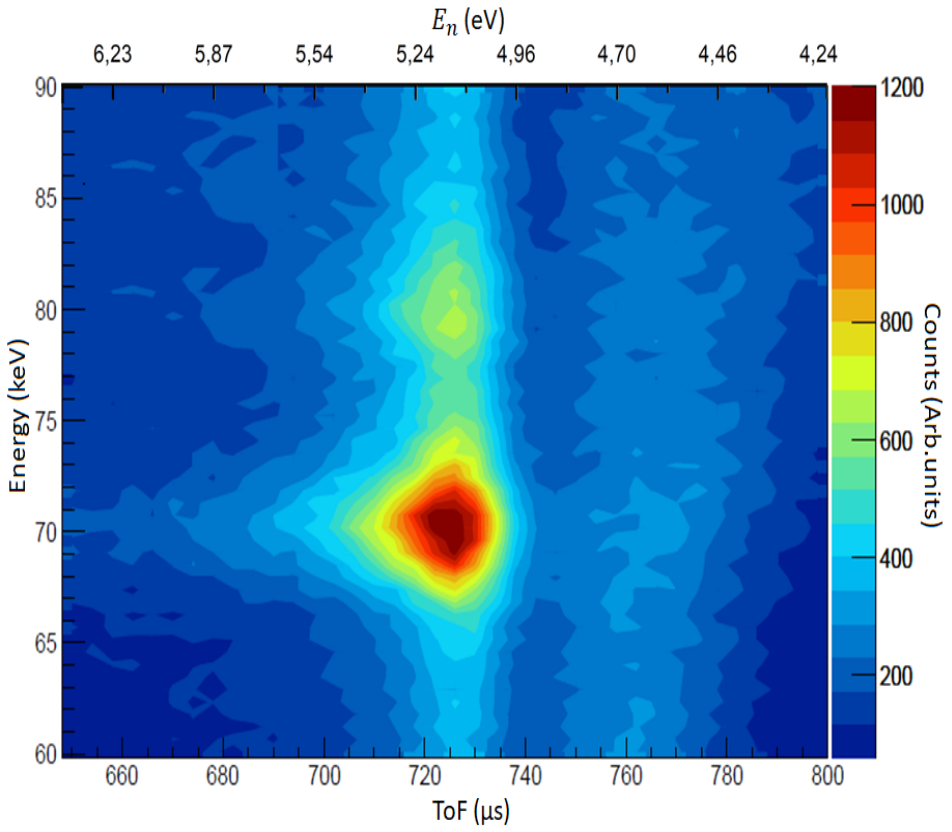

FIGURE 7.19: Zoom in the energy windows 60 keV<E<90 keV. The greater intensity is finds around the 70 keV when the gold is on-resonance i.e around 738 μs.

the photon energy spectrum vs counts as a quantitative indication of the photons spectral contribution to the observed counts for each ToF bin.

By plotting the gold cross section as a function of the time of flight, we see that the width around 738 μs resonance is 10 μs. The biparametric map has been cut into slices of 10 μs in the entire range 200-1200 so as to "slice" the incident neutron beam on the sample. By projecting on the energy axis, we can observe the spectrum generated solely by this neutron selection and separate the contribution of the resonance according to the energy of photons.

These areas have been normalized to the incident neutron flux in the slice considered. The incident flux on INES was not yet characterized, and we got it by dividing the absolute incident flux on VESUVIO by 4, having considered the different primary flight path between two.

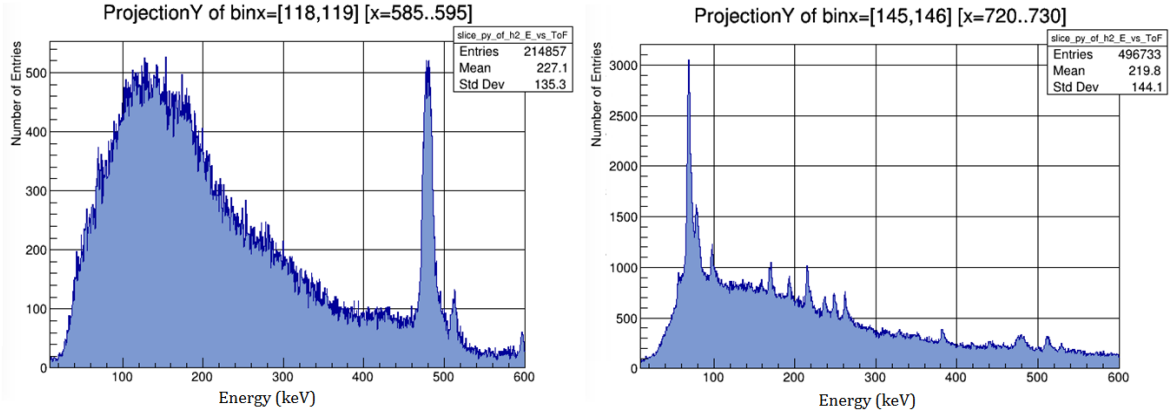

FIGURE 7.20: Example of gamma spectra resulting from biparametric cut in two different ToF intervals. (a) 585 μs < ToF < 595 μs (b) 720 μs < ToF < 730 μs.

Figure7.20 shows two different cuts in the intervals 585 μs < ToF < 595 μs and 720 μs < ToF < 730 μs. We notice how much the number of entries (and therefore the events that our detector is recording) is greater in the second cut so close to the resonance energy, and the gold contribution emerge from the background. In first cut the number of entries are below 500 while in second cut the number of entries arrives up 3000. The blue colored zone represents the spectrum area and then the total number of captured events.

Figure7.21 representing a discrete step projection onto ToF. We note that the value of the normalized areas as a function of the time of flight slice reproduce the shape of the resonance. The contribution between 0-600 keV represents almost the entire contribution to the total area (0-1500 keV). What the YAP currently measuring are blue areas, so most of the signal is discarded. This confirms that the present LLD is not advantageous to the measure, and that the contribution given by the analyser foil when is on-resonance is dominant. We can define a "gain" parameter such as the ratio between the in-resonance spectrum area and the off-resonance spectrum area, i.e. the ratio between peak value and plateaux value for each energy range.

$$Gain = \frac{on - resonancespectrumarea}{off - resonancespectrumarea} \tag{7.5}$$

Fig.7.23 shows the gain calculated in different LLD thresholds such as, 0-1500 keV (which corresponds to no threshold), 100-1500 keV, 200-1500 keV, 300-1500 keV, 400-1500 keV, 500-1500 keV, 600-1500 keV (actually LLD thresholds).

This gain has a value about 14 when no threshold is imposed and get down to 1.5 when a 100-1500 keV LLD is set. Between 100 keV and 200 keV LLD thresholds there isn't big difference, because in the photon energy range 100-200 keV there isn't important gold peaks contributions. We are discarding the peaks at 214, 236, 247, 261 keV which have high cross-sections, and so the gain decrease. The gain increase instead with a 500 keV LLD respect to

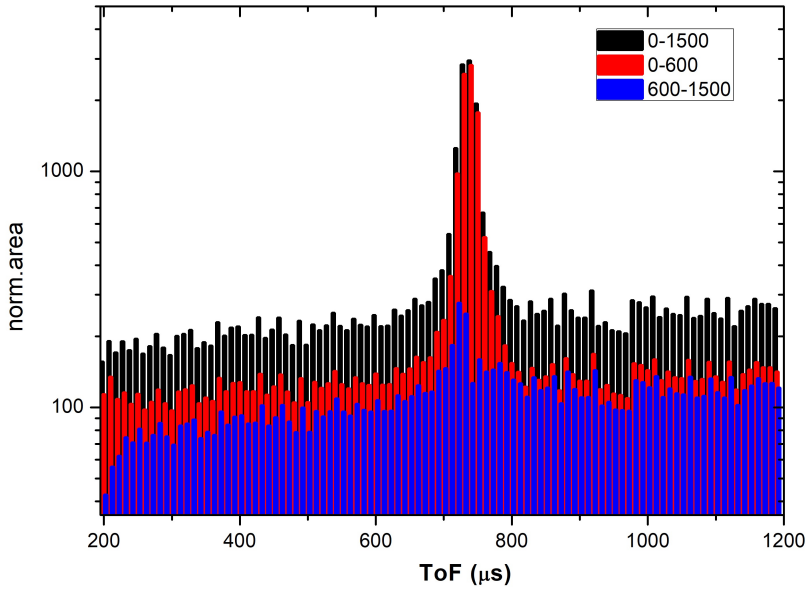

FIGURE 7.21: Values of the areas below the photon energy spectra in different selected energy regions. These areas have been normalized to the incidence neutron flux.

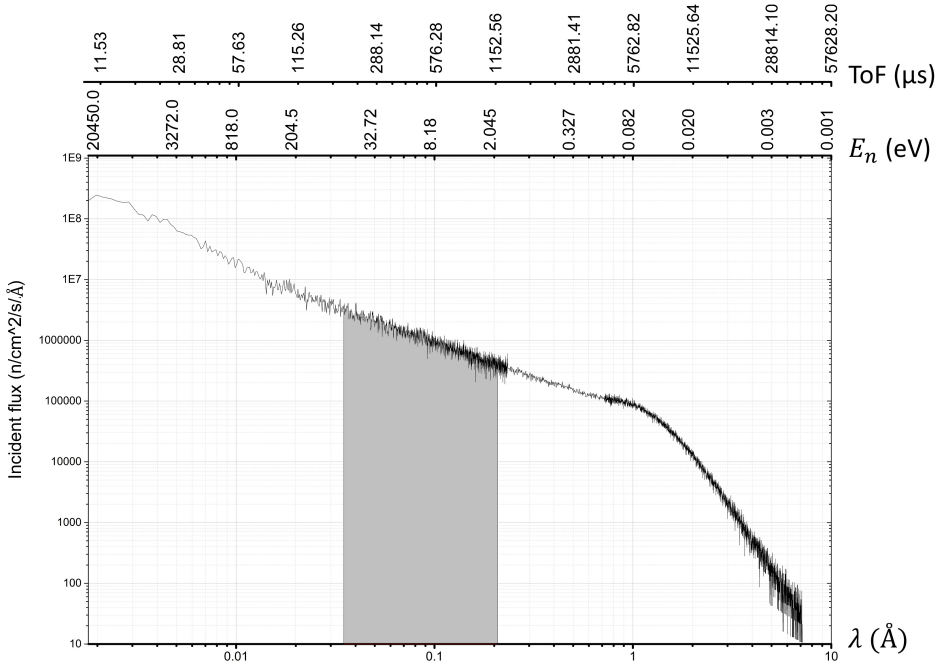

FIGURE 7.22: Neutron incident flux on INES beamline. The colored area is the portion of neutrons considered i.e. 200 μs< ToF< 1200 μs.

400 keV LLD because of the boron peak contribution . The same thing between 500 and 600 keV because of the annihilation peak.

To optimization of gamma detection it would be better to have a higher-level-discrimination (HLD) between 0-600 keV but for now this is prevented with the instrumentation available on VESUVIO. To confirm this we have investigated the possibility of introducing an energy window with the aim of improving the signal-to-background ratio (s/b) and generating the corresponding neutron time-of-flight spectrum.

The result, compared in a semi-log plot with the TOF spectrum obtained without any

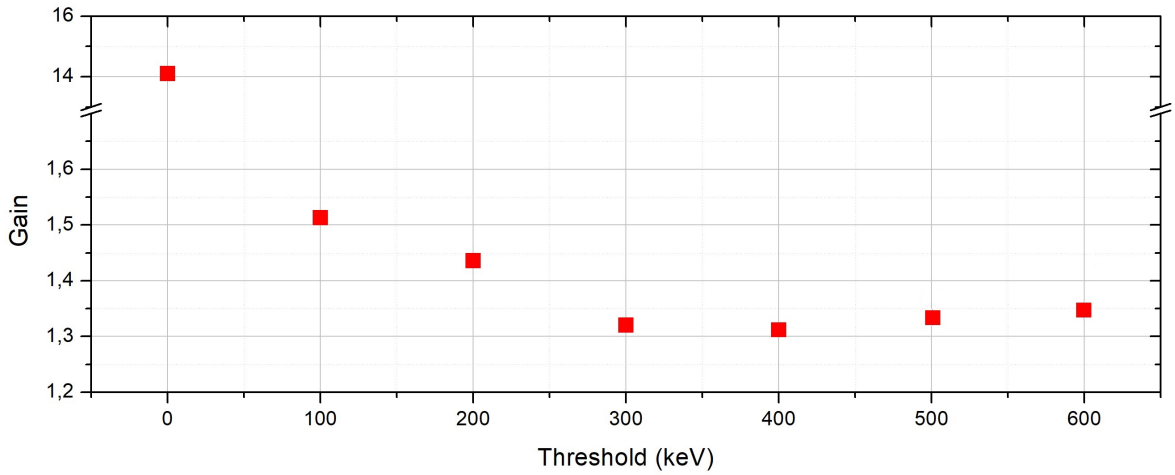

FIGURE 7.23: Gain calculated for different LLD threshold. Red dots indicate where the low level is set.The upper level is set to 1500 keV for each thresholds.

energy selection indicates that a s/b improvement can be obtained. Fig.7.24 suggests that the best s/b can be obtained by choosing a higher level energy discrimination (HLD) at about 400 keV; In fact, choosing 400 keV instead of 600 keV would be a further improvement, as it would exclude the Boron peak, which as we have seen is an important contributing of background. Gold also has no significant peaks beyond this threshold.

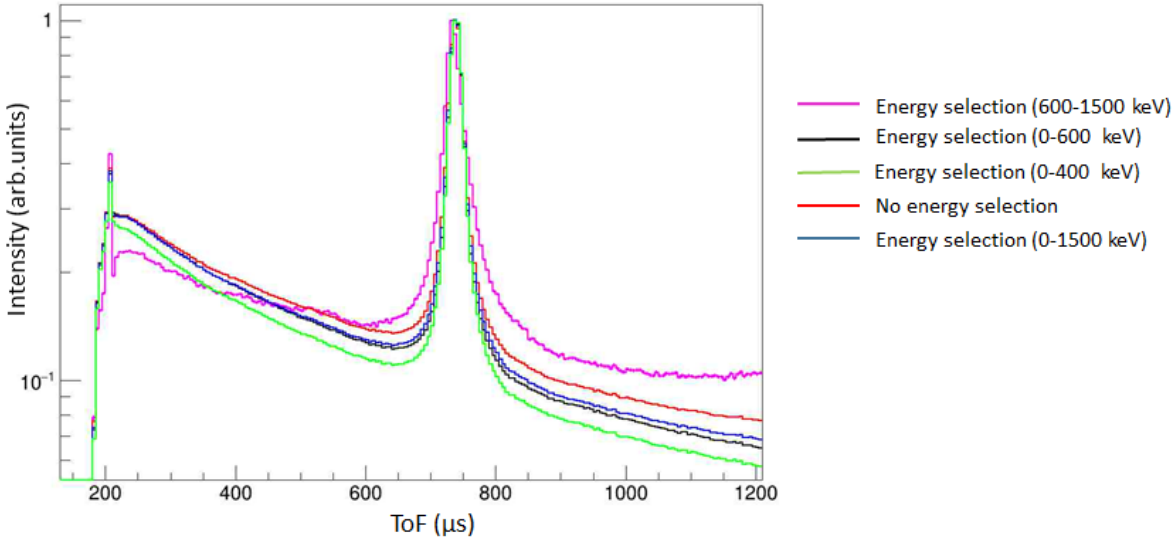

FIGURE 7.24: Neutron time-of-flight spectra for ^{197}Au obtained by projecting the reduced biparametric data on the time axis for five selected energy intervals. The spectra have been normalised so that the intensity of the lowest neutron energy resonance is equal to 1.

This measurement also open the possibility to use a gold foil as a neutron converter coupled with a detector sensitive to photons near the X-rays energy range and less to high-energy photons, such as Gas Electron Multiplier (GEM), RPC or Si-detectors.

7.4 Experiment ongoing carried out on May 15th - May 20th 2017

We now describe the validation experiment based on the proposal made in this thesis to optimize gamma-ray detection emitted by gold analyzer. A DINS experiment was performed on a standard 0.25 mm thick polyethylene sample. Time of flight spectrum from PE sample looks like in fig.7.25. For this detector positioned at a scattering angle of θ=48.6° and L_1=0.539 m from the sample, the peak centred on t=266 μs represents the hydrogen peak while at t=371 μs there is the carbon peak.

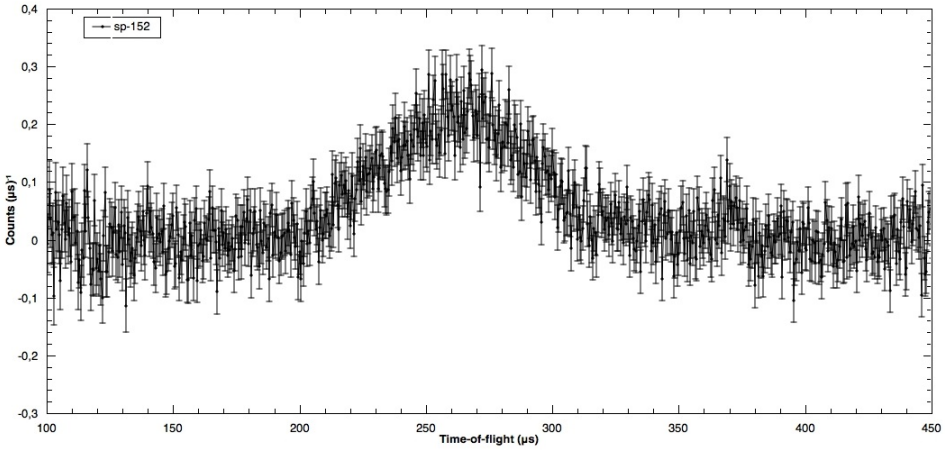

FIGURE 7.25: DINS signal from C_2H_4 sample acquired with the original threshold.

Each Compton peak is centred at ToF position corresponding to:

$$\frac{v_1}{v_0} = \frac{cos\theta + \sqrt{\left(\frac{M}{m}\right)^2 - sin^2\theta}}{\frac{M}{m} + 1} \tag{7.6}$$

Where M is the mass of the stuck atom and m is the neutron mass. The hydrogen peak is not visible with detectors in backscattering because $\left(\frac{M}{m}\right) \sim 1$. ToF peaks are used to calculate the initial neutrons velocity v_0 and then to obtain the incident neutrons energy E_1. The difference $E_1 - E_0$ provides the energy loss $\hbar\omega_r$ in the scattering event. For large values of the stuck mass $\hbar\omega_r$ approach to zero confirming the recoil limit when M$\rightarrow$ inf. The value of $\hbar\omega_{peak}$ depend

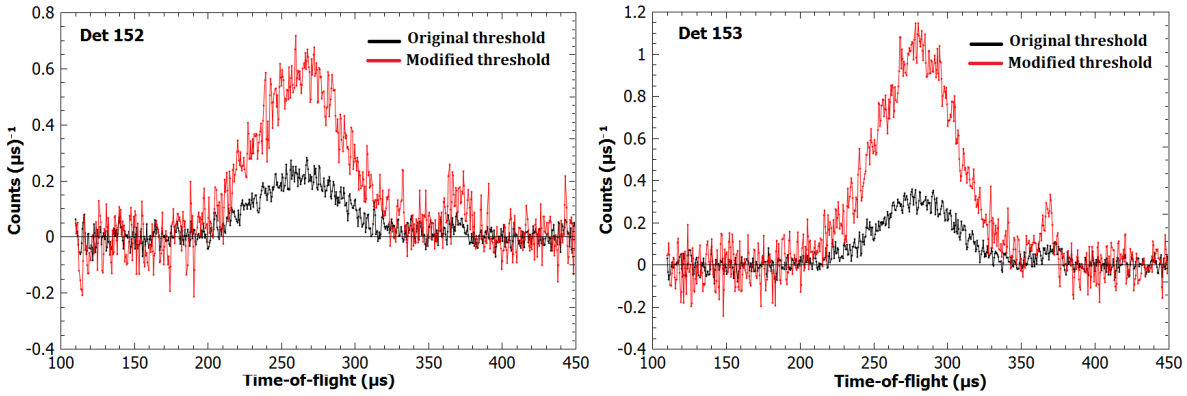

FIGURE 7.26: Figure shows the comparison between DINS spectrum from C_2H_4 sample acquired with the original threshold and the modified threshold.

on q_{peak} that depend itself on the scattering angle:

$$\hbar q = m\sqrt{v_0^2 + v_1^2 - 2v_0 v_1 cos\theta} \tag{7.7}$$

High angle means high q value. The DINS theory impose that

$$\hbar\omega_r = \frac{\hbar^2 q^2}{2M} \tag{7.8}$$

For these reasons, the hydrogen peak appears first in time of flight, the neutron loses less energy in scattering with a lighter atom. The hydrogen peak is bigger then carbon peak because it has a larger scattering cross section. Spectrum in fig.7.25 was acquired without changing the threshold and so the LLD is imposed on 600 keV. Initially we changed the thresholds to 4 detectors, setting them to 0,120,240,360,480 keV respectively. After a quick data analysis, the threshold of about 100 keV was chosen.

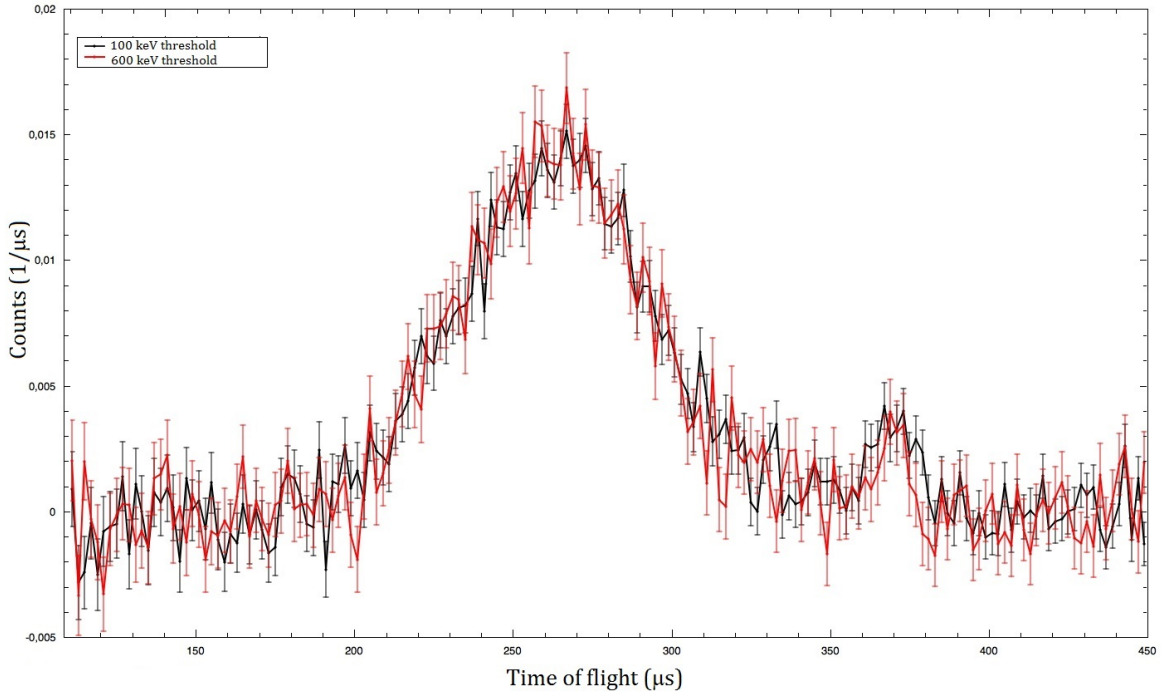

FIGURE 7.27: Black line shows the polyethylene spectrum acquired with a 100 keV LLD. Red line shows the polyethylene spectrum acquired with the original threshold a 600 keV. The spectra were normalized to their area between 100 keV and 450 keV.

Figure7.26 shows the comparison between DINS spectrum from C_2H_4 sample acquired with the original threshold and the modified threshold. We see that changing the threshold increases the count rate on the measurement with the same sample and integer current.

Fig.7.27 shows the comparison between the spectrum acquired with the new threshold and the spectrum acquired with the original 600 keV threshold. This spectra were normalized to their area between 100 keV and 450 keV. In this way even the error bars are divided for the area and are more easily comparable. Relative errors are 20 % inferior in the black spectrum, i.e. with 100 keV threshold.

Within the framework of the IA (Impulse approximation) described in Chapter 4, $\hbar\omega$ and q are explicitly coupled through the West scaling variable y, defined as:

$$y = \frac{M}{\hbar^2 q}(\hbar\omega - \hbar\omega_r) \tag{7.9}$$

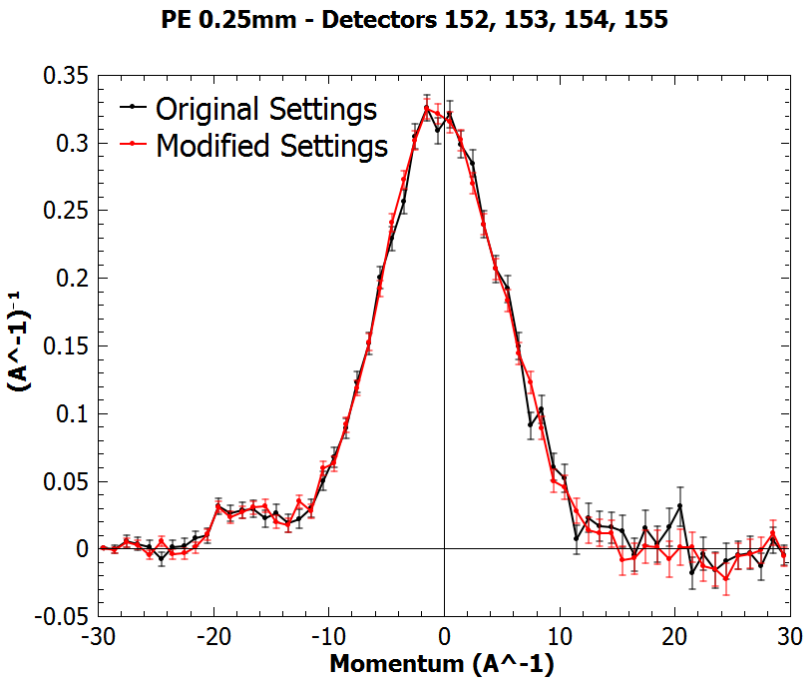

FIGURE 7.28: $J(y, \hat{q})$ for hydrogen peak in PE sample.

So the dynamic structure factor can be reduced to the form

$$S_{IA}(\mathbf{q}, \omega) = \frac{M}{\hbar q} J(y, \hat{q}) \tag{7.10}$$

where

$$J_M(y, \hat{q}) = \hbar \int n(\mathbf{p'}) \delta(\hbar y - \mathbf{p'} \cdot \hat{q}) d\mathbf{p'} \tag{7.11}$$

is the neutron compton profile (NCP), formally defined as the Radon transform of the momentum distribution. The quantity $\hat{q}$ is a unit vector, as J(y,$\hat{q}$) no longer depends on the magnitude of **q**. The function J(y,$\hat{q}$)dy is the probability for an atom to have a momentum parallel to $\hat{q}$ of magnitude between $\hbar$y and $\hbar$(y + dy).

What we see from fig.7.28 is that the shape of the peak doesn't change. Indeed, with the new threshold (red line) we have a better line reconstruction, important to extrapolate data from its. The spectrum is less affected by fluctuations due to error.

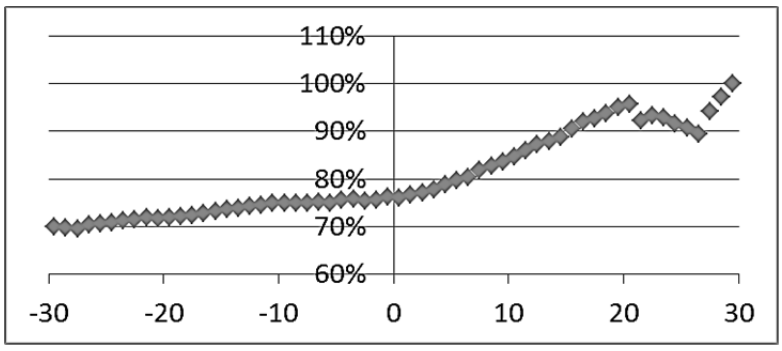

FIGURE 7.29: Plot for the ratio of error bars between the spectra with original and modified spectrum as a function of y.

By making the ratio between the relative errors in the two spectra, the fig.7.29 shows the trend at the variation of y. With the new threshold the error is reduced by an average of 20%.

Chapter 8

Conclusion and Future perspectives

The results obtained in this thesis provide an information to improve the ratio signal to background by measurement gamma emitted by gold foil. Data were acquired with an ad hoc developed biparametric data acquisition, which allowed the simultaneous measurement of the neutron time of flight and γ pulse-height spectra. Analysis of the γ spectra associated with resonant and non-resonant neutron absorption have shown that the observed signal is made up of three main components: (i) X-ray emission, (ii) radiative capture γ emission and (iii) Compton continuum in the low-energy part of the spectrum. The component (i) is the most intense one and is present for both resonant and non-resonant neutron absorption, thus preventing its use for improving the signal to background ratio of the measurement via energy discrimination. The component (ii) is a clear signature of the resonant neutron absorption, but it represents a significant fraction of the overall observed signal only below 400 keV. The component (iii), induced by radiative prompt γ not fully absorbed in the detector, can contain, as in the case of ^{197}Au, a significant fraction of the overall resonance and off-resonance signal. The measured energies and relative intensities of the γ lines of ^{197}Au energy spectra for resonance neutron absorption are in good agreement with the database available. From the data analysis emerges that the dominant contribution given by gold is in the energy region 0 keV -400 keV . This energy range is discarded by VESUVIO's YAP detectors in the actually set-up. In particular in the X-ray energy range between 60 keV-80 keV. This suggest to use a ULD (Upper level discrimination)or window discrimination instead a LLD (low level discrimination), in order to select only the peaks emitted by analyser foil and eliminate other contributions due to the background. The validation experiment suggests that an improvement of s/b can be obtained by setting a new threshold on YAP detectors. The method is effective for ^{197}Au resonances due to a higher difference between the resonance and off-resonance energy spectra in the energy region above 50 keV: this increasing difference in the gamma energy spectra at this energy seems to suggest that a detector set to observe a broader energy range might have better performance. In the future tests with other types of detectors could be performed, like RPC/GEM detectors or Si-detectors which are sensitive to X-rays and less to high-energy photons. A first data analysis of the validation experiment shows, however, that this is the right way to go, opening the doors to a new quality of experimentation.

.

Appendix A

Main ROOT algotithm

A.1 Variable definition

```
// Global Variables

// ***************** Path Germanium and T0 File *******************************
TString dir_inp=("/home/dalila/Desktop/dalila_oro/");
TString filename_t0 = ("beam_12_003_ls_1.dat");
TString filename_germ = ("beam_12_003_ls_0.dat");

TString dir_out=("/home/dalila/Desktop/dalila_oro/");
TString filename_out = ("ines_dalila.root");

// Set TH2D E_vs_ToF

int n_ToF = 4000; // 1bin=5us
int min_ToF = 0;
int max_ToF = 20000;
int n_E = 20000;
int min_E = 0;
int max_E = 20000;

//Set TH2D new range
   int n_Tnew=1000; // 1bin=1us
   int Tmin1 =200;
   int Tmax1 =1200;

   int n_Enew=1000;
   int Emin = 0;
   int Emax = 1000;

//Variables for calibration E=a0+a1*CH
double a1 = 0.5592;
double a0 = -0.3748;
```

A.2 Main ROOT algorithm

```
// Root libraries
#include <TStopwatch.h>
#include <TROOT.h>
#include <Riostream.h>
#include <TH1.h>
#include <TString.h>
#include <TFile.h>
#include <TGraph.h>
#include <TH2D.h>
#include <TVector.h>

// C++ libraries
#include "sstream"
#include "iostream"
#include "cstring"

// include config file
#include "GERMANIO_GlobalVariables_dalila.h"

void GERMANIO_dalila(){
```

```
TStopwatch clock;
clock.Reset();
clock.ResetRealTime();
clock.ResetCpuTime();
clock.Start();

cout << "Read global configuration file : GERMANIO_GlobalVariables_dalila.h" << endl;
cout << "" << endl;

// Open to file input
ifstream fileinp_t0;
fileinp_t0.open(dir_inp + filename_t0,ios::in);
cout << "Open T0 input file: " << dir_inp + filename_t0 << endl;

// Open germanium file input
ifstream fileinp_germ;
fileinp_germ.open(dir_inp + filename_germ,ios::in);
cout << "Open Germanium input file: " << dir_inp + filename_t0 << endl;

TFile *fout = new TFile(dir_out + filename_out, "RECREATE");
cout << "Write results in: " << dir_out + filename_out << endl;
cout << "" << endl;

// Create Histograms
TH1I *h_t0_timestamp = new TH1I("h_t0_timestamp", "t0_timestamp", n_ToF, min_ToF,
    max_ToF);// ogni 100 burst
TH1I *h_germ_energy_ch = new TH1I("h_germ_energy_ch", "germ_energy_ch", n_E, min_E,
    max_E);

//Set TH2D new range

TH2D *h2_E_vs_ToF = new TH2D("h2_E_vs_ToF", "E_vs_ToF", n_ToF, min_ToF, max_ToF, n_E,
    min_E, max_E);
// TH2D *h2_E_vs_ToF = new TH2D("h2_E_vs_ToF", "E_vs_ToF", n_Tnew, Tmin1, Tmax1, n_Enew,
    Emin, Emax);


//TH1I *h_mult = new TH1I("h_mult","Multiplicity", 150, 0, 150);


//Define variables for input file
unsigned long int ts_ToF1, ts_ToF2, ts_germ = 0;
unsigned long int nothing1, nothing2 = 0;
double ToF, PH = 0.;
int n_point = 0;
int var_control = 0;
//int mult = 0;

fileinp_t0 >> ts_ToF1 >> nothing1;
fileinp_t0 >> ts_ToF2 >> nothing2;

cout << "********* Start iterations ********** " << endl;
cout << "" << endl;

while(fileinp_t0.good() && fileinp_germ.good()) {

    if(n_point%100000 == 0){
     cout << "Iteration number: " << n_point << endl;
    }

           if( var_control == 0){
             while(ts_germ<ts_ToF1){
               fileinp_germ >> ts_germ >> PH;
             }
           var_control = 1;
           }

    while(ts_germ < ts_ToF2){
       ToF = double(ts_germ - ts_ToF1)/100;

       h2_E_vs_ToF->Fill(ToF, PH);
       h_germ_energy_ch->Fill(PH);
        h_t0_timestamp->Fill(ToF);
       fileinp_germ >> ts_germ >> PH;
       //mult+=1;
```

```
       }

       //Fill multiplicity
       //h_mult->Fill(mult);

       // Reset multiplicity
      // mult = 0;

        ts_ToF1 = ts_ToF2;
        fileinp_t0 >> ts_ToF2 >> nothing2;
        fileinp_germ >> ts_germ >> PH;

        n_point+=1;
      }


   // Write output file
   fout->Write();
   fout->Close();

   // Calculate and print final statistics
   clock.Stop();
   cout << "" << endl;
   cout << "********* Print Statistics *********" << endl;
   cout << "" << endl;
   printf("RealTime=%f seconds, CpuTime=%f seconds\n",clock.RealTime(),clock.CpuTime());
   cout << "" << endl;

   cout << "****************************************************************" << endl;
   cout << "" << endl;


}
```

A.3 PGAA and NRCA

```
// Root libraries
#include <TStopwatch.h>
#include <TROOT.h>
#include <Riostream.h>
#include <TH1.h>
#include <TString.h>
#include <TFile.h>
#include <TGraph.h>
#include <TH2D.h>
#include <TVector.h>

// C++ libraries
#include "sstream"
#include "iostream"
#include "cstring"

// include config file
#include "GERMANIO_GlobalVariables_original.h"


TH1D* GERMANIO_plot_spectra_gamma_tof(){

   //Open file with TH2D
   TFile *finp = new TFile(dir_out + filename_out);
   TH2D *h2_E_vs_ToF = (TH2D*)finp->Get("h2_E_vs_ToF");



h2_E_vs_ToF->ProjectionY("py_1_16000", 1, 16000 , ""); //gamma
TH1D *h_py_1_16000 = (TH1D*)gROOT->FindObject("py_1_16000");
h_py_1_16000->GetXaxis()->Set(16000, 0.5592, 8946.83); //calibrazione


h2_E_vs_ToF->ProjectionX("px_1_20000", 1, 20000 , ""); // TOF
TH1D *h_px_1_20000 = (TH1D*)gROOT->FindObject("px_1_20000");


h_py_1_16000->SetLineColor(1);
```

```
h_px_1_20000->SetLineColor(6);

TAxis* the_x = h_py_1_16000->GetXaxis();
Int_t last = the_x->GetLast();
Double_t this_x, this_y;


for(int i=1; i <= last; i++) {
   this_x = h_py_1_16000->GetBinCenter(i);
   this_y = h_py_1_16000->GetAt(i);

    printf("%f %f\n", this_x, this_y);
}

return h_py_1_16000;

for(int i=1; i <= last; i++) {
   this_x = h_px_1_20000->GetBinCenter(i);
   this_y = h_px_1_20000->GetAt(i);

    printf("%f %f\n", this_x, this_y);
}
return h_px_1_20000;

h_py_1_16000->Print();
h_py_1_16000->Draw();
h_px_1_20000->Draw("same");

//TOF->Write();
//TOF->Close();
return 0;

}
```

A.4 Energy vs ToF map

```
// Root libraries
#include <TStopwatch.h>
#include <TROOT.h>
#include <Riostream.h>
#include <TH1.h>
#include <TString.h>
#include <TFile.h>
#include <TGraph.h>
#include <TH2D.h>
#include <TVector.h>
#include <TStyle.h>
#include <TColor.h>

// C++ libraries
#include "sstream"
#include "iostream"
#include "cstring"

// include config file
#include "GERMANIO_GlobalVariables_dalila.h"


void GERMANIO_boxes(){
   //Open file with TH2D
   //TFile *finp = new TFile(dir_out + filename_out);
   TFile *finp = new TFile("ines_dalila.root");
   TH2D *h2_E_vs_ToF = (TH2D*)finp->Get("h2_E_vs_ToF");

  //  h2_E_vs_ToF->GetYaxis()->Set(1000, 0.5592, 558.82);
    h2_E_vs_ToF->GetYaxis()->Set(20000, -0.3748, 11183.6252);

   TH2 *h2_bins = h2_E_vs_ToF; //->Rebin2D(1,1); //1bin=5us
   gStyle->SetPalette(55);
   h2_bins->Draw("COLZ");
   h2_E_vs_ToF->Draw("COLZ");

////////////////////////////////////
```

```
TH2D *h_prova = new TH2D("prova", "prova", 11, 700, 755, 31, 55.63468, 86.260602);

Double_t this_x, this_y, this_z;
Int_t bin=0;
Int_t bin_prova=0;
TAxis* the_x = h2_bins->GetXaxis();
TAxis* the_y = h2_bins->GetYaxis();
Int_t lastx = the_x->GetLast();
Int_t lasty = the_y->GetLast();


for(int i=700; i <= 750;) {
 for(int j=55; j<=85; j++){
    bin=0;
    bin_prova=0;
    this_x=h2_bins->GetXaxis()->GetBinCenter(h2_bins->GetXaxis()->FindBin(i));
    this_y=h2_bins->GetYaxis()->GetBinCenter(h2_bins->GetYaxis()->FindBin(j));
    bin = h2_bins->GetBin(i,j);
    this_z=h2_bins->GetBinContent(bin);
    printf("%f %f %f\n", this_x, this_y, this_z);
    bin_prova=h_prova->GetBin(this_x, this_y);
    h_prova->SetBinContent(bin_prova,this_z);
    h_prova->Fill(this_x, this_y, this_z);
    }
    i=i+5;
}

h2_bins->Print();
h_prova->Draw("COLZ");

//new style graph
 const Int_t Number = 3;
Double_t Red[Number] = { 1.00, 0.00, 0.00};
Double_t Green[Number] = { 0.00, 1.00, 0.00};
Double_t Blue[Number] = { 1.00, 0.00, 1.00};
Double_t Length[Number] = { 0.00, 0.50, 1.00 };
Int_t nb=50;
TColor::CreateGradientColorTable(Number,Length,Red,Green,Blue,nb);
h2_E_vs_ToF->SetContour(nb);
h2_E_vs_ToF->SetLineWidth(1);
h2_E_vs_ToF->SetLineColor(kBlack);

  h2_bins->Draw("surflz");

// Make cuts that I need
 h2_E_vs_ToF->ProjectionY("py_on", 144, 152 , ""); //bin to bin
 TH1D *h_py_on = (TH1D*)gROOT->FindObject("py_on");

h2_E_vs_ToF->ProjectionY("py_off", 180, 192 , "");
TH1D *h_py_off = (TH1D*)gROOT->FindObject("py_off");
 h_py_on->SetLineColor(1);
 h_py_on->SetLineWidth(1);
 h_py_on->Draw();
 h_py_off->SetLineColor(2);
 h_py_off->SetLineWidth(1);
 h_py_off->Draw("same");

// PGAA

  h2_E_vs_ToF->ProjectionY("py_1_16000", 1, 16000 , ""); //gamma
  TH1D *h_py_1_16000 = (TH1D*)gROOT->FindObject("py_1_16000");


// NRCA

h2_E_vs_ToF->ProjectionX("px_1_20000", 1, 20000 , ""); //ToF
TH1D *h_px_1_20000 = (TH1D*)gROOT->FindObject("px_1_20000");

h_px_1_20000 ->SetLineColor(2);
h_py_1_16000->SetLineColor(3);
h_py_1_16000->Draw();
h_px_1_20000 ->Draw("same");

}
```

A.5 Projection and analysis

```
// Root libraries
#include <TStopwatch.h>
#include <TROOT.h>
#include <Riostream.h>
#include <TH1.h>
#include <TString.h>
#include <TFile.h>
#include <TGraph.h>
#include <TH2D.h>
#include <TVector.h>
#include <TStyle.h>
#include <TColor.h>
#include <TF1.h>

// C++ libraries
#include "sstream"
#include "iostream"
#include "cstring"

// include config file
#include "GERMANIO_GlobalVariables_original.h"


void GERMANIO_boro(){
   //Open file with TH2D
   //TFile *finp = new TFile(dir_out + filename_out);
   TFile *finp = new TFile("ines_dalila.root");
   TH2D *h2_E_vs_ToF = (TH2D*)finp->Get("h2_E_vs_ToF");

  //  h2_E_vs_ToF->GetYaxis()->Set(1000, 0.5592, 558.82);
    h2_E_vs_ToF->GetYaxis()->Set(20000, -0.3748, 11183.6252);

   TH2 *h2_bins = h2_E_vs_ToF;
   gStyle->SetPalette(55);
   h2_E_vs_ToF->Draw("COLZ");

// ToF cuts

h2_E_vs_ToF->ProjectionY("py_range_1", 143, 147 , "");
TH1D *h_py_range_1 = (TH1D*)gROOT->FindObject("py_range_1");
h2_E_vs_ToF->ProjectionY("py_range_2", 138, 142 , "");
TH1D *h_py_range_2 = (TH1D*)gROOT->FindObject("py_range_2");


TH1D *h_py_range_4 = (TH1D*)gROOT->FindObject("py_range_4");

h_py_range_1->SetLineColor(1);
h_py_range_2->SetLineColor(2);
h_py_range_1->Draw();
h_py_range_2->Draw("same");

h_py_range_1->GetXaxis()->SetRange(700,1000);


//Set gaussian parameter

//TF1 *g3 = new TF1("g3","[0]+[1]*exp(-0.5*((x-[2])/([3]))^2)", 460, 500);
//g3->SetParName(0,"baseline");
//g3->SetParName(1,"constant");
//g3->SetParName(2,"mean");
//g3->SetParName(3,"sigma");
//g3->SetParameters(100, 300, 478, 10);
//h_py_range_1->Fit(g3,"R");
//g3->Draw("same");

//Fit range_1

TF1 *back = new TF1("back","[0]*exp(-x/[1])+[2]", 200, 1000);
back->SetParName(0,"int");
back->SetParName(1,"slope");
back->SetParName(2,"cost");
back->SetParameters(1750, 160, 50 );
```

```
h_py_range_1->Fit(back,"R");

TF1 *g1 = new TF1("g1","[0]+[1]*exp(-0.5*((x-[2])/([3]))^2)+[4]*exp(-x/[5])", 200, 1000);
g1->SetParName(0,"baseline");
g1->SetParName(1,"constant");
g1->SetParName(2,"mean");
g1->SetParName(3,"sigma");
g1->SetParName(4,"int");
g1->SetParName(5,"slope");
g1->SetParameters(100, 300, 478, 10, 160, 50);
h_py_range_1->Fit(g1,"R");

TF1 *somma = new TF1("somma", "g1-back", 200, 1000);
somma->Draw("same");

g1->Draw("same");

//FiT range_2

TF1 *back2 = new TF1("back2","[0]*exp(-x/[1])+[2]", 200, 1000);
back2->SetParName(0,"int");
back2->SetParName(1,"slope");
back2->SetParName(2,"cost");
back2->SetParameters(2000, 200, 160 );
h_py_range_2->Fit(back2,"R");


TF1 *g2 = new TF1("g2","[0]+[1]*exp(-0.5*((x-[2])/([3]))^2)+[4]*exp(-x/[5])", 200, 1000);
g2->SetParName(0,"baseline2");
g2->SetParName(1,"constant2");
g2->SetParName(2,"mean2");
g2->SetParName(3,"sigma2");
g2->SetParName(4,"int2");
g2->SetParName(5,"slope2");
g2->SetParameters(247, 8, 478, 3, 2000, 200);
h_py_range_2->Fit(g2,"R");

TF1 *somma2 = new TF1("somma2", "g2-back2", 200, 1000);
somma2->SetLineColor(11);
somma2->Draw("same");
g2->SetLineColor(6);
g2->Draw("same");



// Energy cuts

h2_E_vs_ToF->ProjectionX("px_range_2", 1073, 2683 , "");
TH1D *h_px_range_2 = (TH1D*)gROOT->FindObject("px_range_2");
h_pxh_px_range_2->SetLineColor(6);
h_px_range_2->SetLineWidth(3)

h_px_range_2->Draw("same");


}
```

Bibliography

[1] L. Molnar, Gabor (2004). Handbook of prompt Gamma Activation Analysis with neutron beam.

[2] E. M. Schooneveld, A. Pietropaolo, C. Andreani, E. Perelli Cippo,N. J. Rhodes, R. Senesi, M. Tardocchi and G. Gorini (2016) Radiative neutron capture as a counting technique at pulsed spallation neutron sources: a review of current progress.

[3] A. Pietropaolo, M. Tardocchi, E. M. Schooneveld R. Senesi (2006). Characterization of the background in epithermal neutron scattering measurements at pulsed neutron sources. Nuclear Instrument and Methods in Physics Research.

[4] M. Tardocchi, G. Gorini, A. Pietropaolo, C. Andreani and R.Senesi. YAP scintillators for resonant detection of epithermal neutrons at pulsed neutron sources. Rev. Sci. Instru. Vol. 75, No.11 2004.

[5] G. Festa, L. Arcidiacono, A. Pappalardo, T. Minniti, C. Cazzaniga, A. Scherillo, C. Andreani, and R. Senesi. Isotope identification capabilities using time resolved prompt gamma emission from epithermal neutrons, Journal of Instrumentation, volume 11, 29 March 2016.

[6] ENDF: Evaluated Nuclear Data File www.nds-iaea.org

[7] K. Skold and D. Price. Methods of Experimental Physics, vol 23-part A, Neutron Scattering, Academic Press 1986.

[8] C. Windsor. Pulsed neutron scattering, Taylor and Francis (1981).

[9] P. Bode. Nuclear Analysis Technique.

[10] P. Schillebeeckx, B. Becker, Y. Danon et al. Determination of Resonance Parameters and their Covariances from Neutron Induced Reaction Cross Section Data, science direct, 2012.

[11] G.S. Bauer. Physics and technology of Spallation Neutron Sources, Lecture notes for the Frederic Jolliot Summer School 1998.

[12] H. Postma and P. Schillebeeckx. Neutron Resonance Capture and Transmission Analysis, in R.A. Meyers ed., Encyclopedia of Analytical Chemistry, Wiley, New York 2009.

[13] A. Pietropaolo, G. Gorini, G.Festa, E. Reali, F. Grazzi and E. Schoonevelt. A Neutron Resonance Capture Analysis Ex- perimental Station at the ISIS Spallation Source, Spectroscopic technique vol 64, number 9, 2010.

[14] L. Bartoli, M. Celli, F. Grazzi, S. Imberti, S. Siano, M. Zoppi. Neutron Diffraction in archeometry: the italian neutron experi- mental station INES, storia della metallurgia, september 2008.

[15] G. Gorini et al. Analysis by neutron resonant capture imaging and other emerging neutron techniques, final activity report may 2010.

[16] Yosuke Toh, Mitsuru Ebihara, Atsushi Kimura, Shoji Nakamura, Hideo Harada, Kaoru Y. Hara, Mitsuo Koizumi, Fumito Kitatani, and Kazuyoshi Furutaka. Synergistic Effect of Combining Two Nondestructive Analytical Methods for Multielemental Analysis, Analytical chemistry 2014.

[17] W.R. Leo. Techniques for Nuclear and Particle Physics Experiments.

[18] H. Postma, P.Schillebeeckx. Non-destructive analysis of objects using neutron resonance capture, 2005.

[19] A. Miceli et al. Measurements of gamma-ray background spectra at spallation neutron source beamlines, J. Anal. Atom. Spectrom. 29 1897.

[20] Glenn F. Knoll. Radiation Detection and Measurement, Wiley 2000.

[21] A. Foderaro. The elements of neutron interaction theory, the MIT press 1971.

[22] J. Mayers. Calculation of background effects on the VESUVIO eV neutron spectrometer.

[23] D. Flammini, A. Pietropaolo, R. Senesi, C. Andreani, F. McBride et al. Spherical momentum distribution of the protons in hexagonal ice from modeling of inelastic neutron scattering data.

[24] G. Gilmore Practical Gamma-ray Spectrometry.